2021

ELECTRICAL POWER TAKE-OFF SYSTEM DESIGN AND PERFORMANCE ASSESSMENT FOR POINT ABSORBER WAVE ENERGY CONVERTER

Xiang Zhou
Michigan Technological University, xiangzho@mtu.edu

ELECTRICAL POWER TAKE-OFF SYSTEM DESIGN AND PERFORMANCE ASSESSMENT FOR POINT ABSORBER WAVE ENERGY CONVERTER

By

Xiang Zhou

A DISSERTATION

Submitted in partial fulfillment of the requirements for the degree of

DOCTOR OF PHILOSOPHY

In Mechanical Engineering-Engineering Mechanics

MICHIGAN TECHNOLOGICAL UNIVERSITY

2021

This dissertation has been approved in partial fulfillment of the requirements for the Degree of DOCTOR OF PHILOSOPHY in Mechanical Engineering-Engineering Mechanics.

Department of Mechanical Engineering-Engineering Mechanics

Dissertation Co-advisor: *Dr. Wayne W. Weaver*

Dissertation Co-advisor: *Dr. Ossama Abdelkhalik*

Committee Member: *Dr. Gordon G. Parker*

Committee Member: *Dr. Chee-Wooi Ten*

Department Chair: *Dr. William W. Predebon*

Contents

List of Figures

List of Tables

Preface

Chapter 1 presents the introduction of this research, which includes the backgrounds of wave energy and wave energy conversion applications. Chapter 2 presents the main challenge of the wave energy converter (WEC) development, the literature review in the Chapter 2 shows the research and design efforts for improving the buoy control and electrical power take-off (PTO) performance in the wave-to-wire (W2W) energy conversion. Chapter 3 introduces the basic dynamics of the W2W modeling, which includes the buoy linear hydrodynamic modeling, the permanent magnet linear electrical machine (LEM) dynamic modeling, the inverter and direct drive (DC) modeling. Chapter 4 includes several reactive power control schemes, such as Proportional-Derivative (PD) complex conjugate control (CCC), singular-arc (SA) control, model predictive control (MPC) and shape-based (SB) control. The Chapter 4 mainly introduces the PDCCC and SB and provides the related literature for other control schemes. Chapter 5 presents a electrical PTO static modeling strategy for W2W energy extraction evaluation with ground-truth ocean wave data. The energy conversion potentials with various control force limits are provided. Chapter 6 presents the energy storage system (ESS) sizing statistical study based upon the W2W energy extraction evaluation methodology in the Chapter 5. 15-years ground-truth ocean wave data is applied in this chapter and the Bayesian statistic theory is used to improve the ESS design reliability. Chapter 7 presents the assessments of

the energy extraction performance of several selected model-based control schemes (according to the Chapter 4) with considering the actual electrical PTO effects. The PTO copper loss model and nonlinear loss model (actual efficiency maps) are both considered. The possible solutions for improving the energy extraction performance are also provided. In Chapter 8, the machine reinforcement learning (RL), one solution which is discussed in the Chapter 7, is applied to design the control for the W2W energy extraction from a global point of view. The performance comparison between the RL control and the original model-based control is provided. The output mean power and output power quality are included as well with considering simple sea state and ground-truth sea state. Chapter 9 presents the research summury and the future research plan.

The results present in the Chapter 5 are published as reference [1], X. Zhou conceived the idea and performed the simulation, O. Abdelkhalik provided the buoy hydrodynamic and control support, and W. Weaver supervised the PTO modeling and integration. The results present in the Chapter 6 are published as reference [2], X. Zhou concerived the idea and performed the simulation, M. Jafari provided the Bayesian Network algorithm support, O. Abdelkhalik and U.A. Korde helped to plan the simulation, L. Gauchia supervised the research and revised the paper. The results present in the Chapter 7 are published as reference [3, 4], X. Zhou conceived the idea and performed the simulation, S. Zou provided the buoy hydrodynamic and control support, W.W. Weaver supervised the research and revised the paper and

O. Abdelkhalik helped to review the paper and results. The results present in the Chapter 8 are published as reference [5], X. Zhou conceived the idea and performed the simulation, S. Zou provided the buoy hydrodynamic and control support, W.W. Weaver supervised the research and revised the paper and O. Abdelkhalik helped to review the paper and results.

Acknowledgments

I would like to express my deepest gratitude to all those who have supported me, helped me, and inspired me during my doctoral program at Michigan Technological University. Thanks to everyone, this journey towards PhD is truly wonderful!

I thank my family for their never-ending love and trust. Your encouragement shined my way forward even in the darkest night.

I would like to thank my former advisor, Dr. Lucia Gauchia. Thank you for giving me the opportunity to join your research group and pursue a Ph.D. degree. I would like to thank my current advisor, Dr. Wayne Weaver. You gave me the most help, and guided me when I met the biggest challenge in my research. Thanks to all the committee members. Thanks to my co-advisor Dr. Ossama Abdelkhalik, who helped me to start my wave energy converter journey. Thanks to Dr. Gordon Parker who advised me for my research model design. Thanks to Dr. Chee-Wooi Ten who helped me with my electrical power take-off system research.

I thank all my friends and lab-buddies, Dr. Jiajun Song, Dr. jianyang Lyu, Dr Shangyan Zou, and Dr. Mingyang Li. Doing research in the same lab, even in the same building with you would really make my day. You have taught me a lot, not only about the technical study, but also about life. Some of you have left the country,

but I will always remember everything we had in the MEEM building.

I also would like to thank all my friends in MTU, in Houghton, and in Hancock. Having you guys would really make the place be my second hometown.

This list can never end since you are all important people to me and I will always cherish these memories. Thank you all again, for making my journey wonderful and full of joys.

Nomenclature

A	Agent Action Space
a	Agent Action
A_i	Excitation Force Amplitude in Frequency i $[N]$
a_i	Fourier Series Unknown Coefficient
A_r	Radiation Matrix
b_i	Fourier Series Unknown Coefficient
B_r	Radiation Matrix
B_v	Viscous Damping
c_i	Viscous Damping in Frequency i
C_r	Radiation Matrix
D	Observed Variables
δK_d	Derivative Gain Step Change
δK_p	Proportional Gain Step Change
e_{abc}	Electrical Machine Induced Voltage $[V]$
E_{dis}	Discharged Energy $[J]$
e_{dq}	Electrical Machine Induced Voltage in dq $[V]$
E_{net}	Net Charged Energy $[J]$
η	Electrical PTO Efficiency

η_{act}	Active Power Efficiency
η_{all}	Overall Efficiency
η_b	Electrical PTO Efficiency Boundary
η_{em}	Electrical Machine Efficiency Map
η_{inv}	Inverter Efficiency Map
η_{react}	Reactive Power Efficiency
f	Chebyschev's Theorem Fraction
F_c	PTO Optimal Control Force Signal $[N]$
F_e	Wave Excitation Force $[N]$
F_{PTO}	PTO Control Force $[N]$
$F_{PTO,ref}$	Reference PTO Control Force Signal $[N]$
F_r	Radiation Force $[N]$
F_s	Hydro-static Force $[N]$
γ	Future Reward Discount
H	Unobserved Variables
H_s	Wave Significant Wave Height $[m]$
i_{abc}	Three-phase Current $[A]$
i_b	Battery Terminal Current $[A]$
i_{dc}	DC Current $[A]$
i_{dq}	Current in dq $[A]$
i_{max}	Maximum Current $[A]$

i_{qc}	Current Flow between Super-capacitor and Generator $[A]$
i_{qM}	Motor Mode Current Input $[A]$
$i_{q,ref}$	Reference Signal $[A]$
K	Linear Hydra-static Coefficient
k	Number of Considered Standard Deviation
k_i	One Frequency Linear Hydra-static Coefficient
K_d	Total Derivative Control Gain
K_{di}	Derivative Control Gain in in Frequency i
$K_{i,dq}$	Integral Control Gain in dq Frame
K_p	Total Proportional Control Gain
$K_{p,dq}$	Proportional Control Gain in dq Frame
K_{pi}	Proportional Control Gain in in Frequency i
λ	Depth of Modulation
L_s	Electrical Machine Inductance $[H]$
L_{dq}	Electrical Machine Inductance in dq $[H]$
m	Buoy Inertia $[kg]$
$m_{add,\infty}$	Buoy Added Mass at Infinite Frequency $[kg]$
$MCFL_{H_{si}T_i}$	Maximum Control Force for One Spectrum $[N]$
$MCFL_{bi}$	Bi-spectrum Control Force Limit $[N]$
m_i	Buoy Inertia in Frequency i $[kg]$
MPL_{biG}	Bi-spectrum Generator Mode Maximum Power $[W]$

MPL_{biM}	Bi-spectrum Motor Mode Maximum Power $[W]$
m_r	Buoy Rigid Body Mass $[kg]$
M_t	Buoy Total Mass $[kg]$
n_p	Electrical Pole Pair Number
ω_{eG}	Generator Mode Speed Input $[rad/s]$
ω_e	Electrical Speed $[rad/s]$
ω_i	One Wave Frequency $[rad/s]$
ω_n	Wave Frequency $[rad/s]$
ϕ	AC Voltage Phase in dq
ϕ_i	One Wave Phase $[rad]$
ϕ_n	Wave Phase $[rad]$
ψ_f	Field Magnetic Flux $[Wb]$
P_{bc}	Power Flow between Super-capacitor and Battery $[W]$
P_e	Output Electrical Power $[W]$
P_{elec}	DC Output Electrical Power $[W]$
P_{e_m}	Extracted Mechanical Power $[W]$
P_{e_l}	Extracting Power Loss $[W]$
P_{loss}	Electrical Copper Loss $[W]$
P_{mean}	Mean Power $[W]$
P_{mech}	Buoy Transmitted Mechanical Power $[W]$
P_{op}	Optimal Output Electrical Power $[W]$

P_{pl}	Providing Power Loss $[W]$
P_{pm}	Provided Mechanical Power $[W]$
P_{qc}	Power Flow between Generator and Super-capacitor Pack $[W]$
r	Agent Collected Reward
r_{COV}	COV Ratio
r_{eq}	Electrical Machine Equivalent Radius $[m]$
r_{PTA}	PTA Ratio
R	Buoy Total Viscous Damping
R_{eq}	Equivalent Resistance $[\Omega]$
R_{line}	DC Circuit Resistance $[\Omega]$
R_s	Electrical Machine Internal Resistance $[\Omega]$
s	Environment State
T	Wave Significant Period $[s]$
T_c	Jump Time Period $[s]$
T_e	Electrical Machine Input Torque $[Nm]$
T_{energy}	Wave Energy Period $[s]$
T_{eG}	Generator Mode Torque Input $[Nm]$
T_{end}	Time Frame End $[s]$
T_H	Prediction Horizon $[s]$
T_p	Wave Peak Period $[s]$
t_{RL}	Agent Control Step Time

θ_i	Deep Neural Network Weight
$\theta_{e,abc}$	Electrical Machine Rotor Position
u	Control Force $[N]$
u_i	Control Force in Frequency i $[N]$
u_{max}	Maximum Control Force $[N]$
v_{abc}	Electrical Machine Terminal Voltage $[V]$
V_{dc}	Inverter DC Voltage$[V]$
v_{dq}	Electrical Machine Terminal Voltage in dq $[V]$
$v_{dq,ref}$	Reference Signal $[V]$
V_{op}	Buoy Optimal Velocity $[m/s]$
v_{qM}	Motor Mode Voltage Input $[V]$
V_s	DC Constant Voltage Source $[V]$
W	Energy Production $[J]$
y	Target Function
z	Buoy Displacement $[m]$
z_i	Buoy Displacement in Frequency i $[m/s]$
z_{max}	Maximum Buoy Displacement $[m]$
z_{min}	Minimum Buoy Displacement $[m]$
$\dot{z}$	Buoy Velocity $[m/s]$
$\dot{z}_i$	Buoy Velocity in Frequency i $[m/s]$
$\ddot{z}$	Buoy Acceleration $[m/s^2]$

$\ddot{z}_i$ Buoy Acceleration in Frequency i $[m/s^2]$

List of Abbreviations

AC	Alternating Current
CC	Complex Conjugate
CCC	Complex Conjugate Control
COV	Coefficient of Variation
DC	Direct Current
DNN	Deep Neural Network
DQN	Deep Q-network
DRL	Deep Reinforcement Learning
ESS	Energy Storage System
LEM	Linear Electrical Machine
MCFL	Maximum Control Force Limitation
MPC	Model Predictive Control
MPL	Maximum Power Limitation
OCV	Open Circuit Voltage
PD	Proportional-Derivative
PDF	Probability Density Function
PI	Proportional-Integral
PMLEM	Permanent Magnet Linear Electrical Machine

PTA	Peak to Average Ratio
PTO	Power Take-off System
RL	Reinforcement Learning
SA	Singular Arc
SB	Shape-based
SC	Super-capacitor
SD	Standard Deviation
WEC	Wave Energy Converter
W2W	Wave to Wire

Abstract

Wave energy has great potential but has a high levelized energy cost comparing to other renewable energy sources (e.g., solar and wind). Improving the buoy control performance in the wave-to-wire energy conversion would be a straightforward way to increase the wave energy conversion efficiency and decrease the wave energy levelized cost. To improve the buoy control schemes design, the assessment of the state of the art controls and the study of the power take-off (PTO) power loss model are demanded. This dissertation starts with the basic dynamics of the wave energy converter (WEC) buoy and electrical PTO, introduces essential mechanics of the WEC wave-to-wire model composing. Furthermore, the details of the electrical machine control methodologies and the state of the art buoy control schemes are included as well to generate the WEC wave-to-wire control frame. According to the wave-to-wire dynamic model, one fast evaluation methodology for energy extraction potential assessment is introduced. The sea-state-output-power matrices are generated while considering various electrical PTO effects and constraints to obtain electrical output power directly instead of relying on dynamic models propagation. Based upon the fast evaluation methodology, 16-years ground truth ocean wave data is analyzed for solving energy storage system (ESS) sizing problems for off-shore applications. To improve the ESS design reliability, the statistical study is applied as well. To further study the electrical PTO power loss model, the PTO dynamic model is implemented

to the WEC buoy dynamic model. Several state of the art WEC buoy control schemes are applied on the device and the performance is assessed. While considering the PTO copper losses, operation constraints and the PTO nonlinear power loss model, the results show that the buoy control schemes will be affected significantly by the actual PTO dynamics. By studying the PTO operation efficiency, the possible solutions for improving the WEC energy extraction performance are provided. Designing the control for the wave-to-wire from a global point of view is demanded. So in the last chapter, the machine reinforcement learning (RL) control for the WEC wave-to-wire modeling is proposed, and the results are compared to other model-based controls, which turns out that the RL control can achieve much higher output power with better power qualities and it is robust for various wave conditions. According to the research results, future study plan is discussed as well in the last.

Chapter 1

Introduction

Traditional fossil fuel energy storage limit on the planet Earth has been discussed in the early global energy study [6]. Sustainable renewable energy is required for the world carbon neutrality. Since then, more and more renewable energy extraction applications have been studied and developed to reduce the carbon release in the future, such as solar farms, wind farms, etc. The wind and solar energy conversion technologies have been well developed and the plants are widely located in many countries. Wave energy, as a different kind of renewable energy, has great potential. Oceans take more than 70% of the planet surface area, and ocean waves contain huge amount of energy, but has barely been taped. The energy density of the wave energy is about $5-10$ times higher than wind energy, and it is about $20-30$ time higher than solar energy [7], which means wave energy is a more consistent and reliable source

comparing to the other two. However, wave energy has not been fully exploited. According to the 2019 renewable global report [8], the total global renewable power is about 2017 GW, the total hydro renewable power is about 1096 GW, and the total ocean power is only about 536 MW, which is only about 0.025 % of the total global renewable power. It has been assessed that there are about 2 TW global wave power [9], but few has been captured.

Wave energy conversion devices have been studied for decades, and the devices can be classified as in three major categories, the oscillating systems, the oscillating water columns and the over-topping devices [10, 11, 12]. The typical applications are shown in the Figure 1.1. The device showing on the top in the Figure 1.1 is a classic direct drive buoy oscillating system [13], the wave motion will cause the buoy heave motion, resulting in driving the linear electrical machine inside the device to generate electricity. The one on the right down side is the oscillating water columns [14], the water height inside the capture chamber will vary alone with the waves, so the air will be driven going through the air turbine, and the turbine will drive the electrical machine to generate electricity. The one on the left down side is the over-topping device PALAMIS [15], the power extraction mechanisms has been well explained in the documentaries.

There are also many other types of wave energy conversion devices, also called wave

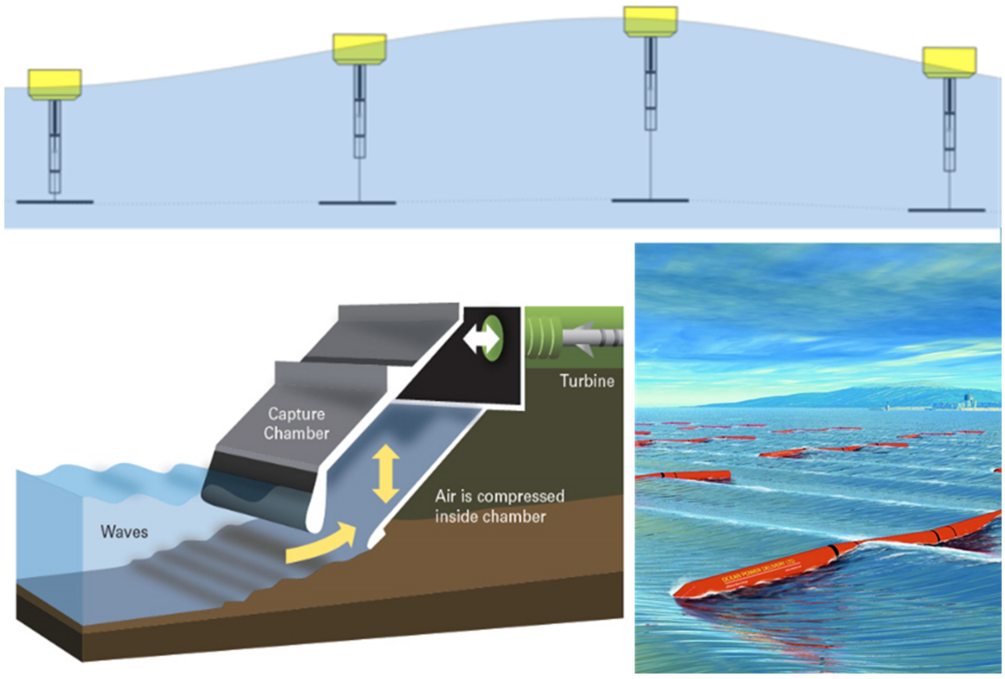

Figure 1.1: Three typical wave energy conversion applications

energy converters (WECs) are developed. The basic wave power extraction mechanisms of the WECs are similar. The mechanisms can be summarized as shown in the Figure 1.2. The WECs will have a wave power absorber, it could be a buoy in some cases, to absorb the wave power. The hydraulic power from the waves will be transmitted to the absorber, resulting in the mechanical motion of the absorber. After that, the mechanical power which carried by the absorber can be transmitted through medias, those media could be mechanical transmission system such as gear systems, also could be air, hydraulic oils, water, etc. The media can transmit the power to either turbines or directly to the generators, and then the generator can be driven to generate electricity. In this way, the wave hydraulic power can be absorbed and converted into usable electrical power which is the so-called WEC wave-to-wire,

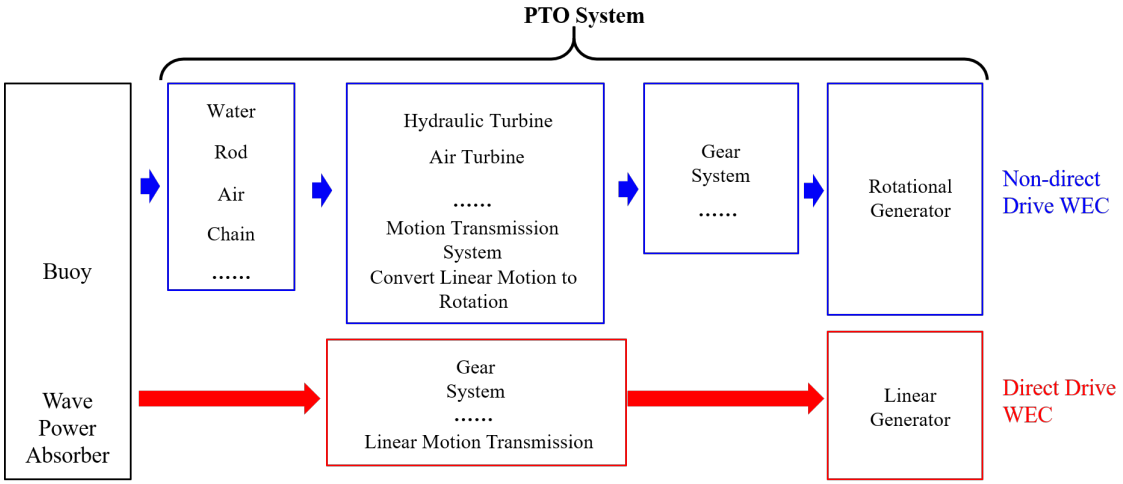

Figure 1.2: Basic mechanisms of WECs

and all the components connected to the WEC buoy which convert the wave power into electrical power are called power take-off (PTO) systems.

In the Figure 1.2, those kinds of WECs which use buoy motions to drive generators directly are called the direct-dirve WECs. Comparing to the non-direct-drive WECs, the direct-drive WECs have the merits of simplified transmission systems and higher power transmission efficiencies [16]. In most cases, the direct-drive WECs are not designed for large scaled WEC applications due to the physical constraints of the mechanical transmission systems. Linear electrical machines (LEM) are mostly common implemented on the direct-drive WECs to get rid of the complex inter-media transmission systems as in the non-direct-drive WECs, and the translator of LEM is driven directly by the buoy.

Chapter 2

Research Background

The main reason why the wind and solar energy are so preferred to the wave energy is that the wave energy levelized cost is high. According to the report from the U.S. department of energy [17], the wave energy levelized cost is about 40 times higher than the utility grid, about 20 times higher than the solar and on-shore wind energy, and about $10 - 15$ times higher than the off-shore (on sea) wind energy. How to decrease the high levelized cost of the wave energy would be the main challenge in the wave energy conversion development.

How to increase the wave energy conversion efficiency could be the key to decrease the levelized cost. The ocean waves are unpredictable, so the energy conversion procedures are more difficult to control comparing to the wind and the solar energy.

Strong waves will bring significant power fluctuations, and lack of waves will result in no power generated. Furthermore, slow wave motions will require significant control force for the buoy control, rendering low generating efficiency in the electrical machine, especially on the direct-drive wave energy converters (WECs) since the electrical machine will provide the required control force directly. Large-scaled WECs, with hydraulic systems (non-direct-drive) can provide significant control force to extract power from aggressive waves, but the overall extraction efficiency is low due to the slow responses of the hydraulic system and the complex energy conversion mechanisms [18].

To improve the WEC PTO performances, the direct methods are improving the electrical machine generating efficiencies. The LEM performances on WECs have been discussed in [19], [20] and [21]. A light-weight translator to decrease the LEM response delay is applied in [19], and in [20, 21], permanent magnet layout and field effect design of the LEM are discussed. Moreover, an electrical machine design with novel superconductor technology is discussed in [22]. The technology has been applied on large-scaled LEM to minimize the LEM power loss for wave power harvesting. However, few of these researches consider the actual electrical PTO constraints, or include the power loss impacts and LEM design efforts on the WEC buoy control performances. Besides, the cost of improving the LEM hardware design is not considered, which dose not meet with the main challenge that decreasing the levelized cost of the wave energy. Meanwhile, improving the WEC PTO design may improve the WEC performance in

some conditions, but this solution is not robust for all wave conditions.

Numerous buoy control schemes, such as impedance matching, model predictive controls, have been presented in the literature [10, 23, 24]. All the control schemes have proposed promising energy harvesting results in ideal conditions to improve the WEC energy harvesting performances, and many of the control theories have been validated on real devices [25, 26]. However, few of these control schemes have considered the WEC PTO effects. The real PTO will have losses and constraints. Meanwhile, the PTO dynamics will have significant impacts on the buoy control schemes since most of the control schemes rely on buoy hydrodynamics and ideal PTO assumptions, such as in [18], the hydraulic PTO effects on the WEC energy extraction has been discussed, and in [27], the electrical machine copper loss is considered to reduce the electrical PTO losses. The real electrical energy extraction result would be far from the ideal results with actual PTOs. The WEC wave-to-wire demands controls which are designed from the global point of view, such as the optimization of the wave-to-wire to achieve the optimal energy extraction results. However, the computational cost would be significant due to the complex and highly non-linear dynamics in the wave-to-wire. Furthermore, the model-based control schemes are highly relying on accurate dynamic modeling and average wave status. Slight uncertainties and inaccurate occurrences will render results that are far away from the optimal ones. More efforts of generating a high-fidelity wave-to-wire model is introduced in [28] to support the future buoy model-based control design. How to design a control strategy

from the global point of view, and considering all the uncertainties and inaccurate occurrences will be a great challenge.

Another choice for WEC wave-to-wire control design is the machine reinforcement learning (RL). Recently, the machine learning techniques experienced explosive growth and are shown promising performance in conducting complex tasks [29, 30, 31, 32]. A function approximator is typically implemented (e.g., the neural network) to approximate the complex dynamics of the environment, which makes the machine learning technique data driven or even model-free. In the context of the previous-mentioned challenge (cannot isolate control design from the wave-to-wire model), it is therefore highly desired to introduce the machine learning techniques to wave energy conversion.

Many of the WEC buoy control schemes have proposed promising wave energy extraction results in ideal conditions, however, few of them have been assessed on the direct-drive WECs with real PTO. The actual energy extraction performances of the state of the art buoy control schemes, such as impedance matching controls, and model predictive controls, need to be evaluated. Studying the PTO effects, such as PTO loss model and the actual PTO constraints, would be necessary to obtain the solutions for improving the PTO performances and eliminating the bias between the results based upon the actual conditions and the ideal conditions.

In the beginning phase of this research, the electrical PTO static model will be discussed. The electrical PTO static model can be applied to fast assess the available wave energy for various WEC designs in different ocean areas according to years of ground truth data. The large data base can be also applied for wave energy statistical study, energy storage system sizing, etc. Then, the electrical dynamic model will be implemented to the buoy dynamic model. The actual dynamic behaviors of the PTO will be discussed, so will the PTO loss model. By studying the PTO behaviors and the loss model, the solutions for improving the PTO operation efficiencies can be obtained. At last, in this research, the machine RL controlled PTO will be proposed, and the PACWave [33] data will be applied as inputs to evaluate the WEC energy extraction performances. By comparing the results from the model-based controls and the RL control, the improvement of the energy extraction performance can be revealed.

In the following chapters, only one kind of the small-scaled direct-drive WEC will be applied and discussed. The simplified configuration of the device is shown in the Figure 2.1. The LEM stator is mounted on the lower body, and the lower body is moored. The translator of the machine is connected to the WEC buoy directly, and it has been assumed that the connection is rigid, so that the LEM translator will follow the buoy motion all the time. All the simulation in this research is conducted by MATLAB/Simulink, and Simscape toolboxes. In Chapter 3, the numerical modeling

of the buoy linear hydrodynamics and the electrical PTO dynamics are detailed introduced. Then in Chapter 5, a simplified static WEC PTO model is introduced, which includes a static LEM model and a static electrical drive model. By implementing the PTO static model to the buoy hydrodynamic model, the actual PTO constraints and limitations are introduced to the wave-to-wire dynamics, and they will have significant impacts on the WEC actual outputs. By applying the PTO static model, the WEC wave-to-wire modeling can be replaced by the sea-state-output matrices, and they can be used for fast wave energy potential assessment or determining the dominant design parameters for the WECs. In Chapter 6, according to the WEC PTO static model, ESS sizing for actual off-shore applications is discussed. The wave energy extraction performance of years of ground truth ocean wave data is evaluated, and statistical method is also applied to improve the ESS sizing reliability. Multiple design solutions are provided. However, to study the PTO loss model and to improve the WEC performance, PTO static model is not enough. So in Chapter 7, the electrical PTO dynamic model is integrated to the buoy hydrodynamic model. By studying the PTO dynamic behaviors, the electrical drive power loss model (copper loss and nonlinear loss) is obtained, which turns out that the actual PTO will influence the buoy linear hydrodynamic model-based control significantly. The actual output is far from the optimal values. Several possible solutions for improving this situation are discussed in this Chapter as well, and the machine RL is included. So in Chapter 8, the RL control is applied on the WEC wave-to-wire control. By comparing to other

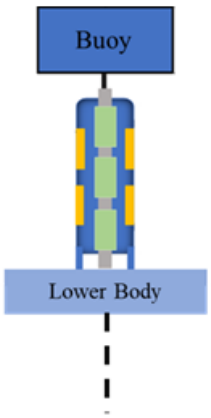

Figure 2.1: Small-scaled direct-drive WEC

model-based control schemes, the RL control cannot only achieve the maximum mean extraction power, but also provides the best output power quality. To further testify the robustness, one-year PacWave ground truth ocean wave data is applied as input. The results show that the RL control can consistently extract the most energy with the best power qualities in all wave conditions. According to the research, the machine RL control is a sufficient strategy for WEC performance improvement and wave energy levelized cost decreasing. At last, the future research plan is included.

Chapter 3

WEC Wave-to-Wire Dynamics

3.1 Introduction

Only buoy heave motion (1 degree of freedom) will be considered in this research, and it has been assumed that the buoy heave motion hydrodynamic is following the linear hydrodynamic, since the WEC design is a small-scaled device with such a small buoy displacement ($\pm 1.5\ m$), which makes the linear hydrodynamic be sufficient. The electrical PTO model applied in this research is an equivalent circuit model. The equivalent circuit model is a widely used model in the renewable energy extraction PTO modeling [34, 35]. The equivalent circuit model includes an LEM equivalent circuit model, an inverter, a direct current (DC) drive circuit. The DC circuit includes

a resistance and an constant voltage source as the infinite energy source/sink. The direct-quadrature (dq) transformation for the alternating current (AC) LEM control is also included in this chapter. The inverter in this research is assumed to be ideal and it can fully support the LEM control. All these dynamic models will be applied in the following chapters.

3.2 Buoy Heave Motion Dynamics

There are three kinds of waves being considered in this research while the buoy engaging with waves. A simplified drawing has been shown in the Figure 3.1. According to the Figure 3.1, there will be incident waves, diffracted waves and radiated waves while the buoy engaging with waves [36]. Based upon the former section, the LEM translator connects to the buoy rigidly and provides a control force u. If only the buoy heave motion is considered, the buoy heave motion dynamic equations can be expressed as

$$m\ddot{z} + F_s + F_r = F_e + u \tag{3.1}$$

where the m is the buoy inertia, z is the buoy displacement, F_s is the hydro-static force, which is the sum of the buoyancy and gravity, F_r is the radiation force, which is caused by the radiated wave potential, F_e is the wave excitation force, which is caused

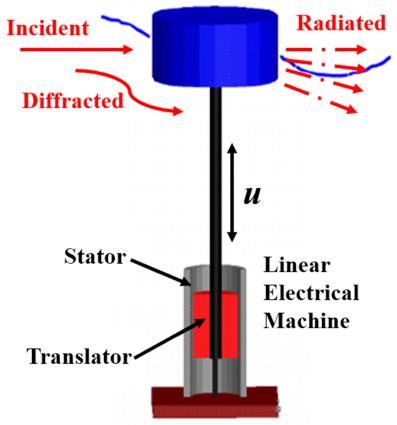

Figure 3.1: Direct drive WEC engages with waves

by the incident wave potential and the diffracted wave potential and u is the control force, which is provided by the LEM translator. According to the Eq. (3.1), the buoy absorbed and transmitted power from the waves to the LEM can be expressed as

$$P_{mech} = u\dot{z} \tag{3.2}$$

where P_{mech} is the buoy transmitted mechanical power.

Based upon Eq. (3.1), applying the linear hydrodynamic model [10], the buoy heave motion dynamic is expressed in state-space as

$$\begin{aligned} \dot{x}_1 &= x_2 \\ \dot{x}_2 &= \frac{1}{M_t}(F_e + u + F_r - B_v x_2 - K x_1) \end{aligned} \tag{3.3}$$

where the x_1 and x_2 are the two states, buoy displacement and velocity respectively,

the M_t is the total mass of the buoy which is the sum of the rigid body mass and the frequency dependent added mass,

$$M_t = m_r + m_{add,\infty} \tag{3.4}$$

the B_v is the viscous damping, which can be approximated linearly by,

$$B_v = \frac{1}{2}\rho C_d A \bar{v} \tag{3.5}$$

and the K is the linear hydra-static coefficient. The radiation force F_r in the equation is calculated by convolutions integral originally [37], but can be approximate in state-space as:

$$\begin{aligned} F_r &= -C_r x_r \\ \dot{x}_r &= A_r x_r + B_r x_2 \end{aligned} \tag{3.6}$$

where the radiation matrices A_r, B_r, and C_r can be obtained from the frequency dependent radiation damping and added mass, which are generated from Nemoh [38]. The excitation force can be expressed as

$$F_e = \sum_{n=1}^{N} \Re(\tilde{F}_e(\omega_n)\eta(\omega_n)e^{i(-\omega_n t+\phi_n)}) \tag{3.7}$$

where $\tilde{F}_e(\omega_n)$ is the frequency (ω_n) dependent excitation force coefficient which can

also be obtained from Nemoh. Furthermore, $\eta(\omega_n)$ is the frequency dependent wave elevation and ϕ_n is the nth random phase shift. A Bretschneider wave spectrum is applied in this research for the irregular wave.

3.3 Electrical Machine Modeling for WECs

Electrical machine, as a significant component of the WEC PTO system, has been studied and improved for decades. Unlike the wind power applications, the WEC devices require excessive control force from the PTO in slow motions. For large-scaled WEC applications, the hydraulic PTO, including the double-acting hydraulic cylinder, the hydraulic motor, etc., will be applied to convert the slow motion power flow into higher rotational speed power flow to achieve high electricity generating efficiency for the electrical machine. The hydraulic PTO performances have been evaluated in many researches, such as [18]. However, for direct-drive WECs, the electrical machine, in most cases the LEM, will need to provide the required control force directly to the WEC buoy to fulfill the control requirements.

3.3.1 Equivalent Circuit Model and dq Transformation

The LEM modeling can be converted into general rotational electrical machine modeling by applying the equivalent radius r_{eq}, and it relates to the LEM design parameter pole pitch. The equivalent circuit model of the permanent magnet synchronous electrical machine has been widely used in modeling [34, 35], and it is shown in the Figure 3.2. In the Figure 3.2, the v_{abc} and i_{abc} are the terminal voltage and current accordingly in three-phase, the R_s is the internal resistance and the L_s is the inductance. The dynamic equation of the equivalent circuit model can be expressed as

$$e_{abc} = R_s i_{abc} + L_s \frac{di_{abc}}{dt} + v_{abc} \tag{3.8}$$

where the e_{abc} is the induced voltage which can be determined by

$$e_{abc} = \psi_f \omega_e sin(\theta_{e,abc}), \tag{3.9}$$

the ψ_f is the field magnetic flux, the ω_e and the θ_e are the machine electrical rotational speed and displacement. For LEM, the translator linear velocity ($\dot{z}$) can be converted into rotational speed by applying the equivalent radius r_{eq}. So the ω_e and the θ_e of

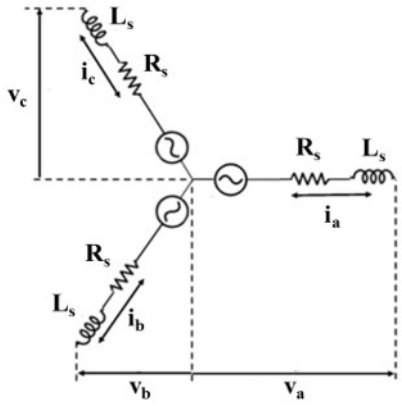

Figure 3.2: Permanent magnet synchronous electrical machine equivalent circuit model

the LEM are determined by

$$\omega_e = n_p \frac{\dot{z}}{r_{eq}}$$
$$\theta_e = \int \omega_e \tag{3.10}$$

where the n_p is the machine pole pair number.

To study and control the electrical machine behaviors directly, the dq transformation will be applied. The dq transformation has been well documented in [39]. The basic transformation process is shown in the Figure 3.3. The three-phase voltage and current can be converted into two-phase (α β) reference frame, then rotate the α β frame along with the machine electrical speed ω_e, the AC signal can be converted into the dq reference frame, which is a DC-"like" signal. The transformation matrix

from three-phase frame to dq frame is summarized as

$$\Gamma = \sqrt{\frac{2}{3}} \begin{bmatrix} \cos(\theta_e) & \cos(\theta_e - \frac{2\pi}{3}) & \cos(\theta_e + \frac{2\pi}{3}) \\ -\sin(\theta_e) & -\sin(\theta_e - \frac{2\pi}{3}) & -\sin(\theta_e + \frac{2\pi}{3}) \end{bmatrix}, \tag{3.11}$$

so the outputs in dq frame are

$$\begin{aligned} e_{dq} &= \Gamma e_{abc} \\ i_{dq} &= \Gamma i_{abc} \\ v_{dq} &= \Gamma v_{abc} \end{aligned} \tag{3.12}$$

where the e_{dq}, the i_{dq}, and the v_{dq} are the induced voltage, the circuit current and the terminal voltage in dq frame accordingly. So the dynamic equations of the LEM equivalent circuit in dq frame are

$$\begin{aligned} e_d &= R_s i_d + L_d \frac{di_d}{dt} - \omega_e L_q i_q + v_d \\ e_q &= R_s i_q + L_q \frac{di_q}{dt} + \omega_e L_d i_d + \omega_e \psi_f + v_q \end{aligned} \tag{3.13}$$

where the e_{dq}, v_{dq}, i_{dq}, and L_{dq} are the induced voltage, terminal voltage, current and inductance in dq frame accordingly, R_s is the resistance, ω_e is the electrical speed of the LEM, and ψ_f is the field flux.

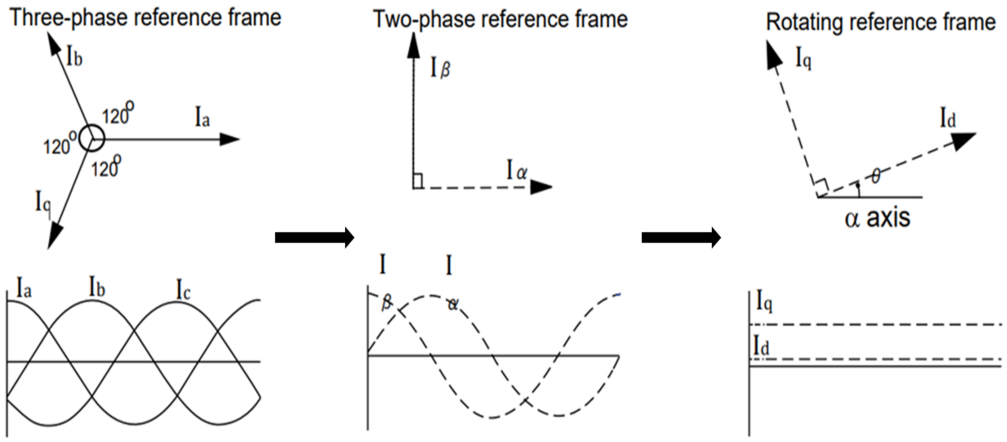

Figure 3.3: Clarke-Park transformation

3.4 Inverter and DC Drive Modeling for WECs

3.4.1 Electrical Machine Control

Based upon the LEM dynamic equations (Eq. (3.16)) in the former section, the WEC buoy control force u (Eq. 3.3) can relate to the LEM current i_{dq} by applying

$$u = \sqrt{\frac{3}{2}} \frac{n_p}{r_{eq}} (i_q \psi_f + (L_d - L_q) i_d i_q). \tag{3.14}$$

The $i_{d,ref} = 0$ [40], and the LEM current i_q is controlled based upon the reference control force signal to fulfill the buoy control requirements to integrate the LEM equivalent circuit model to the buoy dynamic model.

In order to generate the desired PTO control force to optimize the performance of the WEC, a reference control signal ($F_{PTO,ref}$) will be sent to the PTO unit and will be tracked by using the LEM. The $F_{PTO,ref}$ will be determined by different control schemes (e.g., model-based controls or deep reinforcement learning) which will be discussed in the following chapters. The $F_{PTO,ref}$ will be first converted into the reference current signal $i_{q,ref}$ by

$$i_{q,ref} = -\sqrt{\frac{2}{3}} F_{PTO,ref} \frac{r_{eq}}{n_p} \frac{1}{\psi_f + (L_d - L_q) i_d}. \tag{3.15}$$

It is noted that in this equation, the $i_{d,ref}$ is not directly applied in solving the $i_{q,ref}$, since the instantaneous i_d may not converge to the reference signal yet. To converge the current to the reference signals, the Proportional-Integral (PI) control law will be applied to determine the desired voltage input of the LEM

$$\begin{aligned} v_{d,ref} &= -K_{i,d} \int i_d dt - K_{p,d} i_d \\ v_{q,ref} &= -K_{i,q} \int (i_q - i_{q,ref}) dt - K_{p,q} (i_q - i_{q,ref}) \end{aligned} \tag{3.16}$$

where $K_{i,d}$ and $K_{i,q}$ are the integral gains in the dq frame respectively and $K_{p,d}$ and $K_{p,q}$ are the proportional gains in the dq frame accordingly.

3.4.2 Inverter and DC Drive

The inverter and simplified DC drive circuit is shown in the Figure. 3.4. The inverter has been assumed to infinite switching frequency and can fully support the PI controllers for the LEM control. In the DC drive, a constant voltage source V_s is implemented as an infinite energy source/sink. The R_{line} is the DC circuit resistance, the i_{dc} is the DC current, and the V_{dc} is the inverter input/output voltage. Based upon the assumptions, the DC/AC voltage and current are following the correlations as [41]:

$$\begin{aligned} i_{dc} &= \frac{1}{2}\sqrt{\frac{3}{2}}(\cos(\phi)i_d + \sin(\phi)i_q) \\ V_{dc} &= V_s - R_{line}i_{dc} \end{aligned} \tag{3.17}$$

where ϕ is the AC voltage phase in the dq frame, and it can be determined by

$$\begin{aligned} v_d &= \frac{1}{2}\sqrt{\frac{3}{2}}\lambda\cos(\phi)V_{dc} \\ v_q &= \frac{1}{2}\sqrt{\frac{3}{2}}\lambda\sin(\phi)V_{dc} \end{aligned} \tag{3.18}$$

where λ is the depth of modulation to control the magnitude of the inverter output voltage, more details of the converter dynamics are included in [41].

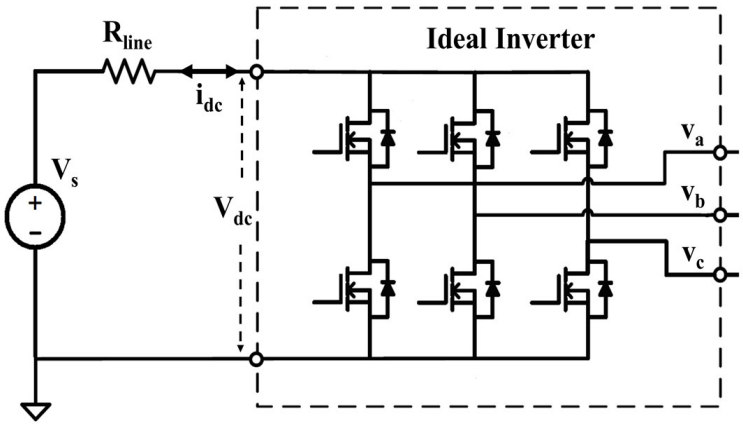

Figure 3.4: DC circuit model

According to the DC drive circuit, the WEC extracted electrical power is

$$P_{elec} = V_s i_{dc} \tag{3.19}$$

where P_{elec} is the WEC extracted electrical power.

3.5 Conclusion

The buoy heave motion linear hydrodynamic modeling and the electrical PTO equivalent circuit modeling have been introduced in this chapter. The key to integrate all the dynamic models is the reference control force signal which is determined by buoy heave motion control schemes, and the LEM PI controllers will control the PTO to fulfill the control force requirements. The state of the art buoy control schemes will be introduced in the following chapters.

Chapter 4

Model-based Buoy Control Schemes

4.1 Introduction

WEC control algorithms have been studied for decades and many of them have been applied and validated on real applications. The PTO system in the buoy passive control algorithms can be simplified as a variable damping [42]. However, by applying the passive control to WECs only can extract limited amount of wave energy comparing to the reactive power control algorithms, due to the buoy oscillation can be maximized by the reactive power control theories [43]. In the reactive power control

algorithms, the PTO system will be treated as a spring-damper system, so that the PTO will need to provide the reactive power back to the buoy to fulfill the control requirements.

In this research, several major model-based control schemes will be involved, including PD complex conjugate control (CCC), singular arc (SA) control, PD control, and model-predictive-like controls such as predictive control (MPC) and shape-based (SB) control. All the involved control schemes have been well documented in the literatures [10, 24, 43, 44]. The PDCCC control and SB control will be detailed explained in the following sections, other control schemes will not be included in this chapter due to this research is not model-based control focused.

4.2 Complex Conjugate Control Algorithm

The complex conjugate control, one typical reactive power control algorithm, will be applied in this research. The control algorithm has been well explained in [43]. To achieve the maximum extracted energy, the buoy motion and the wave motion need to be in phase all the time according to the Eq. (3.2). For regular waves (with only one frequency ω_i), the buoy heave motion dynamics in the Eq. (3.1) can be expressed

as

$$m_i\ddot{z}_i + c_i\dot{z}_i + k_i z_i = A_i sin(\omega_i t + \phi_i) + u_i \tag{4.1}$$

where the m_i is the buoy total mass with the one frequency regular wave as in the Eq. 3.4, z_i is the buoy displacement, c_i is the total viscous damping on the frequency, and k_i is the hydro-static coefficient. The excitation force F_{ei} can be re-written as a sinusoidal force $A_i sin(\omega_i t + \phi_i)$. The A_i is the force amplitude, the ω_i is the frequency and the ϕ_i is the phase. The reference control force signal u_i from PD controller is presented as

$$u_i = -K_{pi} z_i - K_{di}\dot{z}_i \tag{4.2}$$

where the K_{pi} and K_{di} are the proportional and derivative control gains accordingly, z_i and $\dot{z}_i$ are the buoy displacement and velocity which are effected by the regular wave. Substitute the Eq. (4.2) to the Eq. (4.1), the buoy dynamic equation in regular wave is

$$m_i\ddot{z}_i + (c_i + K_{di})\dot{z}_i + (k_i + K_{pi})z_i = A_i sin(\omega_i t + \phi_i). \tag{4.3}$$

According to the Eq. (4.3), to make the buoy velocity in phase with the wave excitation force, the proportional control gain K_{pi} is determined by

$$K_{pi} = \omega_i^2 m_i - k_i. \tag{4.4}$$

According to the complex conjugate control, the control impedance K_{di} should equal to the real part of the mechanical impedance c_i [12], so that the required control force u_i for regular waves is obtained ((4.2)). For irregular waves with more frequencies (ω_{1-n}), the total excitation force F_e can be estimated by $\sum_{i=1}^{n} A_i sin(\omega_i t + \phi_i)$, so the total proportional and derivative control gains K_p and K_d are

$$\begin{aligned} K_p &= \sum_{i=1}^{n} K_{p,i} \\ K_d &= \sum_{i=1}^{n} K_{d,i}. \end{aligned} \tag{4.5}$$

By applying the total K_{pd} control gains, the reference control force signal is obtained ((4.2)).

4.3 Shape-based Control Algorithm

The SB control developed in [24] is assuming the velocity of the device can be approximated by Fourier series

$$x_2 = \frac{a_0}{2} + \sum_{n=1}^{N_w}(a_n \cos(\omega_n t) + b_n \sin(\omega_n t)) \tag{4.6}$$

where a_0, a_1, ...a_{N_w} and b_1, b_2, ...b_{N_w} are unknown coefficients. Therefore, the displacement (x_1) and acceleration ($\dot{x}_2$) of the device are computed by integrating and differentiating the velocity. According to the Eq. (4.6), the required control force is in terms of approximated states as

$$u = M_t \dot{x}_2 + c x_2 + K x_1 - F_e \tag{4.7}$$

where the M_t, c, K and F_e have been detailed explained in the Section 3.2. While the required control force is approximated, the associated energy production in finite horizon can be expressed as

$$W = \int_0^{T_H} (-u x_2) dt, \tag{4.8}$$

which is a function of the Fourier coefficients, so that the energy production is maximized by optimizing the Fourier coefficients and the corresponding optimization problem is formulated as

$$\text{Min}: \quad J = -W \quad \text{subject to} \quad \mid z \mid < z_{max} \tag{4.9}$$

where z_{max} is the displacement constraint such that the maximum stroke will not be violated. The optimal control profile is computed in a prediction horizon (The cost function presented in Eq. (4.9) will be minimized from t to $t + T_H$ at each time instant). The current control (e.g., $t + t_1$) will read the force from last control history (e.g., t to $t+$) until next update of the control history is required (e.g., $t + T_c$). The aforementioned control algorithm is summarized in Algorithm 1, where T_c denotes the period that the control history will not be updated and the selected T_c has to be smaller than the selected T_H to make the control be meaningful. More details of the SB control are found in [24].

while $t < T_{end}$ **do**
  while *mod(t,*T_c*) == 0* **do**
    1. Initialization of the Fourier coefficients
    2. Minimize the cost function in Eq. (4.9) within the prediction horizon ($[t, t + T_H]$)
    3. Save the control history
  end
  Apply the control at time t from the saved history
end

Algorithm 1: SB control algorithm

4.4 Conclusion

Two buoy hydrodynamic model-based control schemes have been introduced in this chapter, the PDCCC is one of the state of the art impedance matching control schemes and the SB is one of the state of the art model predictive like control schemes. They can represent most of the up-to-date model-based control schemes in the buoy motion control area. The PDCCC control will be applied on the WEC while the buoy is integrated to the PTO static model in Chapter 5, and the performance of all other involved model-based controls (SA, PD, MPC, SB) will be assessed and compared to the machine RL in the following Chapter 7 and Chapter 8.

Chapter 5

Electrical PTO Static Model for Wave Energy Conversion Assessment

5.1 Introduction

The procedure to design and size the PTO and ESS system for a WEC system is a challenge. Current research has yielded the buoy shape design [45] and the dynamic control design [46] efforts to harvest the optimal theoretical wave energy. However, the total system optimality does not reflect the actual generated energy in the PTO and

ESS electrical drive since the electrical machine limitations and the electrical power losses are neglected. Wave-to-wire modeling is complex and the computational cost is significant, especially while processing the ground-truth ocean wave date in years. This chapter presents a novel methodology and procedure of integrating the PTO and ESS static model to the WEC buoy dynamic model while considering the electrical machine limitations. This approach can increase the PTO electrical drive design and sizing efficiency, accuracy, and specificity. Considering PTO operation constraints will correct the deviation between the buoy theoretical optimal harvesting power and the actual generated power in the electrical drive. The rule-based control strategy applied to the PTO will increase the electrical drive design flexibility instead of being excessively over-engineered as is a typical case.

The WEC power output in this chapter is calculated based upon ground truth ocean data from Martha's Vineyard Coastal Observatory [47]. The ground truth data is available on their website. A small-scaled WEC system with a permanent magnet linear electrical machine (PMLEM) will be discussed in this chapter, the device configuration sketch is shown in Chapter 2 Figure 2.1. The impedance matching control theory, PDCCC control (as in Section 4.2), has been applied on the WEC buoy control to increase the extracted power maximumly in this chapter.

5.2 Ground Truth Data Case and Ideal Power Calculation

Many studies have shown the modeling effort of wave energy resources characterization and assessment. In [48], the Simulating waves nearshore numerical model is introduced and validated for wave energy estimation in the U.S. east coast region from the Gulf of Maine to South Florida. Another research [49] evaluates different spectral wave models and applies extreme wave heights correction to present the extreme wave condition better. Pacific ocean wave study, such as PacWave report [33], have included ground-truth ocean wave information. In this chapter, the ground-truth ocean wave data is measured and collected by the Woods Hole Oceanographic Institution, on their Martha's Vineyard Coastal Observatory near the south beach in Edgartown, Massachusetts, U.S.. The observatory infrastructure includes an air-sea interaction tower, located 3 km south of Martha's Vineyard, and a 12-m underwater node, located 1.5 km offshore [47]. The ocean wave measurements are recorded and updated as one dataset every 20 mins on the website. One dataset includes significant wave height (H_s) and significant wave period (T) of swell and wind waves. The data of year 2015 has been selected in this chapter. There are 25,116 samples recorded from January 1 3:20 am. to December 31, 12:00 pm, 2015. In this paper, only when both H_s and T of both swell and wind waves are available, the dataset is considered

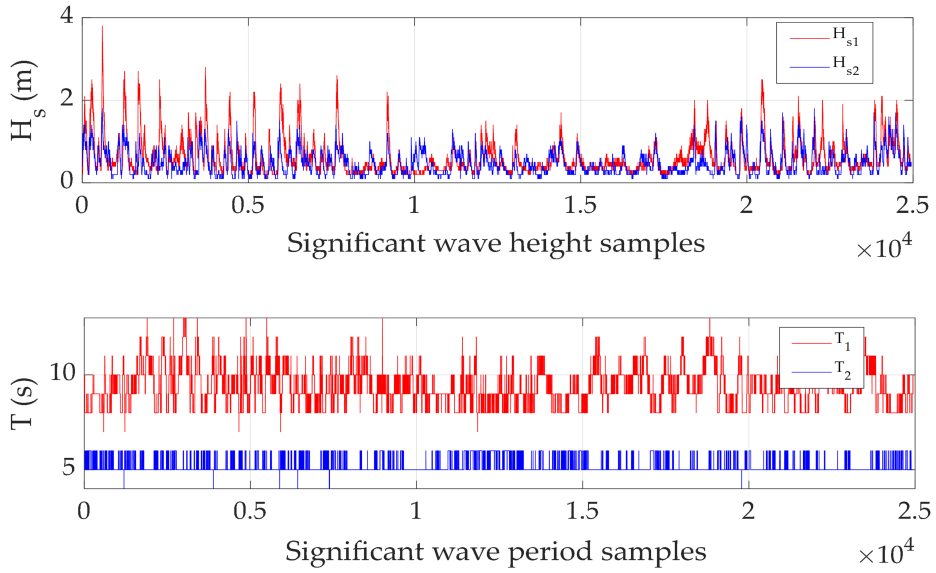

Figure 5.1: 2015 ground truth ocean wave data input H_s (top) and T (bottom) time series with 20-min time step

as a usable one. According to the standard, there are a total of 24,950 usable samples in 2015. All these usable datasets are assumed to be time continuous. In this way, the input time series of the whole year 2015 can be generated, as shown in Figure 5.1.

Based upon the ground-truth input, the WEC mean extraction power calculation algorithms is shown in the following Figure 5.2. The inputs in the Figure 5.2 ($H_{s1,2}$ $T_{1,2}$) are the ground-truth ocean swell and wind waves. The bi-modal spectrum can be generated by a standard 2-parameter equation as

$$S(\omega_i) = \sum_{j=1}^{2} \frac{131.5 H_{s,j}^2}{T_j^4 \omega_i^5} \exp[-\frac{1054}{(T_j \omega_i)^4}] \tag{5.1}$$

where $S(\omega_i)$ is the power density at the frequency ω_i, ω_i is one of the selected frequencies in the frequency vector input in Figure 5.2 flow chart (blue portion), The

whole spectrum should include all the frequencies in the frequency vector. $H_{s,j}$ and T_j are corresponding to the significant wave height and period inputs of the swell and wind waves. The Wave-by-wave prediction method has been applied and it has been explained in [50]. According to the former section, the $H_{s1,2}$ and $T_{1,2}$ datasets update every 20 min, so that a 20-min long wave record will be generated. The excitation coefficient, radiation damping coefficient, frequency-dependent added mass and hydra static restoring coefficient in the orange block can be obtained by the boundary element method solver WAMIT based upon the buoy design parameters. More details about coefficients calculation are introduced in the WAMIT manual [51]. The buoy dynamic equations and the complex conjugate control algorithms have been included in the equations (4.1) - (4.5). The wave excitation force time series (F_e in green box Figure 5.2) is a $1,200$ s time series according to the generated wave record. It is calculated by the excitation wave (blue box Figure 5.2) and the excitation coefficient (orange box Figure 5.2). The time step of F_e time series is 0.57 s based upon the frequency vector input in Figure 5.2. The optimal buoy velocity (V_{op}) time series is determined by

$$V_{op} = \frac{F_e}{2K_d} \tag{5.2}$$

Integrate V_{op} time series to have the optimal buoy displacement z time series, and

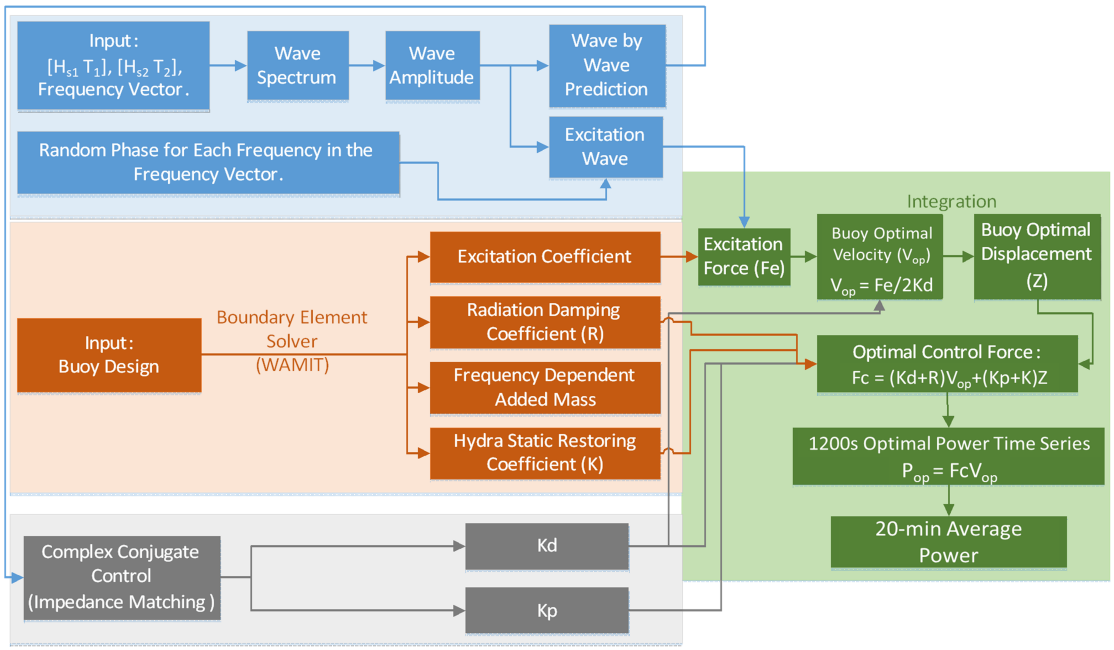

Figure 5.2: Mechanical mean power calculation flow chart

the required control force (F_c in green box Figure 5.2) is calculated by

$$F_c = (K_d + R)V_{op} + (K_p + K)z \tag{5.3}$$

where $K_d + R$ represents the system optimal damping and $K_p + K$ represents the system optimal stiffness, R and K are both determined by boundary element solver WAMIT [51] in the orange box of Figure 5.2. V_{op} and F_c time series are both $1,200$ s time series with 0.57 s time steps. The optimal extraction power (P_{op}) of the buoy is the product of F_c and V_{op}. Average the 1200 s optimal power time series of P_{op} to have one 20 min average optimal power sample.

The ideal results of the whole average power time series of year 2015 is shown in the

Figure 5.3. The different colors represent months from January to December. The x-axis is the layout of all the 20 min average power samples according to the time sequence. The annual average power is 1.77 kW, with the total energy amounting to 14.71 MWh. However, the variance of the 20 min average optimal power is significant throughout the year, especially in January, February, March, April, and October. The maximum power sample happens in January, where it is higher than 15 kW, and the lowest power is 0.025 kW in March. The maximum power samples in June, July, August, and September are relatively lower than other months. In May, November, and December, the maximum power samples are intermediate. According to the ideal power outputs, the ESS would be required for providing constant power for the sensing applications. However, sizing and designing the ESS based upon the ideal outputs is not reliable due to the actual PTO will have losses and operation constraints, resulting in the PTO modeling is demanded.

5.3 Power Take-off and Energy Storage System Static Modeling

In this section, the PTO and ESS model will be integrated to the buoy dynamic model. The inputs from the buoy dynamic model are the optimal buoy speed and required control force time series with 0.57 s time step. It has been assumed that the

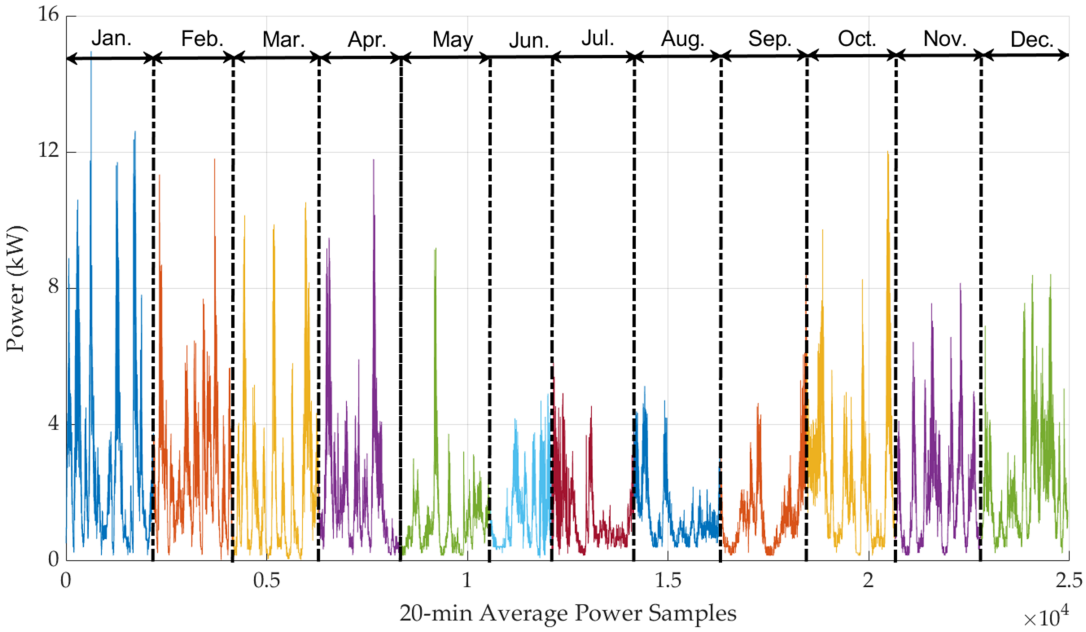

Figure 5.3: Ideal output mean power time series in 2015

PMLEM translator will follow the optimal buoy speed trajectory when the control force requirements are fulfilled. The PMLEM modeling can be converted into permanent magnet rotational electrical machine modeling by applying equivalent radius (r_{eq}) as it has been discussed in the Section 3.3. Thus, the control force requirements input will be converted into torque demands input and the optimal velocity input will be converted into optimal rotational rotor speed input in this section. The LEM dynamic can be easily coupled with the buoy dynamic model as shown in the Eq. 3.14. However, if the buoy dynamic and the LEM dynamic model update states in every 0.57 s, there will be about $5.25e7$ time steps in the whole time frame of the year 2015. The computational cost is excessive. A much more efficient method for sizing the ESS is demanded, resulting in the PTO static model is applied. In the LEM static model, the dynamic states have been assumed to be steady and no state transition

or updating are considered. So the Eq. (3.16) is simplified as

$$v_d = R_s i_d - \omega_e L_q i_q$$
$$v_q = R_s i_q + \omega_e L_d i_d + \omega_e \psi_f \tag{5.4}$$

where the current differential states di_{dq} have been neglected, which means it has been assumed that all the control force requirements have been fulfilled and the LEM has been controlled to achieve the desired i_{dq} in steady state. When the reference i_d is 0, the i_q and the F_c are following the linear correlation as:

$$i_q = \sqrt{\frac{2}{3}} \frac{F_c r_{eq}}{n_p \psi_f} \tag{5.5}$$

According to Eq. (5.4) and (5.5), Eq. 5.6, while the PMLEM operates as a generator, is a power extracting constraint for the inputs as

$$|V_{op} \psi_f| > |\sqrt{\frac{2}{3}} \frac{R_s F_c r_{eq}^2}{n_p \psi_f}| \tag{5.6}$$

The Eq. (5.6) is based upon the LEM generating efficiency constraint that the efficiency cannot be lower than 0 %. The absolute value is applied to eliminate the power flow directions. The constraint is required since the designed LEM may not be able to fulfill the control requirements for all the inputs, although it has been assumed to be in the static modeling. If the control requirements cannot be fulfilled by the

LEM as a generator, it will be operated as a motor even when there is available wave energy for extracting. Table 5.1 shows three different operation modes of the LEM.

Table 5.1
Electrical machine operation modes

Inputs	**Direction**	**Wave Power Status**	**Eq.** (5.6)	**Operation Modes**
$\begin{bmatrix} V_{op} \\ F_c \end{bmatrix}$	$\begin{matrix} + \\ + \end{matrix}$	Not available	Not applied	Mode 1: Motor
$\begin{bmatrix} V_{op} \\ F_c \end{bmatrix}$	$\begin{matrix} - \\ - \end{matrix}$	Not available	Not applied	Mode 1: Motor
$\begin{bmatrix} V_{op} \\ F_c \end{bmatrix}$	$\begin{matrix} + \\ - \end{matrix}$	Available	Fulfilled	Mode 2: Generator
$\begin{bmatrix} V_{op} \\ F_c \end{bmatrix}$	$\begin{matrix} - \\ + \end{matrix}$	Available	Fulfilled	Mode 2: Generator
$\begin{bmatrix} V_{op} \\ F_c \end{bmatrix}$	$\begin{matrix} - \\ + \end{matrix}$	Available	Unfulfilled	Mode 3: Motor
$\begin{bmatrix} V_{op} \\ F_c \end{bmatrix}$	$\begin{matrix} - \\ + \end{matrix}$	Available	Unfulfilled	Mode 3: Motor

In operation mode 1 in the Table 5.1, the LEM must provide power as a motor for the buoy to fulfill the control requirements. In mode 2, wave power is available to extract and the inputs (V_{op} and F_c) do not violate the Eq. (5.6) constraint, so the electrical machine can extract wave power as a generator. In mode 3, there is available wave power to extract, however, Eq. (5.6) constraint is violated, which means the designed LEM cannot fulfill the control requirements by the inputs. Thus, the LEM will work as a motor and provide the exact same amount of the required torque for the buoy control.

The outputs from the LEM model are current (i_{dq}) and voltage (v_{dq}) time series. i_d is assumed to be constant 0 A. Therefore, the generated power on d-axis is 0 W. Based

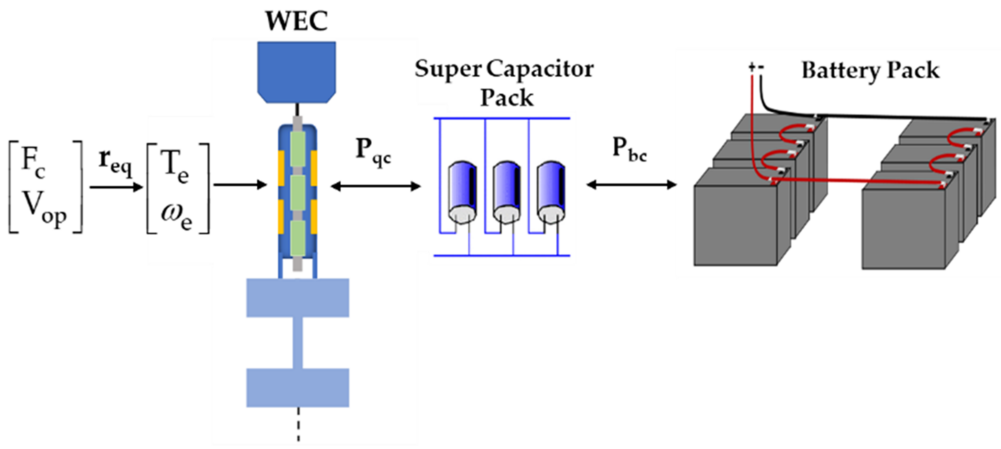

Figure 5.4: Power take-off system static model configuration

upon the static dynamic assumptions, the inputs to the following ESS components are also feed forward and static. The configuration of the static electrical drive is shown in the Figure 5.4, the super-capacitor (SC) pack will have rapid responses to fulfill the LEM control requirements. It can either store or provide energy to support the LEM operating as a generator or a motor. The LEM will provide the exact required i_q to fulfill the buoy control force requirement, and the required current between the LEM and the super-capacitor pack can be determined as well.

The energy storage module includes a SC pack and a battery pack, as shown in Figure 5.4. The equivalent circuit static modeling of the energy storage module is shown in the Figure 5.5. In static modeling, the SC/battery equivalent circuit has been simplified to a constant OCV (open circuit voltage source) with a resistor in series. The inductance and capacitance behaviors are neglected in static modeling.

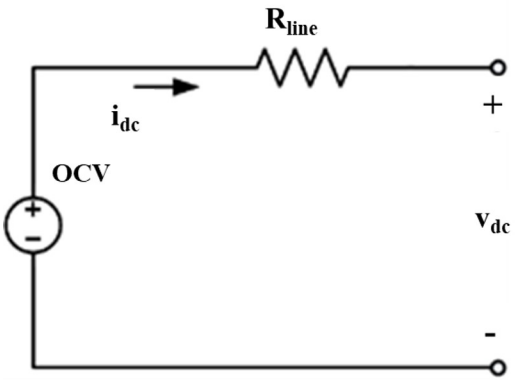

Figure 5.5: Energy storage system static model circuit

Therefore, the modeling equation is

$$OCV - i_{dc}R_{line} = v_{dc} \tag{5.7}$$

where i_{dc} is the SC/battery internal current and v_{dc} is the SC/battery terminal voltage. The battery pack aims to store the harvested energy and support the SC pack and the load in the meantime (as in the Figure 5.4).

5.3.1 Results from Static Power Take-off System

Based upon the buoy dynamic model in the Section 5.2, the optimal velocity (V_{op}) and the required control force (F_c) are both time series with 0.57 s time step. For one set of 20 min ocean wave data (H_s and T of swell and wind waves), there are $2,015$ samples in the time series. The inputs (V_{op} and F_c) of 2015 March, as an example, of the LEM are shown in Figure 5.6. The buoy-required control force in Figure 5.6 is

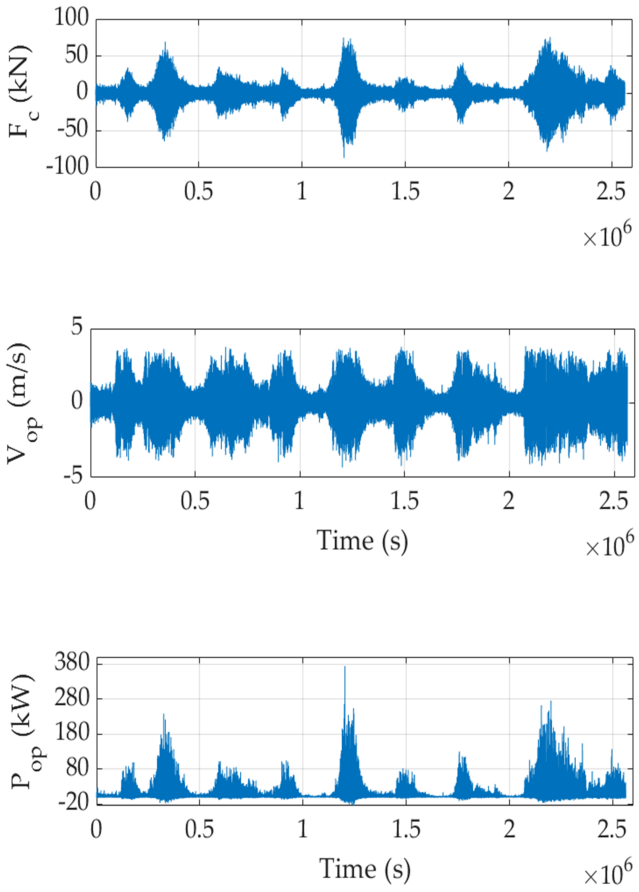

Figure 5.6: Buoy-required control force and optimal velocity inputs in March

over 50 kN, and the buoy velocity is below 4 m/s. The LEM design with large field magnetic flux can help to fulfill these requirements. The optimal power output (P_{op}) from the buoy dynamic model is the product of the V_{op} and F_c time series according to the flow chart in Figure 5.2. The positive P_{op} is the optimal harvesting power from the waves to the PTO and the negative P_{op} is the required power from the PTO for the buoy CC control.

The electrical machine outputs in dq frame are shown in the Figure 5.7. The v_q can

reach over $3,000\ V$ according to the figure. The high voltage inverter is required to convert the current from the AC to DC. To decrease the v_q, the LEM demands increased field magnetic flux, pole pair number, or lower r_{eq}, but it will cause an increased current flow in the drive. Positive P_{qc} happens when the LEM is in motor mode and providing power for the buoy control. Negative P_{qc} means the LEM is extracting power from the waves. The maximum extracting power is higher than $350\ kW$ and the maximum reverse power is smaller than $20\ kW$. The values are very close to P_{op} but in the opposite power flow direction and including the electrical losses.

The behaviors of the energy storage module (SC and battery) are shown in Figure 5.8. The i_{qc} is the current from the capacitor to the LEM. Positive current discharges the capacitor and negative charges it. The capacitor needs to provide the demanded current for the buoy PDCCC control. The i_b is the battery current, the positive current discharges and the negative charges. The battery pack will support the load and store all the energy from the capacitor. A load with $120\ W$ constant power consumption is assumed, and the battery is assumed to be an infinity energy sink in this section. Furthermore, the battery can also charge the capacitor back to the desired SOC level, so that the battery current in Figure 5.8 is the sum of the current to the capacitor and the current to the load sensor. The max charging current for the battery pack can reach $200\ A$ and the stored energy amounts to $1,168\ kWh$ in the whole month if the battery pack pre-charged level is 0. The required capacity for the

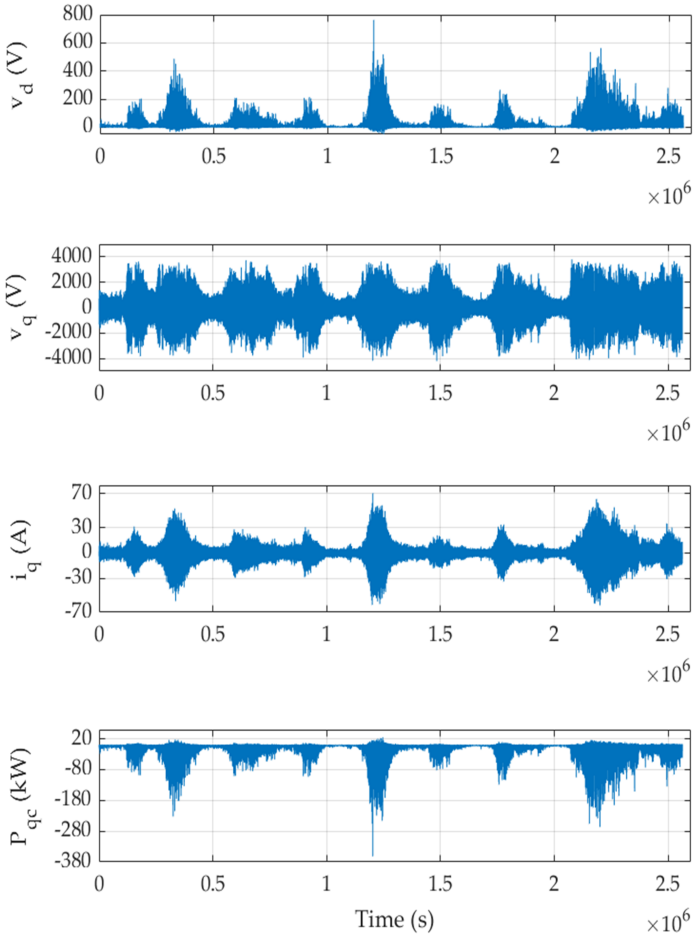

Figure 5.7: Electrical machine outputs in March

battery pack is excessive to store all the extracted energy. The designed PTO can harvest much more energy than one of the assumed load demanded.

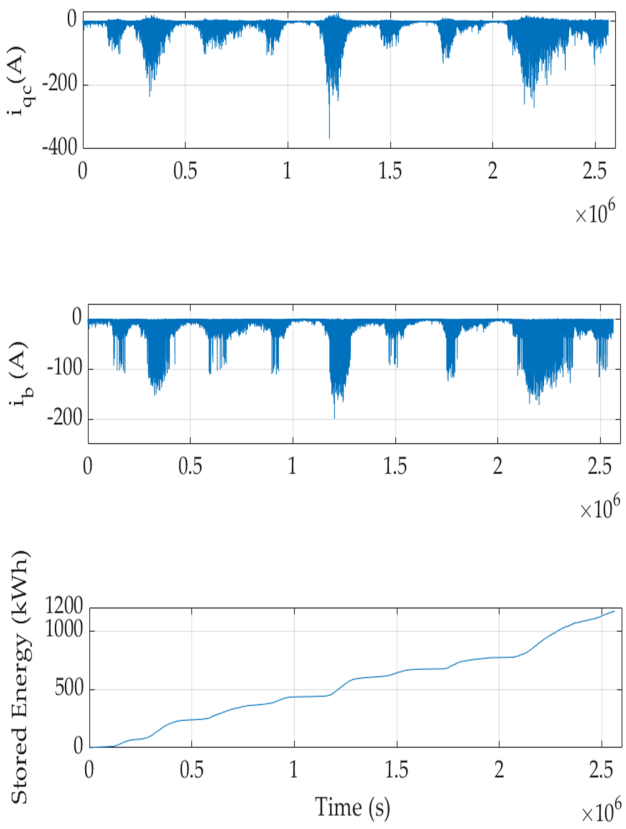

Figure 5.8: Energy storage system behaviors in March

5.4 Power Take-off Constraints and Limitations

5.4.1 LEM Operation Efficiency Constraints

The LEM efficiency varies significantly during the whole month. According to Table 5.1, the LEM does not need to fulfill any efficiency constraint (Eq. 5.6) while working in motor mode, since the buoy may still require a large control force when the oscillation speed is almost 0. However, if the generating efficiency is too low, the

small generating voltage and current outputs will be difficult to be fulfilled by the following components in the electrical drive. Concerning this, a generating efficiency constraint can be applied to filter out low generating efficiency inputs (F_e, V_{op}) and fulfill the control requirements by operating the LEM in motor mode. Based upon the static modeling (Eq. 5.4 - 5.6), the electrical machine generating efficiency is

$$\eta = \frac{3}{2}\frac{i_q^2 R_s}{T_e \omega_m} \tag{5.8}$$

where ω_m is the equivalent mechanical rotational speed (converted from V_{op} by applying r_{eq}) of the generator rotor, and $\frac{3}{2}$ is a scale factor when calculating power in dq frame. Based upon the former sections, the inputs of the LEM static model are T_e and ω_e time series, which are converted from the buoy dynamic model outputs F_e and V_{op} time series. Thus, the electrical machine generating efficiency constraint can be applied on the inputs as:

$$\frac{T_e}{\omega_e} = (100\% - \eta_b)\frac{3}{2}\frac{3 n_p \psi_f^2}{2 R_s} \tag{5.9}$$

where η_b is the efficiency boundary to filter the inputs.

Figure 5.9 shows all the generating points of March on a generating efficiency contour map of the designed LEM. The lowest efficiency is almost 0. There are no data points on the negative efficiency portion (dark blue area) owing to the generating constraints

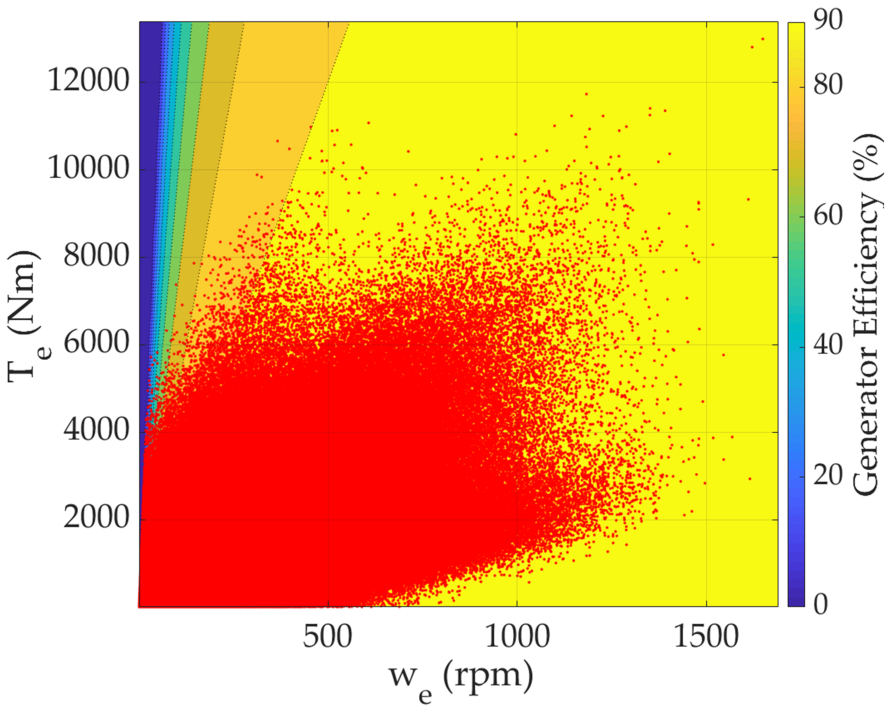

Figure 5.9: Generating points without any efficiency constraint

(Eq. 5.6). The maximum generating efficiency of the month can be above 99%. The efficiency boundary is set to 70% in Figure 5.10. After filtering, the generation time is decreased to 82.23% of the month, which was 82.89% before (29,688 inputs have been filtered out). The slight decrease in generating time can barely change the charging/discharging behavior of the ESS module. The stored energy in the battery pack decreases to 1167 kWh from 1168 kWh.

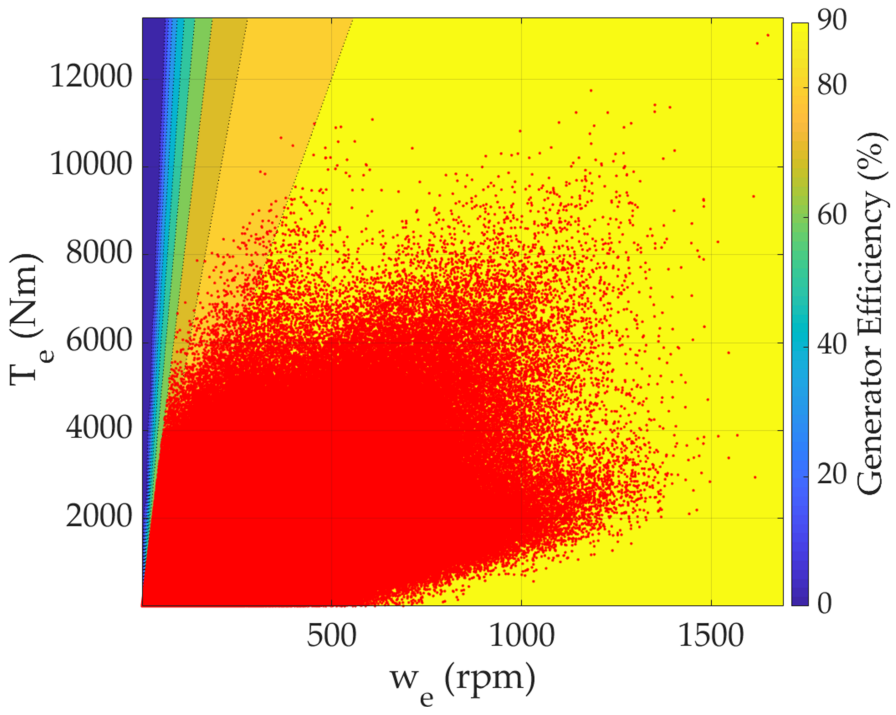

Figure 5.10: Generating points with 70% efficiency constraint

5.4.2 Required Control Force Limitation for Downsized Electrical Machine

The PDCCC control applied in this chapter will maximized the buoy oscillation to absorb the wave power maximally, so that the excessive control force is demanded from the PTO. If the electrical machine can fulfill the large control force requirement, the WEC system can operate without any breaks. On the other hand, the designed electrical machine can be downsized to extract power from small waves only, instead of generating much excess energy stored in the battery. The downsized electrical machine will be locked down and enter a safe mode when aggressive waves come to

prevent the PTO components from being crashed. The required control force output and optimal extracting power output from the buoy dynamic model will be 0 while the WEC is in safe mode. According to the Martha's Vineyard Observatory ocean wave data, one set of bi-spectrum wave data can present the wave status in a 20 min long period. Thus, if the maximum required control force of one bi-spectrum is greater than the PTO limitation, the WEC will be locked down for 20 min.

The required control force with respect to the Hs and T matrices are shown in Figure 5.11. The color bar shows the average extraction power of 20 min. The average extraction power increases with PTO maximum control force limitations (MCFL) increase. When the MCFL is 10 kN, only small waves can be captured by the buoy, so the average extraction power is low. If the MCFL is increased to 50 kN, the average extraction power can reach over $3,000$ W.

The matrix in Figure 5.11 is for a single spectrum. The maximum required control force threshold of the bi-spectrum can be determined by the sum of the maximum required control force of the swell spectrum and the wind waves spectrum. Therefore, the maximum bi-spectrum MCFL PTO constraint can be expressed as

$$MCFL_{bi} = MCF_{H_{s1}T_1} + MCF_{H_{s2}T_2} \tag{5.10}$$

where $MCFL_{bi}$ is the MCFL of the bi-spectrum, $MCF_{H_{s1}T_1}$ and $MCF_{H_{s2}T_2}$ are the

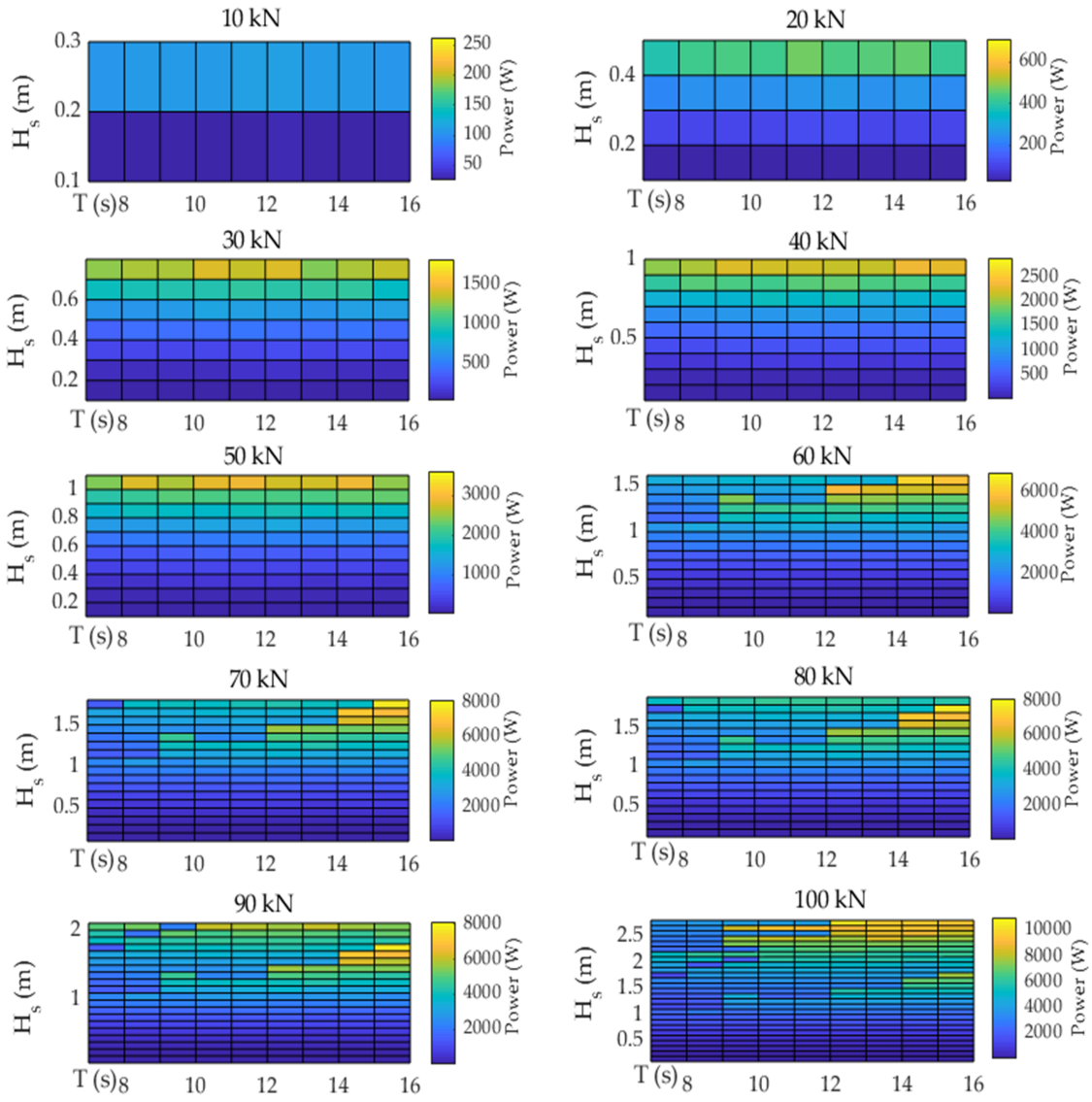

Figure 5.11: Control force limitation look-up table

maximum required control force of one set of swell and wind waves inputs. The $MCFL_{bi}$ can represent the theoretical maximum required control force of the bi-spectrum, but the actual required control force can be smaller than this value due to phase differences at the same frequency between the two spectrums. However, it is more common to use power to size electrical machines instead of the max torque the

machine can provide. Thus, the maximum power limitation (MPL) constraint for the LEM can be expressed as

$$MPL_{biG} \geq \max(\frac{\omega_{eG}(t)}{n_p} T_{eG}(t))$$
$$MPL_{biM} \geq \max(\frac{3}{2} v_{qM}(t) i_{qM}(t)) \tag{5.11}$$

where $MPL_{biG,M}$ is the MPL constraint for the bi-spectrum when the LEM is in generator or motor mode, $\omega_{eG}(t)$ and $T_{eG}(t)$ are the rotational speed and torque time series inputs to the LEM according to the bi-spectrum while the LEM is in generator mode, $v_{qM}(t)$ and $i_{qM}(t)$ are the voltage and current time series in dq frame when the LEM is in motor mode. The max power of the inputs to the LEM must not be greater than the $MPL_{biG,M}$, if it does, the inputs time series cannot be accepted by the downsized LEM and the WEC system will be locked down for 20 min.

5.4.3 Results with Constraints Applied on the Electrical Machine

The MPL_{bi} of the LEM has been set to 30 kW in this section. The constrained inputs (F_c and V_{op}) are shown in Figure 5.12. According to Figure 5.12, the continuous 0 values (gaps) are seen in the time series when the WEC is locked down. The required control force (F_c) and the optimal buoy velocity (V_{op}) will be 0 in the lockdown

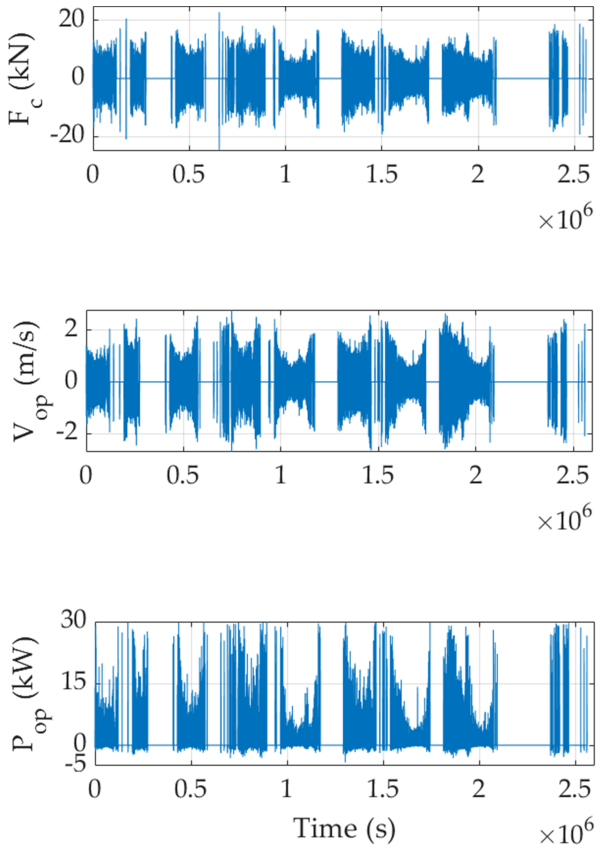

Figure 5.12: Constrained buoy dynamic inputs in March

periods, so will the optimal extracting power (P_{op}). It has been assumed that the WEC buoy will go back following the optimal velocity trajectory without any delay after releasing the lockdown. The maximum required control force is less than 25 kN, which means that only small waves can be captured by the buoy based upon the Figure 5.11 matrices. The maximum V_{op} decreases to about 2 m/s from 4 m/s compared to Figure 5.6. The maximum P_{op} is always smaller than 30 kW.

The downsized LEM has different parameter setups with smaller magnets without compromising the inputs requirements. Because the parameters have been modified,

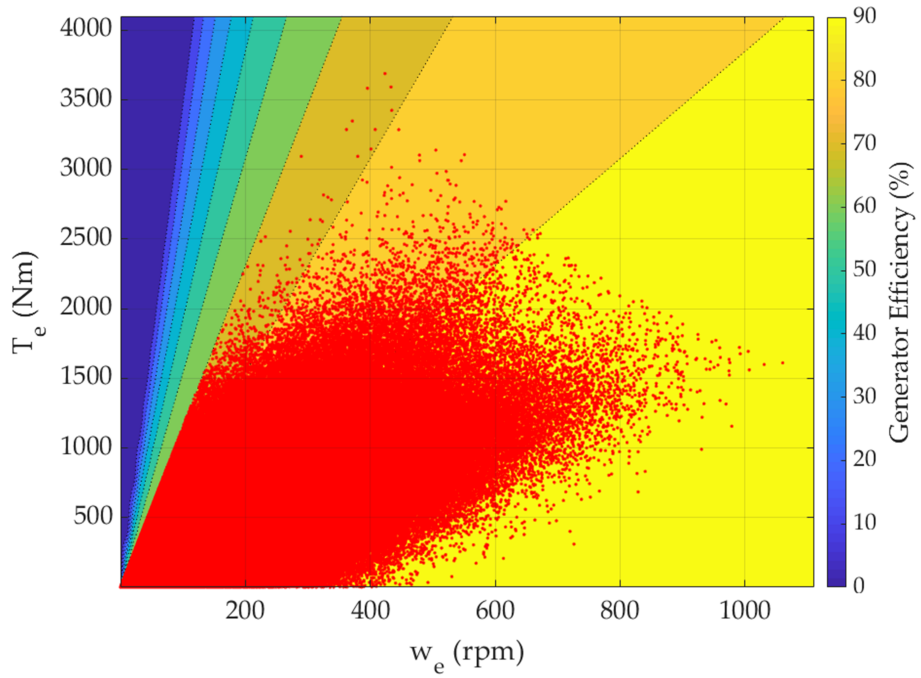

Figure 5.13: Constrained March generating contour map

the generating efficiency contour map of the LEM is changed as well. While considering the same generating efficiency constraint (70%), the updated generating efficiency contour map is shown in Figure 5.13.

The slope of the high-efficiency boundary (90%) in Figure 5.13 decreases significantly (comparing to Figure 5.10) because of the decreased magnet field flux. While applying the MPL and generating efficiency constraints, the generating time only takes a 20.64% of the whole month. The LEM outputs are shown in Figure 5.14. In Figure 5.14, the LEM output v_q decreases to lower than $1,000\ V$ from $3,500\ V$, v_d decreases to $150\ V$ from $780\ V$. The decreased voltage will increase the design feasibility for the following components in the electrical drive. The current i_q is on the

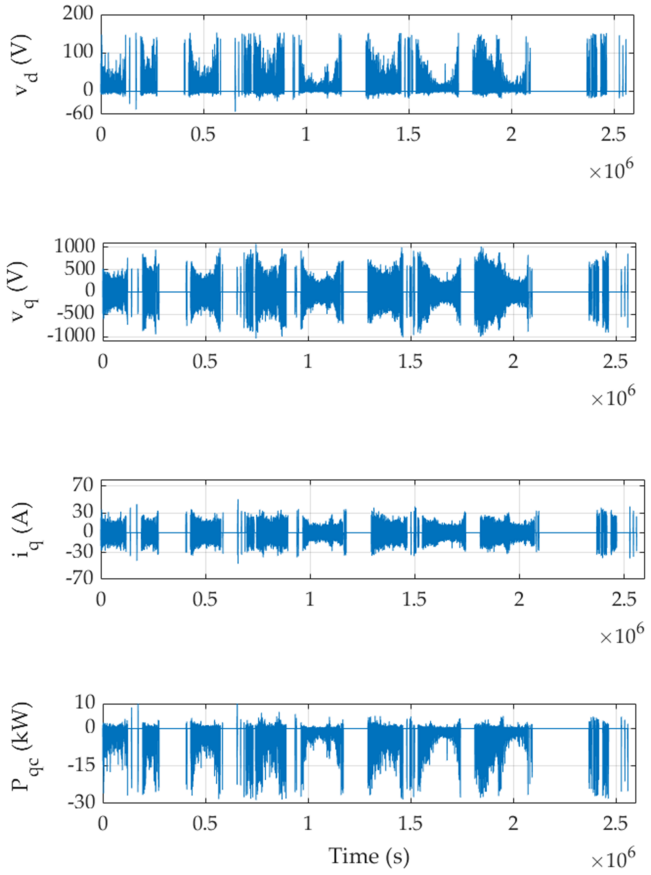

Figure 5.14: Constrained electrical machine outputs in March

same level comparing to Figure 5.7. There are no samples in the P_{qc} time series having power higher than 30 kW since the inputs have been constrained to 30 kW. With the updated parameters, the capacitor pack fully charged OCV can also be decreased (comparing to unconstrained cases). The energy storage system behaviors are shown in Figure 5.15.

According to the results in Figure 5.15, the current flows (i_{qc} and i_b) decrease significantly comparing to Figure 5.8. The current i_b is slightly higher than 0 when the WEC is shut down since the battery pack needs to keep discharging to supply the load.

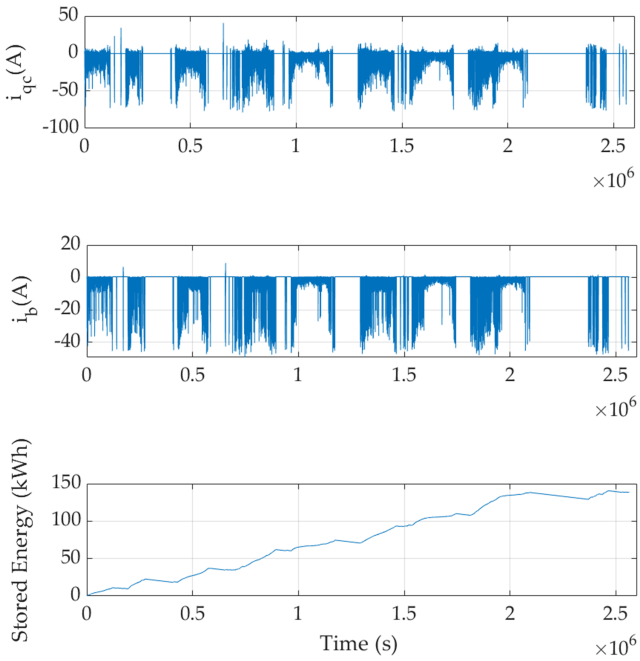

Figure 5.15: Constrained energy storage module behaviors in March

The required battery pack capacity can be decreased to 140 kWh from $1,168$ kWh in Section 5.3.1. According to the input required control force in Figure 5.12, the max control force is smaller than 25 kN, resulting in that the generating constraints have filtered generating inputs down to about 20%. Thus, the average generating power of the whole month will be even lower. With this downsized PTO, the extremely high voltage (over $3,500$ V DC) and current fluctuations requirements can be eliminated. The load power demand (constant 120 W) can still be fulfilled with the small PTO. The amount of stored energy in the battery pack is still large. Supporting multiple loads can be considered in the future to size the PTO and the battery pack in the most efficient way.

5.5 Conclusions

The PTO and ESS design cannot be isolated from the buoy dynamic behaviors and control strategy requirements, meanwhile, the WEC device and control performances assessment should also consider the PTO limits. The optimal extracting power from the buoy can be achieved only when the control requirements can be fulfilled perfectly well by the PTO. This chapter discusses the integration methodology between the buoy dynamic model and the WEC PTO electrical drive model. The electrical machine operation modes, which due to the actual device constraints, will influence the wave power extraction performance, as it has been discussed in Section 5.3. Furthermore, high demand control inputs will give stringent design requirements to the PTO and ESS components. According to the results in Section 5.3.1, the required control force can be higher than 90 kN while the translator speed is around 4 m/s. The LEM design will be very limited by this stringent demand. Instead of capturing all the optimal wave power, the PTO and ESS should be designed to fulfill the demand of selected applications and purposes. The operation constraints and rule-based control strategies introduced in Section 5.4.2 can improve the PTO and ESS design efficiency. Downsizing the PTO is another strategy which is discussed in the chapter to improve the design. By downsizing the PTO, the high voltage bus can be decreased to $1,000\ V$ from $3,500\ V$. The definitions of MCFL and MPL are also introduced in Section 5.4.2. The $H_s - T - MCFL$ matrices in Figure 5.11 can help

future PTO and ESS sizing since it relates the MCFL and the average power to the ground truth H_s and T. The static modeling of the direct drive WEC PTO electrical drive is enough to determine the dominant parameters for the PTO and ESS design. To further improve the PTO and ESS design reliability and specificity, the dynamic behaviors of actual electrical drive components can be integrated. An optimization strategy can also be applied to determine the optimal rule-based control boundaries in the future. How to apply the PTO static model on the off-shore application ESS sizing will be shown in the next chapter.

Chapter 6

Energy Storage Sizing Statistical Study

6.1 Introduction

Ocean sensing applications require sustained power to measure and collect data during extended periods in remote locations. This calls for the design of energy systems capable of delivering such stringent demands. Typical solutions include wave energy converters (WECs), which rely on wave height to actuate an electromechanical or hydraulic system [52] to generate power. However, this is not a sufficiently resilient choice as lack of waves and wind can result in no power generated, rendering the

sensors useless. The literature presents solutions in which the WECs are part of hybrid systems, with either photovoltaic [53], wind [54], batteries, and/or fuel cells [55]. However, most solutions add the energy storage or alternative generation [56] as an afterthought, rather than considering a combined design effort for both the WEC and ESS.

Offshore structure long-term performance is highly depending on the ocean environment. A robust statistical model for observed variables will improve the design reliability significantly [57]. Using Bayesian methodology to predict and estimate ocean motions is available in the literature. The long-term significant wave heights are inferred by Bayesian approach in [58], while considering extreme value theory. In [59], Bayesian networks are applied to predict the significant wave heights. But, these efforts are focused around the probabilistic estimation of oceanographic data. In this work we propagate the probabilities to represent the variations in the PTO power extraction and therefore to better inform the energy storage sizing.

In this chapter, wave power is extracted by the same wave-to-wire static model as in the Chapter 5. The inputs are the ground-truth ocean data from Martha's Vineyard Coastal Observatory record from year 2001 to 2016 [47]. The ground-truth data is used to estimate the power distribution of each sample in the whole year time-series by Bayesian statistical method. Statistical annual power output time-series are composed by the mean and standard deviation of the power distribution. The capacity

statistical tolerance for the ESS is determined based on Chebyschev's Theorem. The goal is to use the historical data to inform energy storage sizing, and eventually control decisions too.

6.2 ESS Sizing for Ocean Sensing Application

One of the ocean sensor applications requires a constant 0.12 kW power supply with a 120 V DC. According to the PTO and electrical drive static modeling in the Chapter 5, to support the ocean sensing application for working consistently the energy storage system is required due to the lack-wave-power period. According to the ground-truth ocean wave data which has been assessed in the Chapter 5 Figure 5.7, all the lack-wave-power periods are shown in the following table. Many of the periods are in different day and month, however from the sample #5492 to the sample #5557, these samples are all in one day, which will result in few wave energy being extracted during the day and the application will highly rely on the ESS in this day.

The ESS sizing logic is shown in the following Figure 6.1. In the figure, the inputs are the battery current (i_b as in Chapter 5). Integrate i_b from time 0 to time t_n to obtain the total extracted net energy at t_n. E_{net} is the net energy at different time steps. The E_{net} is used to determine the maximum value of the extracted energy which needs to be stored in the battery pack. E_{dis} is used to determine the maximum value of

Table 6.1
Wave Power Lack Periods

Index	**Date**	**Time**	**P**(kW)	**Index**	**Date**	**Time**	**P**(kW)
3864	2/24/2015	18:40	0.026	**5535**	3/20/2015	15:00	0.054
5028	3/13/2015	10:40	0.053	**5539**	3/20/2015	16:40	0.053
5037	3/13/2015	13:40	0.054	**5540**	3/20/2015	17:00	0.053
5039	3/13/2015	14:20	0.054	**5541**	3/20/2015	17:20	0.054
5040	3/13/2015	14:40	0.054	**5556**	3/20/2015	22:20	0.053
5042	3/13/2015	15:20	0.053	**5557**	3/20/2015	22:40	0.053
5492	3/19/2015	23:40	0.107	**5821**	3/24/2015	17:40	0.054
5524	3/20/2015	10:20	0.053	**5850**	3/25/2015	18:40	0.025
5525	3/20/2015	10:40	0.053	**5851**	3/25/2015	19:00	0.025
5034	3/20/2015	14:40	0.054				

the discharged energy while the wave power is not sufficient. If $E_{net}(t_n)$ is positive, it means the wave power is not sufficient (positive i_b means discharging) and the value of $E_{net}(t_n)$ is the energy that the battery pack needs to provide by time t_n. A positive $E_{net}(t_n)$ value will be integrated to the following $E_{dis}(t_{n+1})$ calculation. If $E_{net}(t_n)$ is negative (negative i_b means charging), it means the wave power is sufficient at time t_n, a negative $E_{net}(t_n)$ value will be fixed to 0 for the following $E_{dis}(t_{n+1})$ calculation. At the end, the greater one of the maximum absolute values of the E_{net} and E_{dis} is the required capacity of the battery pack. By applying the ESS sizing algorithms in the Figure 6.1 on the annual output power time series in Chapter 5 Figure 5.8, if all the energy is stored in the battery, the required capacity would be $1,168\ kWh$. The excessive required capacity of the battery pack is totally inapplicable for off-shore applications.

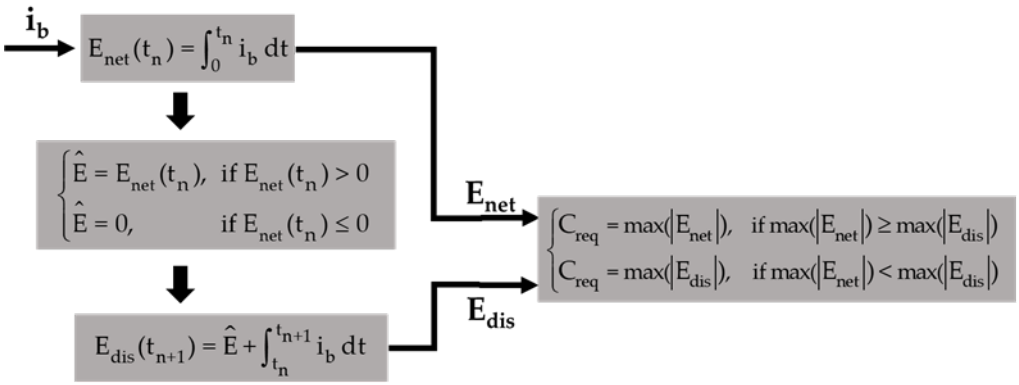

Figure 6.1: ESS Sizing Logic for Ocean Sensing Application

6.3 ESS Sizing for Downsized PTO with Multiple Loads

It has been well explained the details of PTO downsize in Chapter 5 Section 5.4.2. While supporting multiple sensor loads with the downsized PTO, all the loads will be connected to the battery pack in parallel as shown in the Figure 6.2. The required power of all the loads must be fulfilled by the PTO and ESS system. As in the former section, if one sensor load requires constant 120 W power, then the total constant power requirement is $120n$ W (n sensors have been connected).

To consider a variable number of sensors to support, with a sweep from 1 to 8, the ESS sizing optimization algorithm (Figure 6.1) will run for all the scenarios. According to Figure 5.11, there are 10 power time series being generated with respect to different MDFLs ($10 - 100$ kN), so that there are 80 optimization results. The results are

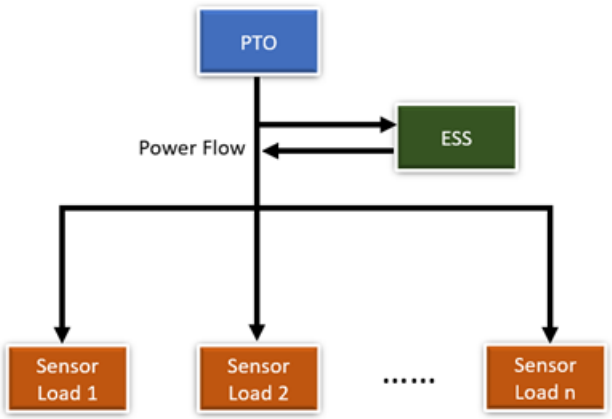

Figure 6.2: Configuration of Supporting Multiple Loads

shown in the Table 6.2. In the Table 6.2, when the MCFL is 10 kN, the required capacity is much higher than the ones with other MCFLs with respect to the same quantity of supported sensors, since the WEC device is switched into safety mode for most of the time throughout the whole year, so the extracted energy is too low to support the sensors and the ESS is the main energy source for the sensors. While the MCFL is increasing, the required capacity is decreasing when supporting the same quantity of sensors, since the increased MCFL contributes to extracting more power from the WEC to support the sensors or charge the ESS. However, analyzing the Table 6.2, the required capacity will not decrease if the increased MCFL only aids to extract more excess energy. The available wave energy at some points throughout the year is not high enough to support multiple sensors, so the required capacity is not decreasing no matter how the MCFLs have been increased. The scenario happens when supporting 2 sensors with increased MCFL from 20 kN to 100 kN. The required capacity stays constant at $18,056$ Wh. A similar scenario happens when supporting 1

sensor with MCFLs higher than 80 kN and supporting 3 sensors with MCFLs higher than 30 kN. To pursuit supporting the sensor with the smallest PTO and ESS, the required MCFL must be at least 20 kN with an $8,880$ Wh ESS to support one sensor. To pursuit the smallest sized ESS, the MCFL must be at least 80 kN with a 702 Wh ESS. To pursuit supporting the maximum number of sensors possible, 3 sensors with 30 kN MCFL and $50,505$ Wh ESS is the combination as the ESS is increased by about 468% comparing to $8,880$ Wh. 2 sensors with 20 kN MCFL and $18,056$ Wh ESS is an intermediate choice as the ESS is increased by about 103% comparing to $8,880$ Wh. The required capacities showing in red in the Table 6.2 are considered as acceptable ESS size for off-shore applications, the ones outside the red block are too excessive.

6.4 Static PTO Mean Power Outputs Estimation

To estimate the 20 min mean power output time-series for each year, a power extraction matrix is generated based upon the ground truth data by applying the PTO static model (Section 5.3). Figure 6.3 shows the 3-D power extraction matrix, similar to the Figure 5.11. According to the recorded ocean data, the usable significant wave height (H_s) and period (T) in the 16 years vary from $0.1 - 3.8$ m and $7 - 16$ s respectively. Two examples of power output time-series for the year 2010 and 2014 are shown in Figure 6.4. The maximum extracted power by the PTO in the 16 years is

Table 6.2
ESS Sizing Statistical Study Results

MCFLs (kN)	**1 Load**	**2 Loads**	**3 Loads**	**4 Loads**
10	505 kWh	1,703 kWh	2,900 kWh	4,098 kWh
20	8.9 kWh	18.1 kWh	68.7 kWh	657 kWh
30	6.7 kWh	18.1 kWh	50.5 kWh	161 kWh
40	4.5 kWh	18.1 kWh	50.5 kWh	135 kWh
50	3.0 kWh	18.1 kWh	50.5 kWh	105 kWh
60	1.4 kWh	18.1 kWh	50.5 kWh	105 kWh
70	1.3 kWh	18.1 kWh	50.5 kWh	105 kWh
80	0.7 kWh	18.1 kWh	50.5 kWh	105 kWh
90	0.7 kWh	18.1 kWh	50.5 kWh	105 kWh
100	0.7 kWh	18.1 kWh	50.5 kWh	105 kWh
MCFLs (kN)	**5 Load**	**6 Loads**	**7 Loads**	**8 Loads**
10	5,295 kWh	6,493 kWh	7,690 kWh	8,888 kWh
20	1,838 kWh	3,025 kWh	4,219 kWh	5,414 kWh
30	311 kWh	745 kWh	1,804 kWh	2,958 kWh
40	286 kWh	508 kWh	1,010 kWh	1,672 kWh
50	239 kWh	455 kWh	936 kWh	1,431 kWh
60	211 kWh	427 kWh	907 kWh	1,403 kWh
70	209 kWh	425 kWh	906 kWh	1,401 kWh
80	209 kWh	425 kWh	906 kWh	1,401 kWh
90	209 kWh	425 kWh	906 kWh	1,401 kWh
100	209 kWh	425 kWh	906 kWh	1,401 kWh

in the 18 kW range, and the low power valleys are lower than 100 W when the wave energy is lean.

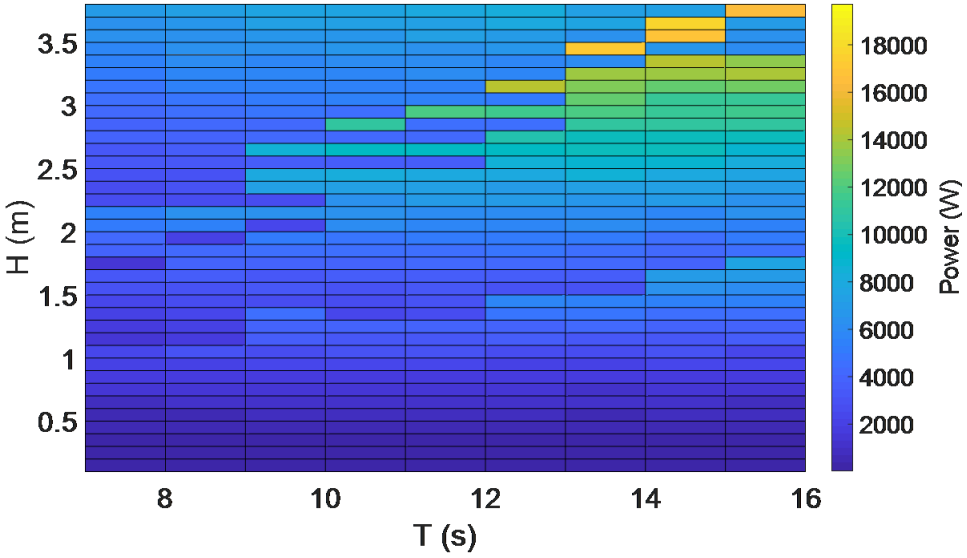

Figure 6.3: Mean power estimation matrix

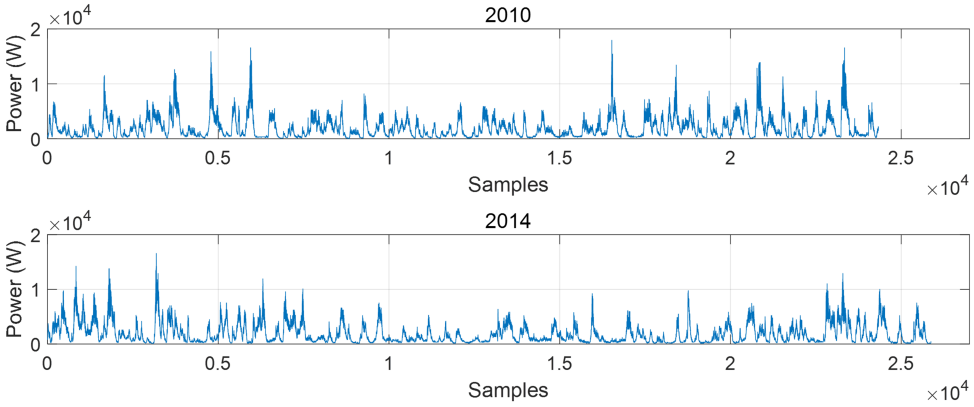

Figure 6.4: Annual mean power time-series of the two selected years

6.5 Bayesian Methodology for Mean Power Time-series Prediction

As the power time-series varies every year due to weather conditions that affect wave height [60], these variations should also be considered when sizing the ESS. In this work we propose propagating the Bayesian approach to the PTO power extraction to better inform the ESS sizing.

Bayesian statistics are particularly interesting due to the fact that it updates the probability of a hypothesis as new information arises. It is based upon the interpretation of different states of believed probability. The general form of Bayes' equation is shown as

$$p(H|D) = \frac{p(D|H)p(H)}{p(D)} \tag{6.1}$$

where the variables D and H are groups of observed variables and unobserved variables respectively. $p(H|D)$ is the posterior distribution, $p(D|H)$ is the likelihood function, $p(H)$ is the prior distribution and $p(D)$ is the marginal distribution of observations on the unobserved variables H. By calculating the unobserved variables through definition of probability distributions' parameters, the probabilistic expression can include all uncertainties that in sampling, measurement and processing. In

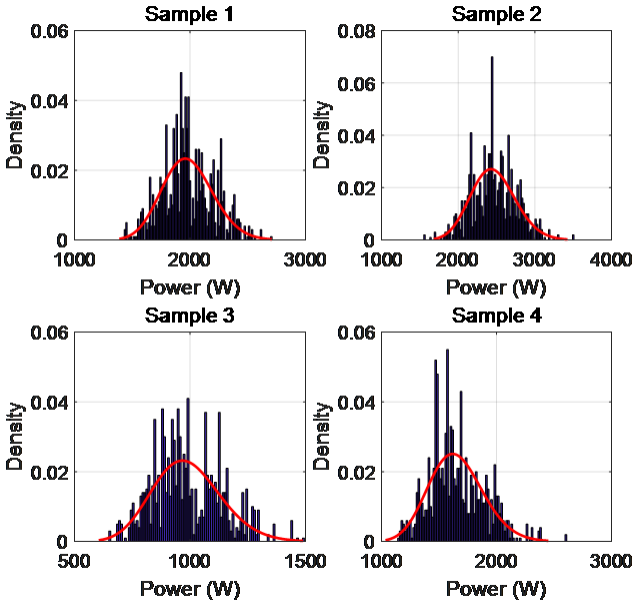

Figure 6.5: Posterior PDF of four random picked samples

this case, gamma distribution is applied to generate the prior distribution for each sample in the time-series. Posterior distribution is estimated based upon (6.2). However, it is not possible to calculate the marginal distribution of observations for all values of unobserved quantities. Therefore, Markov Chain Monte Carlo (MCMC) algorithm is used to calculate the posterior distributions and Metropolis-Hastings method is applied for sampling. The posterior Gamma distribution probability density function (PDF) of four random picked time stamps are shown in Figure 6.5.

Based on the posterior PDF, the annual statistical power out-put time-series, shows in Figure 6.6, is composed by the mean value from the posterior distribution obtained for samples. However, it is lacking extremely high or low power values, which is different from the ground truth examples in the Figure 6.4. Other authors, such as

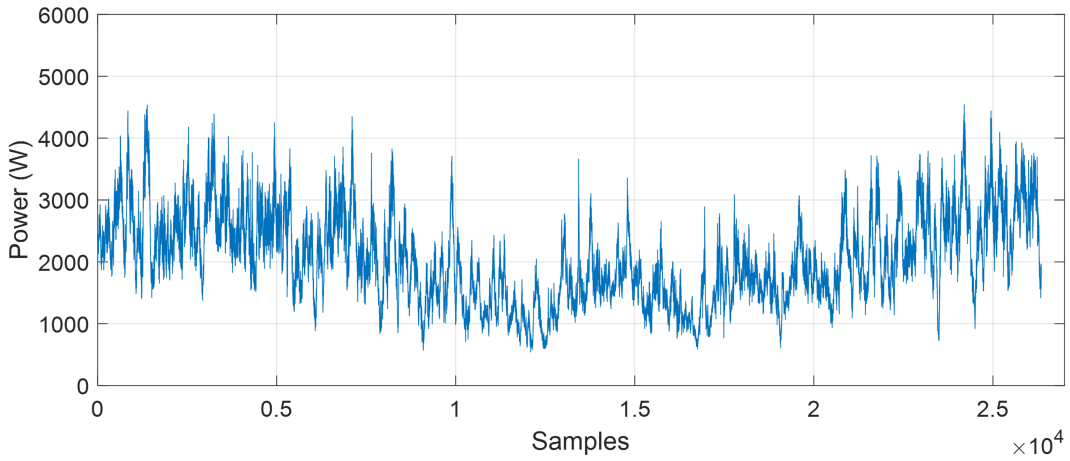

Figure 6.6: Predicted annual mean power time-series

[58, 59], show similar challenges. The power layout in ground truth power time-series varies for different years with high frequency variations that also include high or low power samples that are infrequent. This particular pattern complicates the probability study. The situation can be hypothesized that a frequency-based analysis should be overlapped to the Bayesian statistics to capture both the correct distribution in each sample and the annual maximums and minimums pattern.

6.6 ESS Sizing for Statistical Study

Table 6.3 shows all the required capacities for different ESS design. For the actual ocean data, since 2001 to 2016, the required capacity reaches 790.57 Wh when the annual power is lean. However, in some cases, such as year 2009 and 2016, the ESS is not required at all, due to the active wave motion throughout the whole year.

Table 6.3
ESS Sizing Statistical Study Results

Recorded Years	**ESS Capacity**	**Recorded Years**	**ESS Capacity**
2001	22.08 Wh	2009	0.00 Wh
2002	58.49 Wh	2010	790.6 Wh
2003	47.41 Wh	2011	79.48 Wh
2004	246.2 Wh	2012	22.30 Wh
2005	34.88 Wh	2013	0.00 Wh
2006	22.21 Wh	2014	22.30 Wh
2007	81.35 Wh	2015	91.23 Wh
2008	333.5 Wh	2016	0.00 Wh
Re-built Power		**Re-built Power**	
Mean	0.00 Wh	Mean-4SD	941.0 Wh
Mean-5SD	2880 Wh		

Figure 6.7 shows the Gamma distribution probability density function (PDF) of the required capacities for the observed years. Any required capacity larger than 200 Wh (year 2004, 2008 and 2010) is not showing in the figure since they are rare, but also because the PDF is not able to reflect the actual scenario very well due to the limited quantity of the observed years. Based upon Figure 6.7, the required capacity is in the range of $0 - 100\ Wh$ in most cases.

Based on Chebyschev's Theorem, which is shown as:

$$f = 1 - \frac{1}{k^2} \tag{6.2}$$

where f is a fraction of the data within k of the mean for any data set, the k is number of the considered standard deviation (SD). According to the Eq. 6.6, 88.89 % of all the power magnitude probability is included when considering 3 SD of the mean.

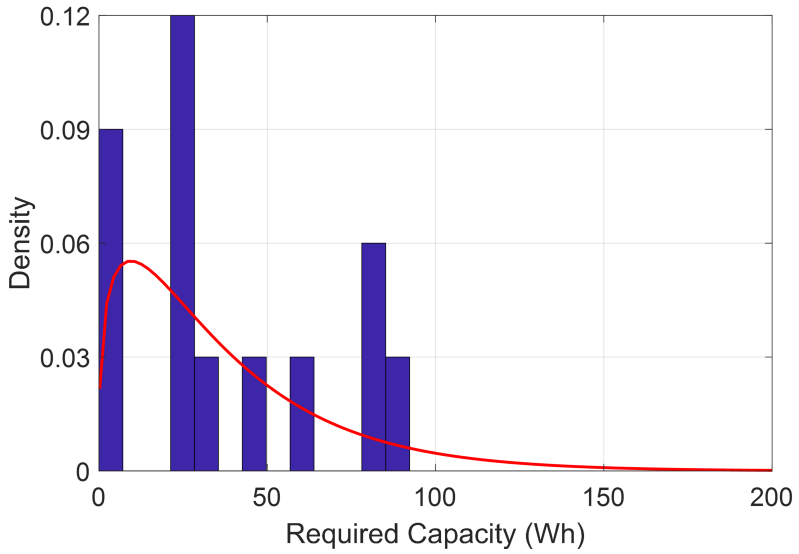

Figure 6.7: ESS Sizing Statistical Study Gamma Distribution

Similarly, 93.75 % and 96 % of the probability are included when considering $4SD$ and $5SD$ respectively. For the predicted power map, if only mean power of each time stamp is considered, like the power map in Figure 6.5, according to Figure 6.3, the required capacity is 0, since the mean values of the predicted power is much higher than the required 120 W. However, the mean power from Bayesian method is not able to represent the high power bursts or extremely low power valleys. According to the Chebyschev's Theorem, starting with 90 % of all the power magnitude probability ($4SD$, 93.75 %), the required capacity is 941 Wh in Figure 6.3, when the power map is composed by ($mean$–$4SD$) power magnitude for each time stamp. The map is able to represent the statistically worst scenario in the year when considering $4SD$ of the mean, since the power magnitude of each time stamp is assumed to be statistically the lowest. When considering $5SD$ of the mean, the required capacity is increased to $2,880$ Wh, which is much higher than the actual required capacities for the observed

years, since similarly, the power magnitude for each time stamp is assumed to be statistically the lowest, ($mean$–$5SD$). The assumed lowest power map of considering $5SD$ of the mean is shown in Figure 6.5. To obtain more reliable sized ESS, the predicted power map with considering higher SD level can be generated based on the same method. However, the required capacity will also be increased significantly.

6.7 Conclusions

The ESS sizing progress with considering statistical analysis for WEC system supporting ocean sensing application is presented in this chapter. Downsizing the PTO scale and supporting multiple loads are also discussed in this chapter to design the ESS in the most efficient way. To increase the ESS design reliability, Bayesian method is applied to summarize the generated power Gamma distribution for each time stamp based on the observed historical ocean data. The predicted power map is generated by the means and SDs of the time stamps in the whole year. Based upon Chebyschev's Theorem, in order to cover most cases in the future functioning, required capacities of ESS for 4SD and 5SD of mean consideration are estimated. To guarantee the ESS is able to fulfill the selected consideration, the correspondingly assumed lowest power map is used to estimate the required capacities. The required capacity is increased significantly with the statistical tolerance consideration. More reliable design can be obtained by increasing the level of considered SDs. The PTO static modeling could

be used for fast processing the large ground-truth data base, but it is not detailed enough for PTO power loss model studying and design improvement. So the WEC PTO dynamic model will be integrate on the buoy hydrodynamic model in the next chapter.

Chapter 7

Actual PTO Impacts on Wave Energy Extraction

7.1 Introduction

In former chapters, electrical PTO static model for direct-drive WEC has been introduced. The PTO static model is a simplified model, which can be used to determine the dominant parameters for the WEC PTO and ESS design. However, it is not enough to study the WEC electrical drive actual behaviors. Especially for WEC control performance assessment, more detailed PTO dynamic behaviors are demanded. In this chapter, electrical PTO dynamic model will be applied on the

buoy dynamic model to study the actual electrical outputs of the direct drive WEC system. Although numerous buoy control schemes have been presented in the literature [10, 23, 24], few of the electrical power take-off (PTO) impacts have been considered in these control algorithms and are only proposed for ideal conditions.

This chapter presents the results of the bias between the ideal PTO conditions and the limited PTO (stroke and force) conditions. In this chapter, the WEC device adopts the small scaled direct-drive WEC device as shown in the Figure. 2.1. The LEM stroke has been limited to 3 m.The PTO power loss model and operation efficiency are studied and applied in this chapter as well. The results highlight the necessaries and the demands of relating the ideal buoy control schemes design and the feasibility of the actual PTO applications. Model predictive control, shape-based control, singular arc control, and proportional-derivative control are applied and their performance assessments are obtained as well.

The electrical PTO components include a LEM equivalent circuit model, an ideal inverter model, a DC circuit model and an ideal constant voltage source, as in Section 3.3, 3.4. The electrical drive is controlled to fulfill the buoy control force requirements with respect to the control algorithms. Ideal (unlimited stroke and current) PTOs and limited PTOs will be both discussed and implemented. The electrical outputs of all the applied buoy control algorithms will be obtained and evaluated. Furthermore, by studying the electrical PTO power losses, the optimal operation

current limitations for the applied buoy control algorithms are determined. In the end, a more complex electrical machine efficiency map and an actual inverter efficiency map will be implemented in the electrical drive model, and the energy extraction results will also be presented. Meanwhile, possible solutions for improving the electrical PTO operation efficiency will be discussed.

7.2 Dynamic Model Coupling and PTO Behaviors from Shape-based Control

According to the model configuration that has been introduced in the previous sections, the buoy dynamic model and the electrical drive (LEM, inverter and DC circuit) dynamic model can be coupled by applying the Eq. (3.14), (3.15). The electrical drive outputs of the SB control, as an example, are shown in this section to validate the electrical drive behaviors. All the following results have all been simulated for 300 s. The irregular wave which has a significant height of 1 m and a peak period of 8 s is applied as input in this chapter.

The reference control force signal and the actual control force are shown in Figure 7.1. The reference control force signal has been fulfilled by the LEM. In Figure 7.1, when zoomed in, it is clear that the reference control force signal has rapid changes and spikes, these control force spikes are casued by the SB control prediction horizon

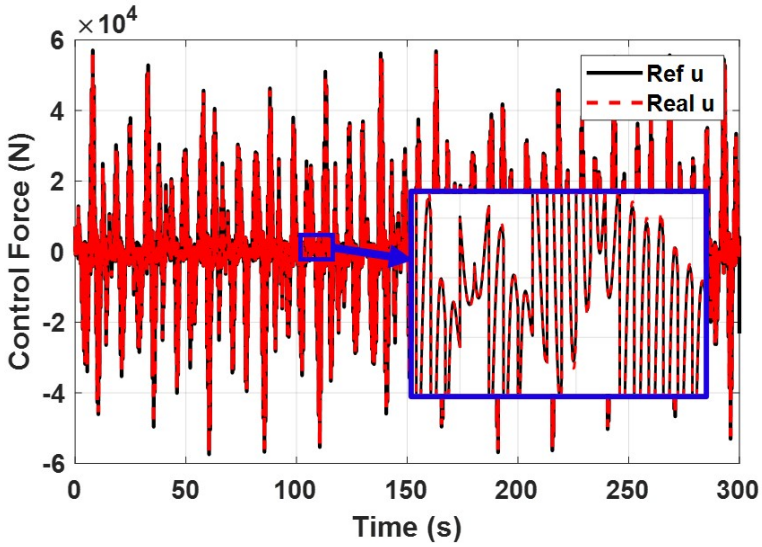

Figure 7.1: Shape-based reference and actual control force

(Section 4.3), but they all can be followed well by the LEM.

The LEM terminal voltage v_{dq} and current i_{dq} are shown in Figure 7.2. In Figure 7.2, the v_{dq} magnitude can be controlled by the λ in Eq. (3.18). The i_d cannot be controlled perfectly to 0 all the time, but it is small enough to be neglected. The i_q reaches above 500 A due to the significant control force requirements. In this section, there is no PTO constraints being considered (e.g., unlimited buoy displacement and circuit current), so that the i_q current can be increased as much as necessary to fulfill the control force requirements.

The DC circuit current i_{dc} is shown in Figure 7.3. The current and power have been defined with positive values flowing to the voltage source V_s . Therefore, when $i_{dc} > 0$ the LEM is operated as a generator to extract wave energy.

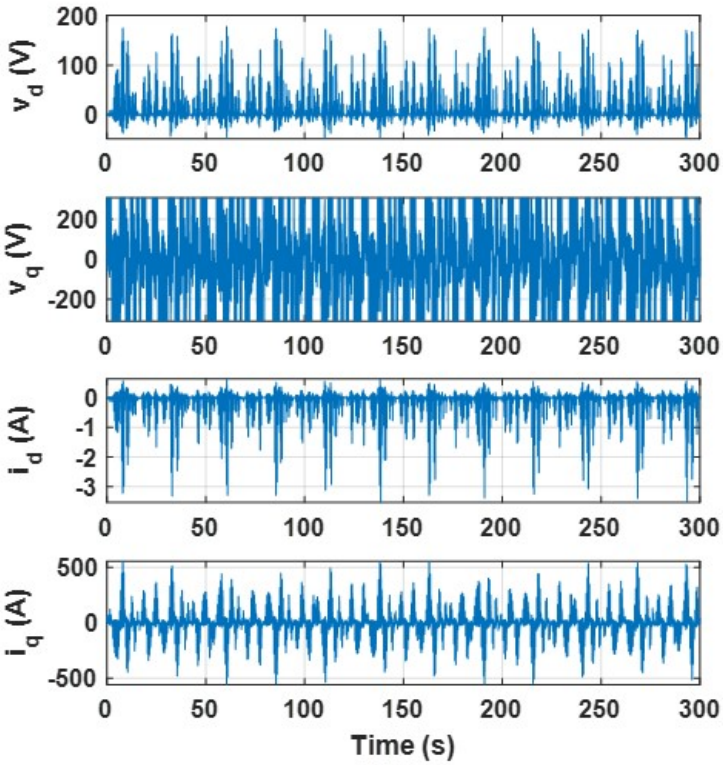

Figure 7.2: Shape-based control AC outputs in dq frame

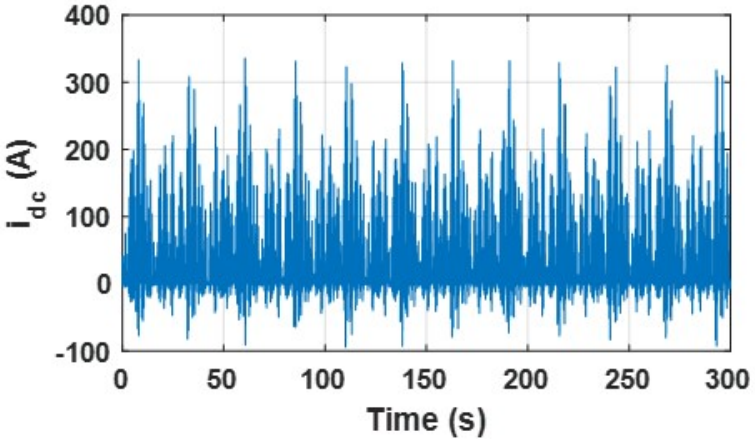

Figure 7.3: Shape-based control DC current output

7.3 Energy Extraction Results from Different Controls and Unlimited PTO

7.3.1 Results from Unconstrained Control and Unlimited PTO

There are no buoy displacement or control force constraints being considered in the SA and PD control. The two controls will maximize the buoy oscillation to extract optimal wave power, resulting in the excessive control force requirements. The SA and PD ideal results and the actual electrical outputs with unlimited PTO are shown in the Figure 7.4. The ideal signal in the figure is based upon the buoy dynamic model calculation with ideal PTO assumptions. It is the mechanical energy on the buoy

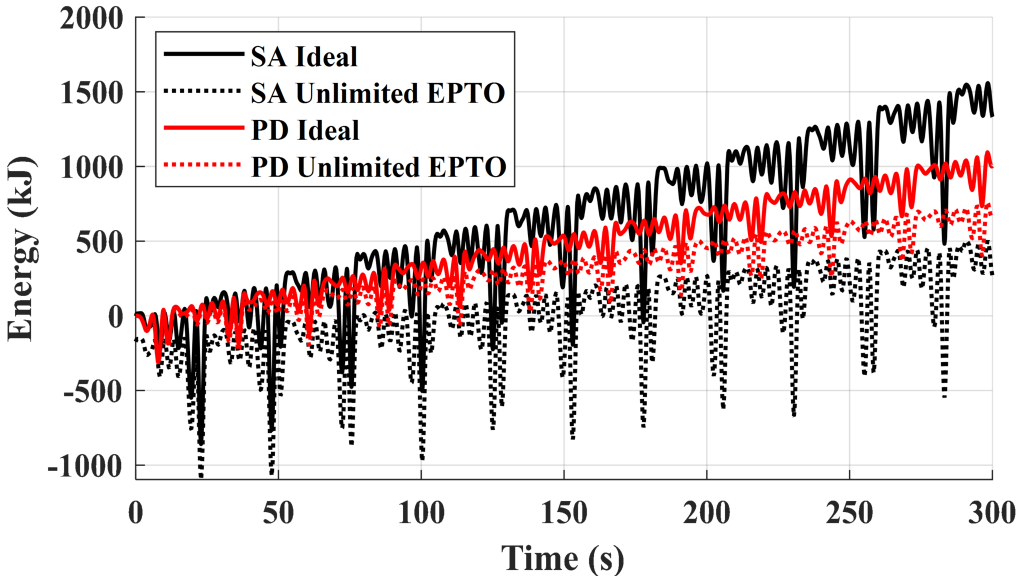

Figure 7.4: PD and SA theoretical and electrical energy outputs with unlimited PTO

side, which is the integration of the buoy mechanical power. The buoy mechanical power is calculated by $P_{mech} = u\dot{z}$. The electrical (EPTO) energy output is the actual electrical PTO output based upon Eq. (3.19). The ideal energy outputs from SA is higher than the one from PD. However, the actual electrical energy outputs with unlimited PTO from SA is lower, which means the PTO power extracting efficiency of the PD control is higher than the SA control.

The reference control force signals and the actual control force of both the SA and PD are shown in the Figure 7.5. According to the Figure 7.5, the reference control force signal is tracked by the unlimited electrical PTO, which proves that the main reason that causes the bias between the ideal and actual energy outputs is the added PTO losses, instead of the PTO control force tracking performance. The results

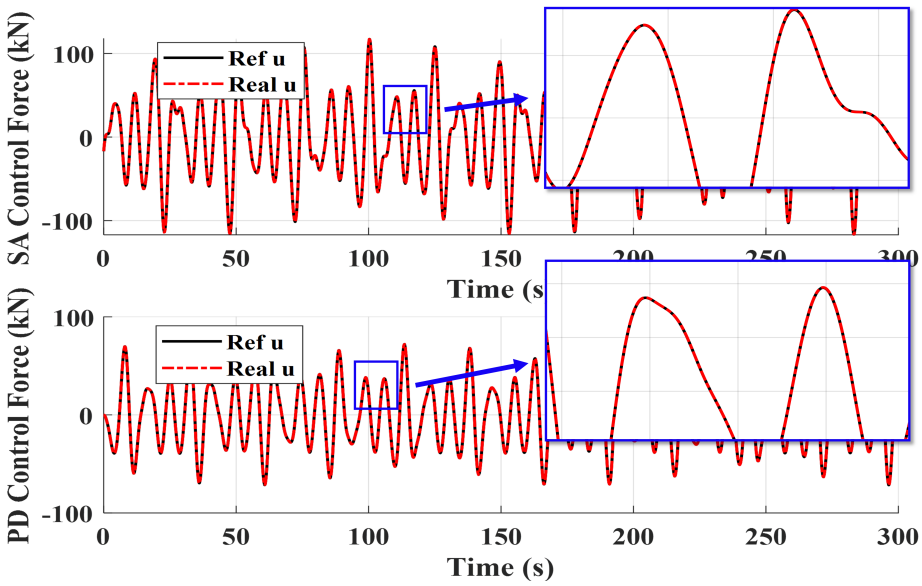

Figure 7.5: PD and SA reference and real control force with unlimited PTO

from the unconstrained model-based controls (e.g., PD and SA) indicate that the proposed promising control performance in ideal conditions does not lead to the good wave-to-wire performance due to the PTO constraints and losses have been neglected.

7.3.2 Results from Constrained Control and Unlimited PTO

The WEC buoy displacement saturation has been considered in the MPC and SB control algorithms. Due to the LEM stroke limit, the maximum trough to crest of the buoy oscillation has been saturated to 3 m. As with the previous section, the ideal and actual electrical energy outputs of the MPC and SB control are shown in the Figure 7.6, and the reference and actual control forces are shown in the Figure 7.7.

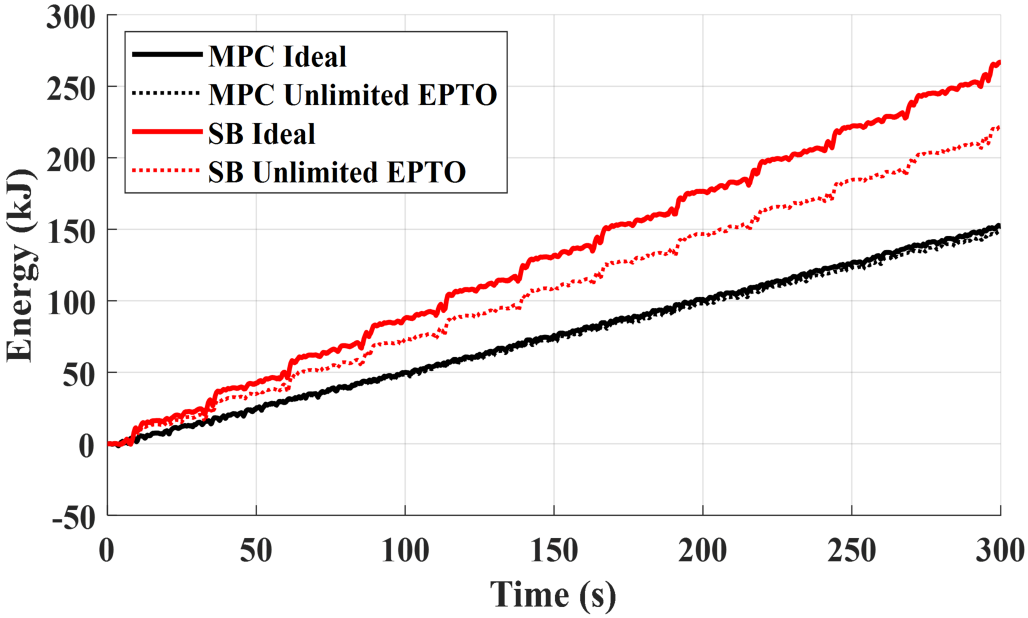

Figure 7.6: MPC and SB theoretical and electrical energy outputs with unlimited PTO

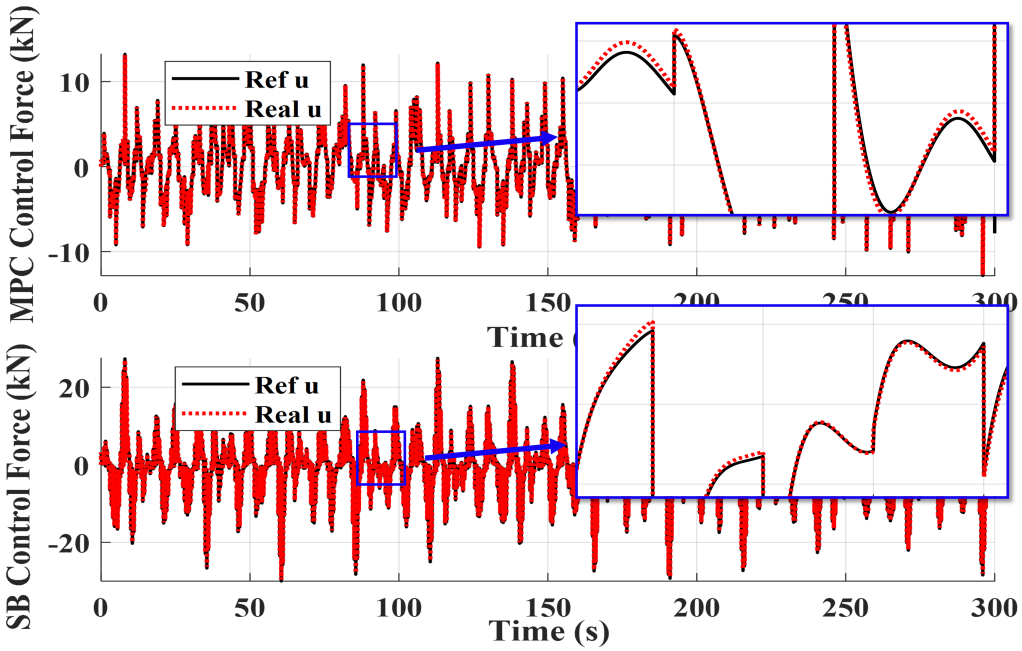

Figure 7.7: MPC and SB reference and real energy outputs with unlimited PTO

Based upon the energy extraction results in the Figure 7.6, the MPC and SB control with unlimited PTO extract much less energy comparing to the SA and PD control algorithms due to the buoy displacement saturation. The SB control can extract more energy but with larger bias between the ideal output and the actual output. According to the control forces shown in the Figure 7.7, the reference control force signals for MPC and SB can be tracked by the electrical PTO. However, when zoomed in (blue blocks), the reference signals cannot be tracked as well as they did for SA and PD due to the signal spikes which are caused by the prediction horizon. The slight untracking could also cause the output bias besides the added electrical PTO losses.

7.4 Electrical PTO Power Loss and PTO Current Limitation

According to the results in the previous section, unconstrained PD and SA demands excessive control force (up to 117 kW in SA) to achieve the maximum buoy oscillation (about 30 m trough to crest displacement in SA). The excessive required control force will end up with large current flow in the electrical drive and result in significant electrical power losses. The losses still has a significant impact on the actual energy output even when the PTO can fulfill the control force requirements.

Unlike passive control algorithms, the LEM in this paper need to extract active power and also provide reactive power. The electrical power loss in this scenario is expressed as

$$P_{loss} = \sqrt{\frac{3}{2}} R_s (i_d^2 + i_q^2) + R_{line} i_{dc}^2 \tag{7.1}$$

where P_{loss} is the total power loss in the electrical drive, $\sqrt{\frac{3}{2}}$ is a scale factor when calculate the power in dq frame. Due to no other loss considered, the only loss in the electrical drive is the loss caused by the circuit resistances.

According to the Eq. (7.1), the efficiencies of the electrical drive extracting and providing power is

$$\begin{aligned} \eta_{act} &= \frac{\mid P_{mech} \mid - P_{loss}}{\mid P_{mech} \mid} \\ \eta_{react} &= \frac{\mid P_{mech} \mid}{\mid P_{mech} \mid + P_{loss}} \end{aligned} \tag{7.2}$$

where η_{act} and η_{react} are the efficiencies when the electrical drive extracting and providing power respectively, P_{mech} is the required mechanical power for the buoy control. The absolute value is applied to eliminate the power flow directions.

Based upon Eq. (7.2), the overall energy extracting efficiency of the electrical PTO

in the 300 s time frame is

$$\eta_{all} = \frac{\sum_i^N (|P_{e\_m,i}| - P_{e\_l,i}) - \sum_j^M (|P_{p\_m,j}| + P_{p\_l,j})}{\sum_i^N |P_{e\_m,i}| - \sum_j^M |P_{p\_m,j}|} \tag{7.3}$$

where η_{all} is the overall extracting efficiency, N is the total number of the time steps when the WEC is extracting active power in the time frame, $P_{e\_m,i}$ and $P_{e\_l,i}$ are accordingly the buoy extracted mechanical power and PTO power loss at time i. Similarly, M is the total number of the time steps when the WEC is providing reactive power in the time frame, $P_{p\_m,j}$ and $P_{p\_l,j}$ are accordingly the reactive mechanical power and PTO power loss at time j.

According to the Eq. (7.3), even when the electrical drive has a high efficiency, the overall energy extracting efficiency can be low. To further prove that, the efficiency of all the electrical PTO operation points in SB control, as an example, is shown in Figure 7.8. Based upon the efficiency map, for most operation points (more than 95 %) in SB have a high efficiency (higher than 95 %). However, the electrical energy output, according to the Figure 7.6, is only about 80 % of the ideal value. To improve the overall energy extraction efficiency, the electrical PTO operation efficiency can be increased more by limiting the provided control force. Based upon the Figure 7.8, the operation points within the black square area (where the control force magnitude is smaller than 10 kN) can have even higher efficiencies. Based upon the Eq. (3.15), limiting the i_q current is a straightforward way to limit the electrical PTO control

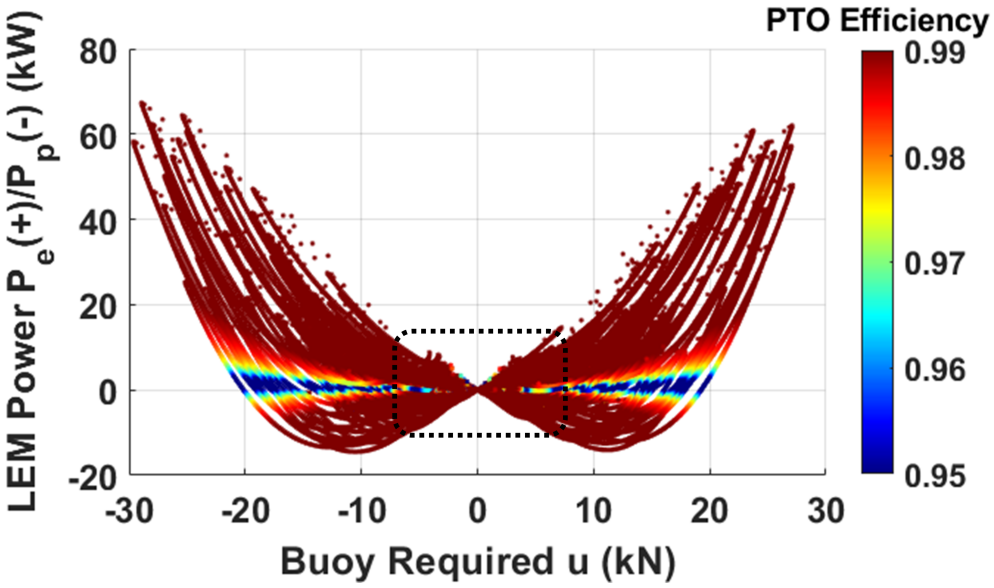

Figure 7.8: Electrical PTO efficiency of all operation points in SB

force.

7.5 Limited Electrical PTO Impacts on Control Algorithms

It has been assumed that there is no mechanical power loss when the LEM translator reaches the stroke limit and the buoy oscillation is always continuous. According to this, the i_q current limitations of a sweep from 50 A to 200 A with a 50 A increment have been applied to the simulations. The energy extraction results of the 300 s frame by SA, PD, MPC and SB controls are shown in the Figure 7.9.

In the Figure 7.9, the positive energy is the extracted energy, and the negative energy

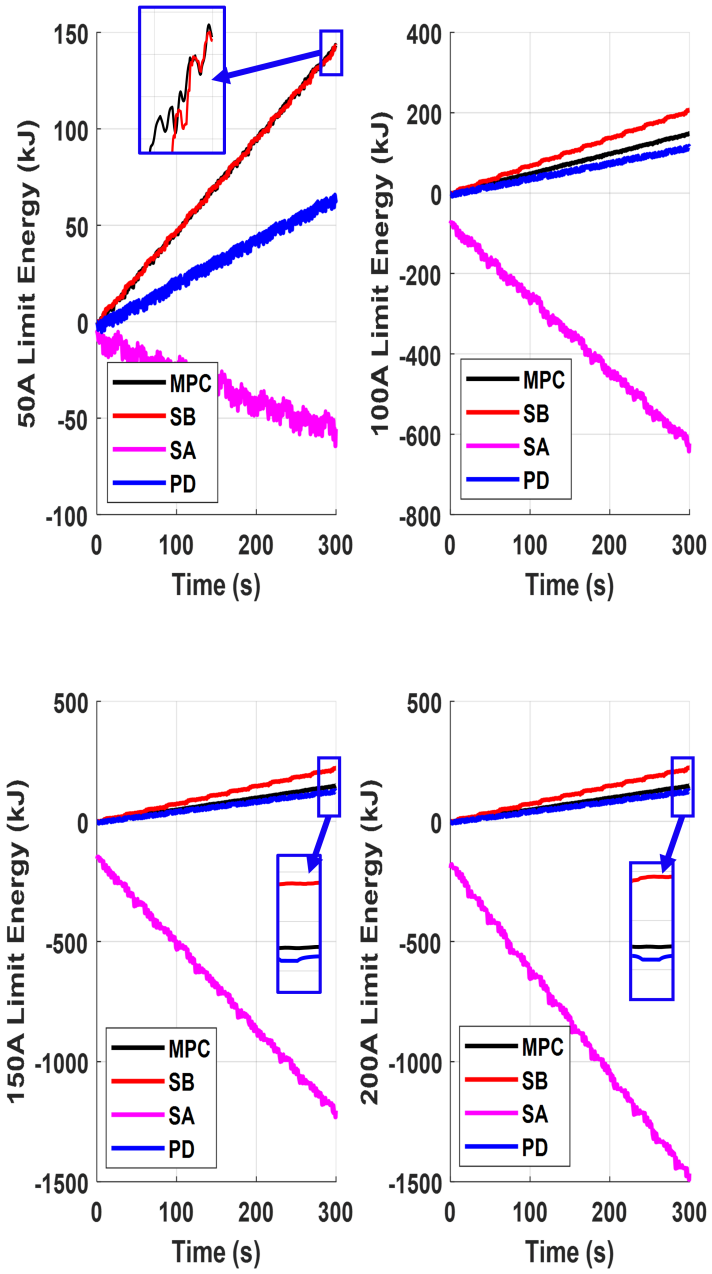

Figure 7.9: Energy extraction results with different i_q current limitations

is the consumed energy for the buoy control. With the selected i_q current limitations, the SA control cannot extract any energy but provide energy for the buoy control due to the limited LEM stroke. The SA control can achieve the maximum extracted

energy in ideal conditions, but the feed-forward control signals will end up with no extracted energy while limited PTO applied. This situation cannot happen physically since the excessive losses would likely damage the device. The PD control, as another unconstrained control, has a feedback control loop, so that it can actually extracted energy while the stroke limit is applied. The MPC and SB control are both constrained optimization control algorithms. SB control can always extract the maximum energy for all the applied current limits. While the current limits are high (150 A, 200 A), the MPC can extract slightly higher energy than the PD. On the other hand, if the current limits are low (50 A), the MPC and SB controls can have similar results.

To further evaluate the energy extraction performances for the same control but with various current limits, the energy extraction mean powers of the time frame are shown in the Figure 7.10. The MPC control requires the minimum level of the control force comparing to the other three control algorithms, the maximum i_q in MPC control is close to 100 A, so that the mean power keeps constant while the current limits is higher than 100 A. Similarly, the PD control requires significantly decreased i_q current (< 150 A) while the stroke is limited. The SA control can extract energy when the current limit is extremely low (25 A), the mean power is much lower comparing to the other three algorithms. The SB control can achieve the highest mean power when the current limit is 200 A, and it is even higher than the unlimited current case. This scenario corresponds to the PTO operation points efficiency map in the

Figure 7.8. Although the limited current will decrease the extracted power, it will limit the electrical power losses as well. The optimal extracting/loss trade-off can be found to achieve the maximum energy extraction.

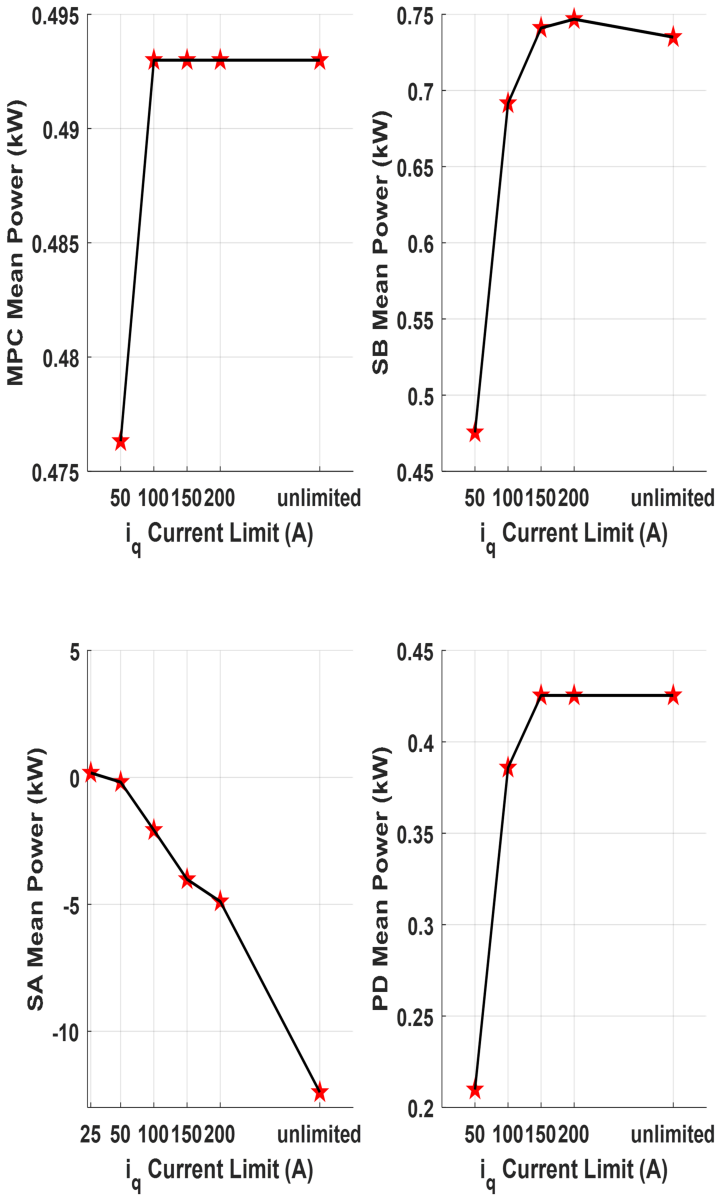

Figure 7.10: Energy extraction mean power results with different i_q current limitations

7.6 Electrical Machine and Inverter Efficiency Map Implementation

In this section, a general permanent magnet synchronous electrical machine efficiency map has been applied. The implemented inverter efficiency map is based upon the actual product [61]. The model configuration is shown in the Figure 7.11. In the Figure 7.11, the η_{em} is the LEM operation efficiency, the η_{inv} is the inverter efficiency, both of them are determined by the implemented efficiency maps $\eta_{em}(\dot{x}, u)$ and $\eta_{inv}(V_{dc}, i_{dc})$. The product of the η_{em} and the η_{inv} is the overall efficiency ($\eta_{overall}$) of the LEM and the inverter. According to the $\eta_{overall}$, the power loss is calculated based upon the power inputs to the electrical drive. The value of the equivalent resistance R_{eq} is obtained by applying the same amount of power loss on the controlled resistors in the circuit model, so that the LEM and inverter efficiency maps is implemented by manipulating the controlled resistors.

The SB control has been selected as an example due to the best energy extraction performance according to the results in the previous Section 7.5. The overall efficiency map ($\eta_{overall}$) with all the SB control electrical PTO operation points are shown in the Figure 7.12. In the Figure 7.12, the red dots are the electrical PTO operation points. The highlighted black curves have separated the map into low efficiency area

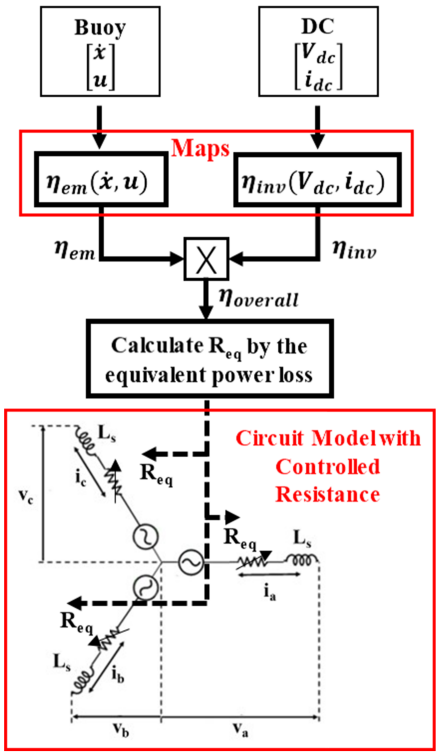

Figure 7.11: Efficiency map implementation configuration

(below 80 %), medium efficiency area (80 % to 90 %) and high efficiency area (above 90 %). 23.15 % of the operation points are in the low efficiency area due to the low buoy velocity and high required control force. 55.10 % of the operation points locate in the medium efficiency area and only 21.75 % of the operation points are in the high efficiency area. Few of the operation points (0.17 %) can have efficiencies higher than 93 %. Comparing to the electrical PTO efficiency in the Figure 7.8, where most of the operation points can achieve higher efficiencies than 95 %, the electrical PTO operation efficiency has decreased significantly as a result of implementing efficiency map models.

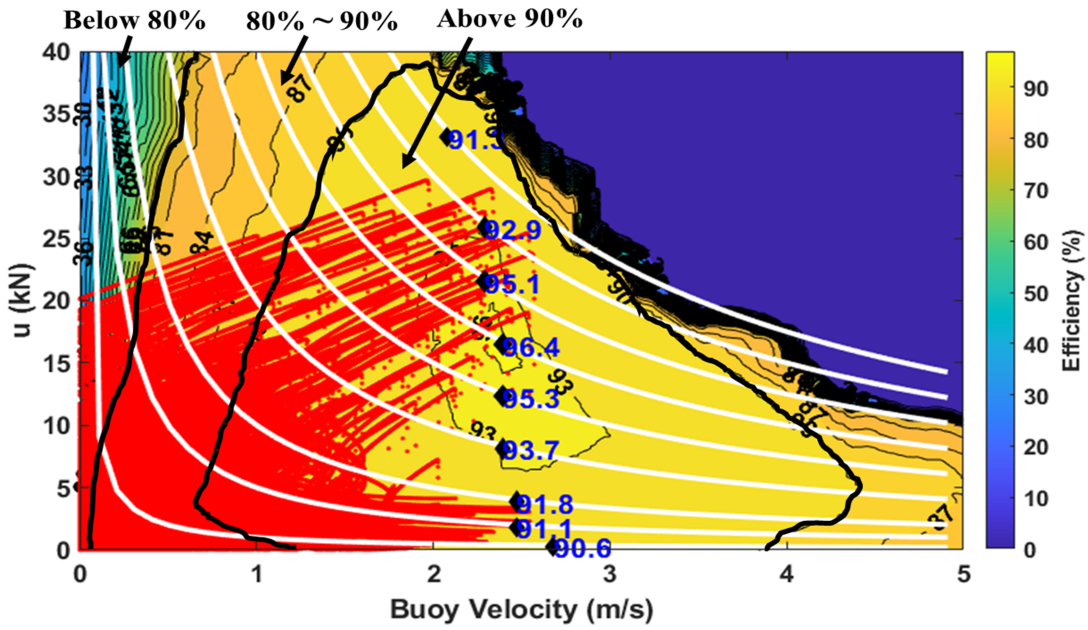

Figure 7.12: Efficiency map and operation points

The energy extraction results by the SB control in different conditions are shown in the Figure 7.13. The ideal signal (mechanical energy) is calculated from the buoy dynamic model by integrating the product of the buoy velocity and required control force (as in the previous sections). The result with unlimited PTO is lower than the one with 200 A i_q current limitation due to the electrical power losses. The blue curve is the extracted energy while considering the actual efficiency maps. Comparing to the ideal signal, the amount of the extracted energy with actual efficiency maps only takes about 60 % of the ideal result.

One of the possible solutions for increasing the electrical PTO operation efficiency is re-design the electrical PTO to obtain a best fitting PTO for the selected wave conditions and the selected WEC design. This solution is not robust for all the wave

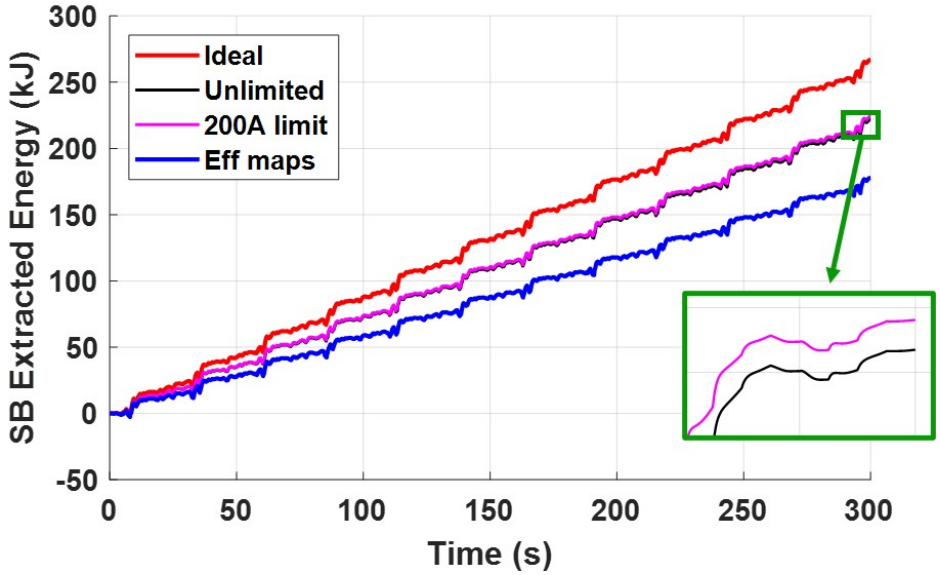

Figure 7.13: SB energy extraction comparison in different conditions

conditions at all, and it will not be discussed in this paper. Besides re-designing the electrical PTO, an added gear system, such as a continuously variable transmission system, can be applied to connect the buoy and the LEM translator. By controlling the gear ratios, the added gear system can manipulate the electrical PTO operation points and allow the electrical PTO to seek the most efficient operation points along the required power lines without compromising the control force requirements. The white color curves in the Figure 7.12 are the power lines from 0.1 kW to 70 kW (the increments are not fixed). The black squares on the power lines show the highest operation efficiencies along the power line for the PTO. Implementing an extra gear system could help the PTO to achieve a much higher overall energy extraction efficiency from the results shown in the Figure 7.12. However, the added gear transmission will introduce a new power loss model into the WEC system, and the actual gear system limits need to be considered as well. The evaluation of the energy

extraction performance needs to be included in the future study.

The Table 8.1 shown in the end includes the wave energy extraction performance of the selected control algorithms in various conditions (ideal and limited PTO). The i_q current limits shown in the table are the optimal limits or ∞ (unlimited current) according to the results in the previous sections. The maximum required control force (u_{max}), the maximum buoy displacement (z_{max}-z_{min}) and the extraction mean power (P_{mean}) are given in Table 8.1.

Table 7.1
Extraction performance comparison

Symbol	**Value**	**Symbol**	**Value**
SA ideal		PTO (3 m Stroke, 25 A)	
u_{max}	117 kN	u_{max}	2.8 kN
z_{max}-z_{min}	32 m	z_{max}-z_{min}	2.8 m
P_{mean}	4.5 kW	P_{mean}	0.2 kW
PD ideal		PTO (3 m Stroke, ∞)	
u_{max}	72 kN	u_{max}	11 kN
z_{max}-z_{min}	19 m	z_{max}-z_{min}	3 m
P_{mean}	3.3 kW	P_{mean}	0.4 kW
MPC ideal		PTO (3 m Stroke, ∞)	
u_{max}	13 kN	u_{max}	5.3 kN
z_{max}-z_{min}	2.6 m	z_{max}-z_{min}	2.5 m
P_{mean}	0.5 kW	P_{mean}	0.4 kW
SB ideal		PTO (3 m Stroke, 200 A)	
u_{max}	30 kN	u_{max}	21 kN
z_{max}-z_{min}	2.9 m	z_{max}-z_{min}	2.8 m
P_{mean}	0.7 kW	P_{mean}	0.8 kW
SB with η_{maps}			
u_{max}	30 kN		
z_{max}-z_{min}	2.9 m		
P_{mean}	0.6 kW		

7.7 Conclusion

In this chapter, the WEC electrical PTO model is implemented with several different buoy control algorithms (PD, SA, SB and MPC) to study the bias between the ideal extracted energy and the actual extracted energy. Electrical power loss mechanisms were introduced into the WEC, resulting in a low overall efficiency. The electrical PTO power loss has great impacts on the unconstrained control algorithms (PD and SA) from the results in the Section 7.3.1, due to the excessive current flow in the electrical drive. The i_q current limitation strategy is discussed in the Section 7.4 to improve the electrical PTO operation efficiency by studying the power loss model and the electrical PTO operation points. The limited PTO (LEM limited stroke and limited i_q current) is implemented to the controls in the Section 7.5. The SA control can only extract energy with extremely small i_q current limitation (25 A) due to the limited stroke. The PD control can extract energy with higher i_q current limitation since it is a feedback loop control. The limited LEM stoke has no effects on the constrained controls (MPC and SB) since the buoy displacement saturation has been considered in the control algorithm. The electrical PTO with limited i_q current can extract even more energy due to the higher PTO operation efficiency, such as SB control with 200 A i_q current limitation. Actual hardware efficiency maps are implemented to the LEM circuit model by controlling a variable resistors in Section 7.6. The electrical PTO operation points from SB control and the energy

extraction results comparison are shown in the section as well. One of the possible solutions for increasing the PTO operation efficiency is to implement an extra gear transmission system to manipulate the PTO operation points. However, more factors need to be included in the future study to evaluate the efforts. The results in table (Table 8.1) show the actual PTO losses will have great impacts on the WEC and buoy control designs, and the actual optimal results are obtained only when all the factors are considered. Another of the possible solutions for increasing the electrical PTO operation efficiency is re-design the electrical PTO to obtain a best fitting PTO for the selected wave conditions and the selected WEC design. However, this solution is not robust for all the wave conditions at all. The most robust solution to improve the wave energy extraction performance is that applying the control design from a global point of view of the whole wave-to-wire dynamics, such as designing the optimization control for the wave-to-wire dynamic model. The challenges would be the excessive computational cost, since the wave-to-wire model is highly complex and non-linear. Meanwhile, another possible solution could be the machine reinforcement learning, which will be introduced in the last chapter.

Chapter 8

Reinforcement Learning Solution

8.1 Introduction

In the former chapters, the model-based controls, which are designed based upon buoy hydrodynamics, have been assessed on the real electrical PTO models. The results turn out that the actual PTO constraints and loss will have great impacts on the control performance. The bias between the control proposed ideal (mechanical) output and the actual PTO (electrical) output is significant. The selected model-based controls cannot achieve the optimal wave energy extraction in the wave-to-wire modeling, since they are all design from a local point of view (based upon buoy hydrodynamic only). How to design a control for WEC wave-to-wire model from a

global point of view is a challenge. As discussed in the former chapters, a wave-to-wire optimization control could be a solution. However, the computational cost of the wave-to-wire optimization would be significant due to the model complexities. On the other hand, the machine reinforcement learning could be another key to design the control from a global view, and it will be discussed in this chapter.

Recently, the machine learning techniques experienced explosive growth and are shown promising performance in conducting complex tasks [29, 30, 31, 32]. A function approximator is typically implemented (e.g., the neural network) to approximate the complex dynamics of the environment, which makes the machine learning technique data-driven or even model-free. In the context of the previous-mentioned challenge (cannot isolate control design from the wave-to-wire model), it is therefore highly desired to introduce the machine learning techniques to wave energy conversion. The supervised learning is typically applied to predict the wave information (e.g., wave forces [62], wave elevation [63]), approximate complex hydrodynamics [64, 65, 66, 67], and complex wave mechanics [68, 69, 70]. However, the major challenge of applying the supervised learning techniques in a complex WEC system is that there is no known optimality. In contrary to supervised learning, the reinforcement learning (RL) algorithm is more appropriate to be applied to wave energy conversion problems considering the RL agent will automatically identify the optimality based on direct interaction with the environment. While the investigation of using RL to maximize wave power production is relatively underdeveloped in the literature. Only a few

studies [71, 72, 73] are conducted, in which a fully developed PTO dynamics are not considered. Unlike the existing method (assume a linear proportional-derivative (PD) control law), a time-varying PD control law is implemented in this chapter since the proposed wave-to-wire model is highly nonlinear which may not be sufficiently controlled by using a linear PD law. The optimal time variation of PD gains will be identified by the DQN agent through direct interaction with the nonlinear environment. Finally, the actual electricity generation will be collected as the reward of the agent such that guarantees the agent will optimize the system performance from a global point of view (wave-to-wire dynamics, power losses, motion constraints, etc.).

The WEC device adopted in this paper is the same as the former chapters (Figure 2.1), which has a radius of 0.5 m, a draft of 0.5 m, and a rigid body mass of 399.15 kg. The LEM translator is rigidly attached to the bottom of the device, and the stator is connected to a lower-body such that a relative motion, with a maximum stroke of 3 m, is created for wave energy extraction.

The wave-to-wire model in this chapter is composed of two dynamics: the hydrodynamics and the PTO dynamics, which have been introduced in detail in the Section 3.2 -3.4. Moreover, the dynamics of all the subsystems are fully coupled to complete the simulation framework.

Giving that there are many physical constraints that cannot be violated to avoid the failure of the device in real-time operation, it is therefore critical to take the physical

limitations into consideration in designing the control. In this study, the constraints on the displacement of the device (due to the maximum stroke of LEM) and the current in the circuit (due to the capacity of the LEM) are implemented. In which, the constraint on the displacement is implemented in the fashion of modifying the desired control signal

$$\begin{aligned} F_{PTO,ref} &= -K_{p,c} x_{1,max} \text{sign}(x_1) \quad \text{If } |x_1| > x_{1,max} \\ &= Eq.\ (8.6) \qquad \text{Otherwise} \end{aligned} \tag{8.1}$$

where $x_{1,max}$ represents the maximum relative displacement between two bodies. One can clearly tell from this equation that when the motion of the device violates the displacement constraint, the control will focus on regulating the displacement in the constraint instead of concerning the optimality. Furthermore, the current constraint is also considered in calculating the reference current signal

$$\begin{aligned} i_{q,ref} &= \text{sign}(i_{q,ref}) i_{max} \quad \text{If } |i_{q,ref}| > i_{max} \\ &= Eq.\ (3.15) \qquad \text{Otherwise} \end{aligned} \tag{8.2}$$

In this equation, i_{max} is the maximum current of the LEM. Finally, the generated electricity (P_e) can be computed as

$$P_e = \sqrt{\frac{3}{2}}(v_d i_d + v_q i_q). \tag{8.3}$$

8.2 Deep Reinforcement Learning Methodology

Unlike traditional model-based controls, the RL technique does not require explicit knowledge of the system dynamics but instead optimize the system performance (in terms of defined rewards) by direct interaction with the environment. This model-free characteristic makes it well suited to be applied to complex systems. Considering the proposed system includes complex dynamics (modeled from wave to wire), it is very cumbersome or nearly impossible to derive a model-based control. Therefore, it is desired to apply the RL techniques. As far as the learning algorithm is considered, the DQN is applied in this study. The DQN is extended from the widely applied Q-learning technique, which leverages the advantages of deep learning (e.g., is able to learn more complex dynamics, more adaptive). This algorithm is first proposed in reference [29] which shows a successful performance in playing Atari. Unlike traditional Q-learning, there are two Deep Neural Networks (DNN) (namely θ and θ^{-}, which are the weights of the DNNs) are applied to isolate the target generation from the Q-learning update to improve the stability. In which, the target y can be expressed as

$$y = r + \gamma \max_{a'} Q(s', a'; \theta_i^{-}) \tag{8.4}$$

where r is the reward collected from the environment and γ is the future reward discount. Moreover, the s' is the states at the next time instant and a' is the control action that maximizes the target network ($Q(s', a'; \theta_i^-)$). The losses between the target network (θ^-) and the Q network (θ) will be minimized with respect to the weights of the DNNs by using

$$\nabla_{\theta_i} L(\theta_i) = E_{s,a,r,s'}[(y - Q(s, a; \theta_i))\nabla_{\theta_i} Q(s, a; \theta_i)]. \tag{8.5}$$

In this equation, s and a represent the state at current time and the action applied to the environment respectively. Furthermore, a minibatch training (sampled from the stored experience buffer) is also adopted to avoid divergence and smooth the learning.

8.2.1 DQN Problem formulation

A discrete control action is typically needed in the original application of RL control (e.g., robots). However, the WEC control is continuous, which therefore requires a reformulation of the RL control algorithm. This reformulation is successfully proposed/implemented in references [71] which applies a certain control law (e.g., damping control $u = -K_d x_2$) with the control coefficients (e.g., damping coefficient K_d) being adjusted by the RL technique. This technique is also applied in this paper to fulfill the requirement of a continuous control profile. Moreover, the existing methods

in the literature [71] typically apply a linear control strategy (e.g., the control coefficient will be updated approximately every 5 mins in terms of simulation time). In this manner, the control is adaptive to the constantly changing sea states (typically vary around every 10 mins to 15 mins), and within each RL control horizon (5 mins), the control strategy is linear. Unlike the existing methods, in this paper, the WEC control is formulated in the fashion of time-varying Proportional-Derivative (TVPD)

$$F_{PTO,ref} = -K_p(t)x_1 - K_d(t)x_2. \tag{8.6}$$

Instead of varying the control coefficients in a quasi-static (slow, say 5mins) manner which mainly aims at addressing the changing sea conditions, the TVPD coefficients ($K_p(t)$ and $K_d(t)$) is designed to be time-varying (fast and nonlinear, say 0.1s) which is expected to be more suitable to be applied to the proposed highly nonlinear system and provide more adaptivity. The feedback gains of the control signal are adjusted over time such that the generated electricity is optimized with the consideration of electrical PTO losses.

The states of the DQN agent are

$$s = [z,\, v,\, i_d,\, i_q], \tag{8.7}$$

which are required to propagate the wave-to-wire performance of the WEC (as described in Section. 3.2). In order to implement a continuous variation of the TVPD control coefficients, the action space of the DQN agent is defined as

$$A = \{a|[(+\delta K_p, 0), (0, +\delta K_d), (0, 0), \\ (-\delta K_p, 0), (0, -\delta K_d)]\} \tag{8.8}$$

where $\delta K_p = K_p(t + \delta t_{RL}) - K_p(t)$ and $\delta K_d = K_d(t + \delta t_{RL}) - K_d(t)$ are the small variations of the control coefficients. One can clearly tell from this equation that there are three possible strategies (includes 5 actions) at each DRL step: increase, maintain, or decrease. It is noted that, although, there should be 7 possible actions based on the described strategies; the action $(+\delta K_p, +\delta K_d)$ and $(-\delta K_p, -\delta K_p)$ are not considered to limit the action space [74]. According to Eq. (8.4), the optimal actions will be selected such that maximize the target based on the reward collected from the environment

$$r = P_e \tag{8.9}$$

where P_e is the generated electricity as described in Eq. (8.3). Moreover, considering the proposed wave-to-wire dynamics is complex, particularly the rapid dynamics of the electrical system needs to be captured by a very small time step ($\delta t = 0.0001$s used in this study) numerically. It will be extremely computational intense if the

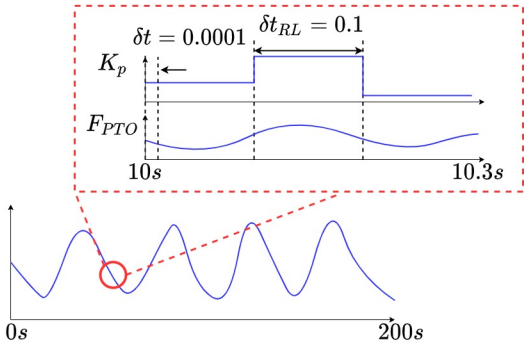

Figure 8.1: The explanation of the difference between the propagation time step and the DQN update step.

update of the DQN agent follows the same step size (say $\delta t = \delta t_{RL}$). Therefore, the DQN step (the update rate of the RL agent and also the frequency of applying an action) is specified as $\delta t_{RL} = 0.1$s in this paper, which is considered to be sufficient to present the time-varying characteristic of the control coefficients. In addition, the reward at the current step needs to be reformulated as

$$r = \frac{\sum P_e \delta t}{\delta t_{RL}} \tag{8.10}$$

which denotes the average electrical power within each DQN step. This concept is further explained in Figure 8.1.

It is worth noting that the reward described in the above equation is different from the definition of the cost function, which is typically used in optimal controls and optimization. If applying optimal control/optimization techniques to a WEC system, the cost function typically needs to be specified as $J = \int_0^T P_e dt$, which means the

objective of the control is to maximize the electricity generation over all the future horizon (e.g., the model predictive control [75]). This concept is still applied in DRL control, while through the Q-function, which represents the summation of the current reward and all the future discounted rewards, in which r only represents the reward at the current DRL step. Therefore, this demonstrates another advantage of the proposed DRL control: it does not require the wave prediction but instead relies on the direct feedback from the environment (current reward) and the maximization of all the reward (including current and future) is already embedded in the algorithm.

8.2.2 DQN control framework

The details of the DQN control framework are presented in Figure 8.2. As shown in the figure, the DQN agent is only composed of the critic network (which differs from other DRL algorithms that may be composed by both actor and critic network). The observed reward at current DRL step (r_t) and the new state (s_{t+1}) will be collected by the DQN agent after last action (a_t) has been executed. As we mentioned earlier, to improve the convergence and learning speed, the experience replay technique will be applied. Therefore, the experience of the agent needs to be stored: $e_t = [s_t, a_t, r_t, s_{t+1}]$ and saved in a experience buffer (D). A mini-batch will be randomly sampled from the experience buffer and used to train the deep Q-network (by using Eq. (8.5)). Finally, next action (a_{t+1}) will be decided by maximizing the target (refer

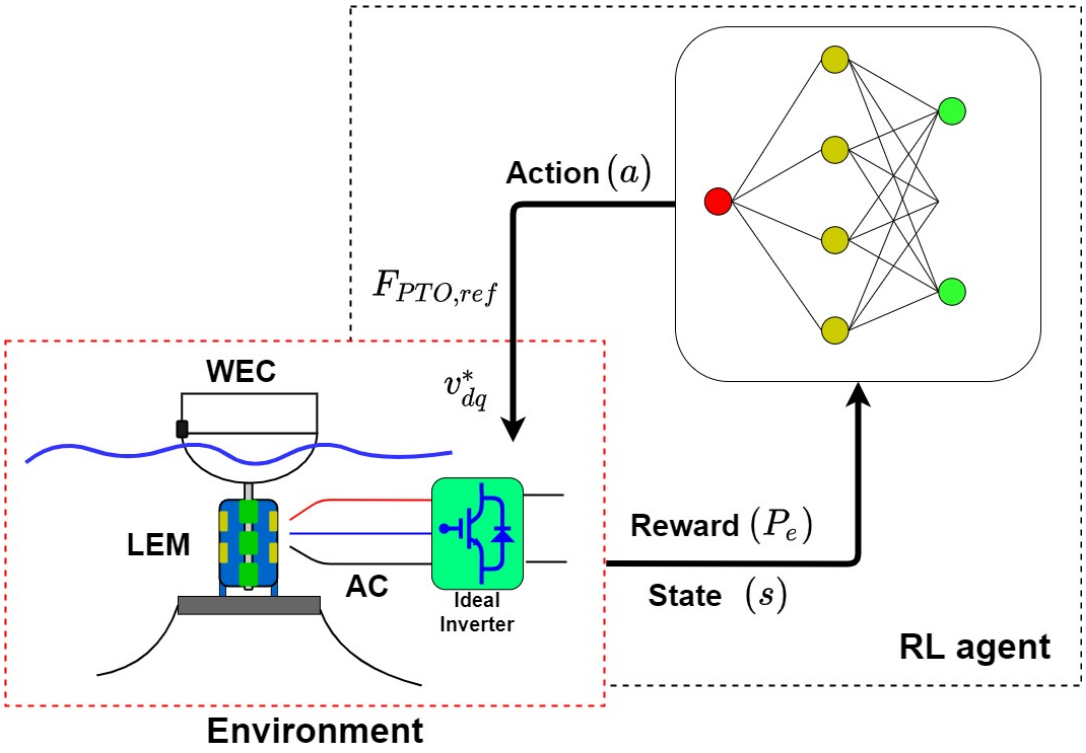

Figure 8.2: Block diagram of the DRL control

to Eq. (8.4)). It is also noted that there are two networks in the proposed learning algorithm (θ_i and θ_i^-). The target network (θ_i^-) will be updated by smoothing the Q network: $\theta_i^- = \tau\theta_i + (1-\tau)\theta_i^-$. The algorithm of the proposed DRL control is also summarized in Algorithm. 2. More details of the DQN algorithm can be found in reference [29]. Additionally, the DQN agent will be trained off-line [72] in this study (e.g., episodes), and the trained agent is directly applicable in real-time implementations.

As far as the model-based controls are concerned, the model-predictive control (MPC) [75], the Shape-Based (SB) control [24], and the proportional-derivative (PD) control

Initialization: Initialize replay memory D;
Initialize two action-value functions;
for *episode = 1, M* **do**
  Initialize the state s_0;
  for t *= 0,* T **do**
    Either select a random action $a_t \in A$ with probability ϵ or select greedy action which maximizes the target;
    Execute a_t, observe the reward r_t and the new state s_{t+1};
    Store the experience: $e_t = [s_t, a_t, r_t, s_{t+1}]$ in D;
    Sample a random minibatch from D and train the Q-network θ_i based on gradient descent;
    Synchronize the target network with the Q network;
  end
end

Algorithm 2: The DQN training algorithm

(time-invariant) will be implemented and compared with the performance of the proposed DRL control. In which the motion constraint (similar to the DRL control) is considered in designing the MPC and SB controls. Giving that the PD control is an unconstrained control, the physical limitations are directly implemented in the dynamics (e.g., end-stop). Readers of particular interests in these controls are directed to the references introduced above.

8.3 Results and Discussion

The numerical results are presented in detail in the following sections. The irregular wave which has a significant height of 1 m and a peak period of 8 s is applied as input in this chapter. All the simulations are conducted in MATLAB, and the cost of completing the training (number of episodes is selected as 2000) of the DQN agent

is around 24hrs.

8.3.1 DQN Agent Training

The agent needs to be trained before applied in real-time. The parameters that are used in the learning algorithm is summarized in Table. 8.1. In this research, the

Table 8.1
DRL hyperparameters

Hyperparameters	**Value**
optimizer	Adam
minibatch size	64
gradient threshold	1
replay memory size	10^4
learning rate	3×10^{-4}
number of hidden layers	2
number of neurons per hidden layer	24
discount factor	0.999
activation function	ReLU
target smoothing coefficient	10^{-3}
target update frequency	1

number of episodes is selected as 2000 which is considered to be sufficient for training of the agent. The overall discounted reward of each episode in the training is presented in Figure 8.3. One can tell from the figure that the episode reward starts to converge after around 1200 episodes.

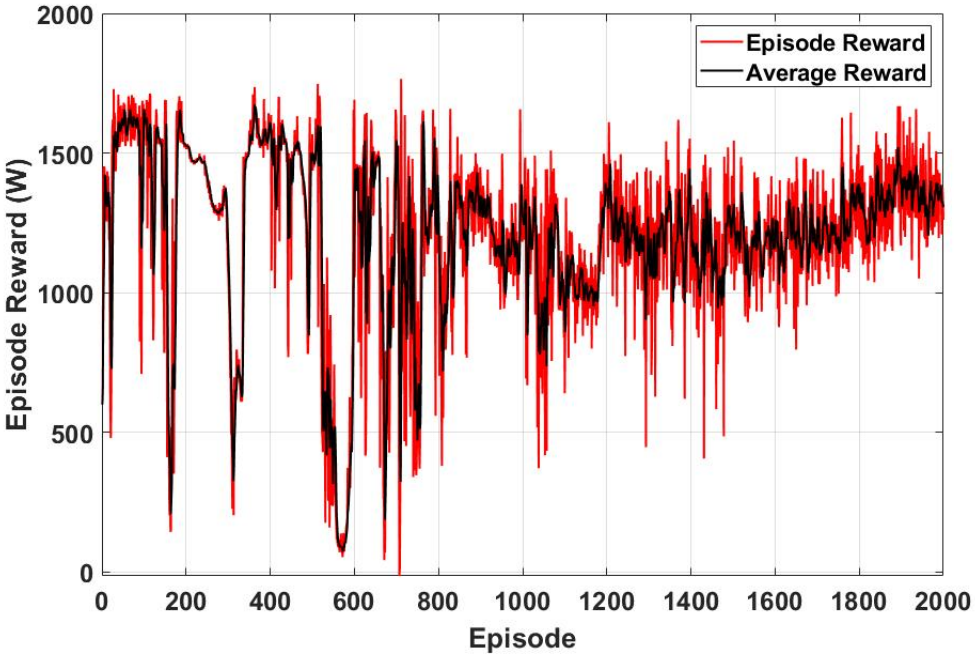

Figure 8.3: Reward per episode during training

8.3.2 Performance of Energy Extraction

One of the trained agents (which has a good performance in terms of episode reward) will be extracted to study more details. One of the most important critics to assess the performance of the proposed DRL control is the electrical power production (which is shown in Figure 8.4). In these simulations, 100 A is used as the current constraint. For readers who are interested in the performance of different model-based controls with various current limitations please refer to [4]. The figure indicates the trained DQN agent outperforms all the implemented model-based controls in terms of power

production. The SB control, which extracts the highest power among different model-based controls, only takes around 70% of the power produced by the DQN agent. However, this result cannot prove that the DRL control is a better control algorithm than the model-predictive-like control algorithms, since the DRL can extract more energy because PTO power loss is considered in the algorithm (global point of view). Similar research has been presented in the literature [27], the authors integrate the PTO copper loss function to the MPC cost function and increase the energy extraction performance by about 20 %, which means the model-predictive-like control schemes are also available for designing control from the global point of view. The advantages of the DRL are data-driven and with lower computational cost. The linear PD control has the worst performance because of the unrealistic design of the control gains (linear wave theory and impedance matching).

The difference between the linear PD control and the proposed DRL control can be further demonstrated by investigating the control coefficients. Figure 8.5 shows the comparison between the time-varying control coefficients (formulated in DRL control) and the linear PD control gains. The DRL control coefficients are constantly changing over time (particularly the $K_p(t)$) and are significantly different from the linear PD control gains. In conjunction with the results presented in Figure 8.4, the DRL control, which is associated with the time-varying profile in Figure 8.5, produces more energy. This result aligns well with the expectation: the proposed DRL control (formulated in a time-varying manner) shall outperform the one that is formulated

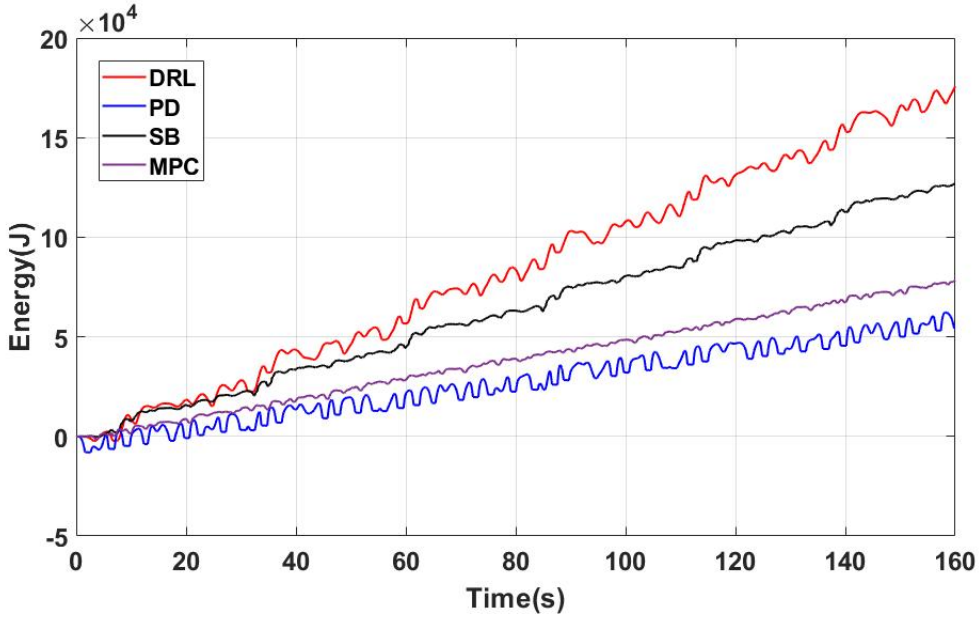

Figure 8.4: Reinforced learning and model-based control electrical energy outputs

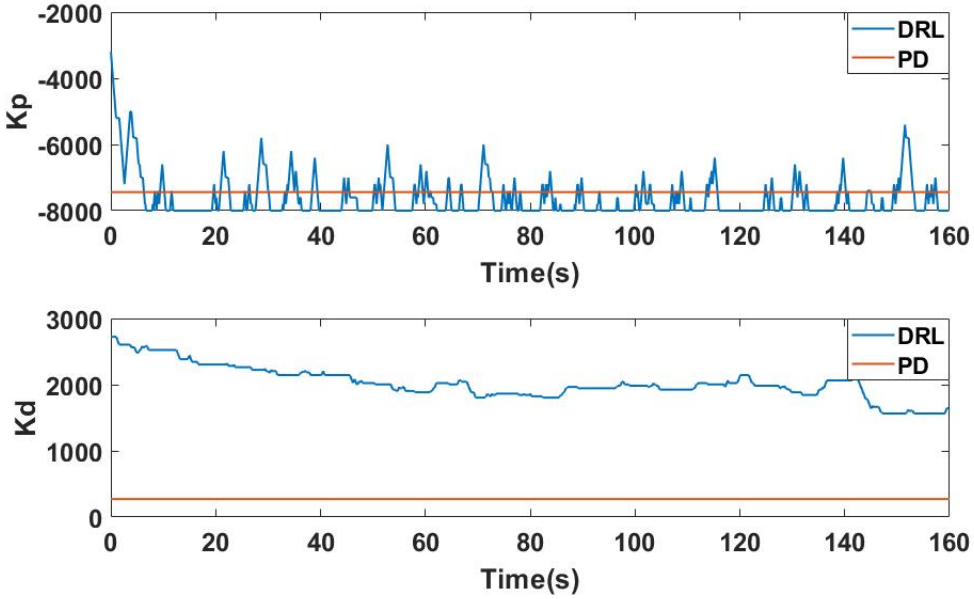

Figure 8.5: Trained DRL control coefficients

in a time-invariant manner because the system dynamics are highly nonlinear.

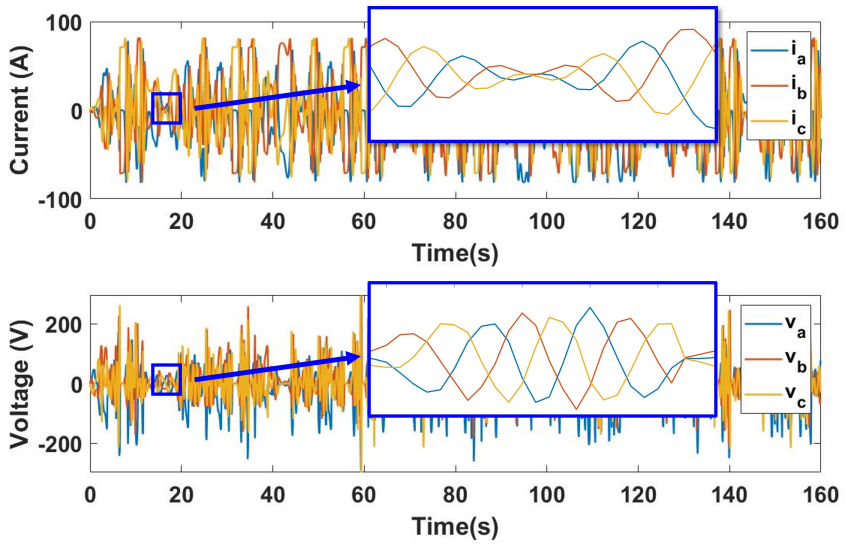

Figure 8.6: Circuit voltage and current from DRL

Moreover, the details of the system responses are presented as follows. The electrical drive current ($i_{a,b,c}$) and voltage ($v_{a,b,c}$) are shown in Figure 8.6. When zoomed in (the blue square), the AC current and voltage are smooth and balanced, which means the designed LEM model can fulfill the DRL control requirements. Additionally, the displacement, velocity, and control effort of the proposed DRL control are compared with model-based controls. Giving that the SB control has the best performance among model-based controls, it is selected for this comparison. As shown in Figure 8.7, the displacement of the DRL control is significantly larger than the displacement of the SB control, whilst they are both limited in the maximum stroke ($\pm$1.5m). This indicates the motion of the DRL control is more excited than the SB control, which is consistent with the results presented in Figure 8.4 (more power has been produced). Moreover, by comparing the time profile of the buoy velocity and control effort between different types of controls, it is seen that the system's responses

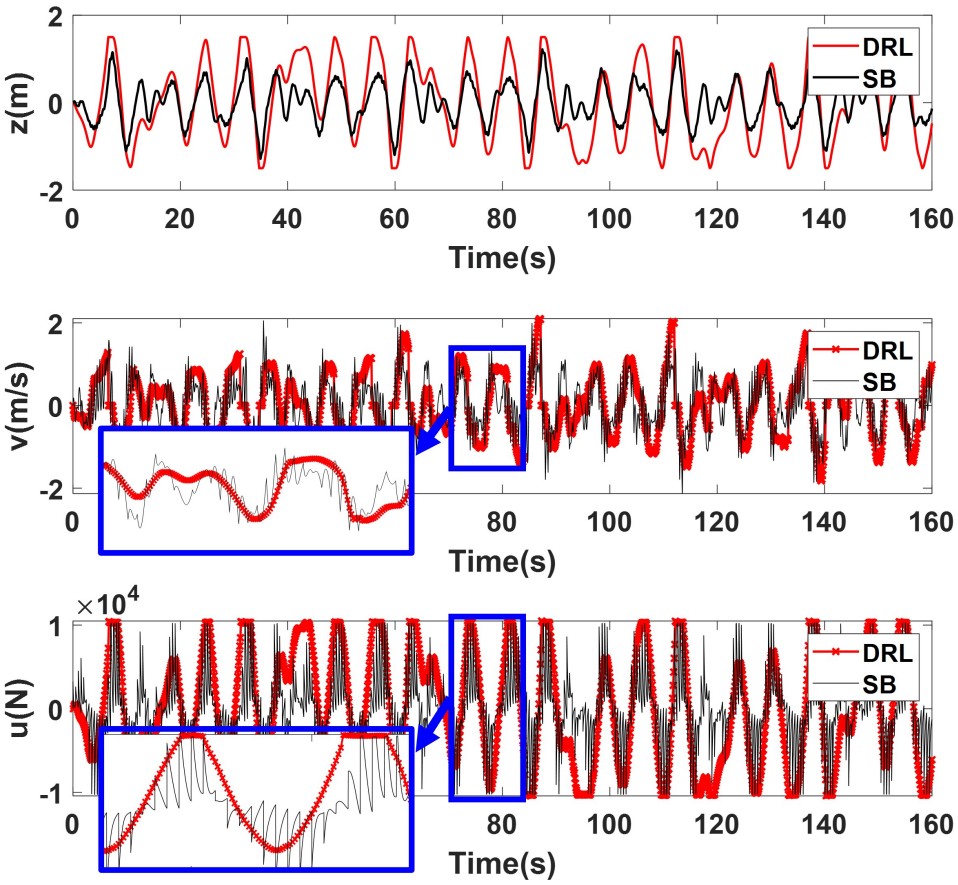

Figure 8.7: DRL, PD, and SB control buoy displacement velocity and control force

generated by the DRL control are significantly smoother, which is considered to be more ideal in practice (e.g., higher efficiency of the electrical PTO). It is also clear that the SB control force is oscillating around the DRL control profile (shown in the zoom-in scope). The sudden change of the SB control force is caused by the update of the control (starting a new finite prediction horizon). Theoretically, these oscillations can be eliminated if the prediction horizon of the SB control is assumed to be infinite. More details of the SB control can be found in reference [24]. In conclusion, the DRL control not only has a better performance than the model-based control in terms of

energy production but also generates smoother system responses which indicate it is more meaningful in practical applications.

8.3.3 Performance of Power Losses

Model-based control relies on accurate dynamic models to achieve optimal results. However, the proposed control schemes (PD, MPC SB) only consider the buoy heave motion dynamics instead of the wave-to-wire modeling so that the actual electrical outputs will be far away from the ideal mechanical outputs [4]. The additional power loss model, which is introduced by the PTO dynamics, will have a great impact on the WEC power extraction efficiency. As it has been discussed in [3], the PTO power is bi-directional (active and reactive power) in reactive power control schemes, so that there will be power losses in both directions, which means the PTO has to provide more reactive power and extract less active power due to the PTO losses. The electrical PTO operation efficiency can be expressed as

$$\begin{aligned} \eta_{ra} &= \frac{|P_{mech,ra}|}{|P_{e,ra}|} \\ \eta_{a} &= \frac{|P_{e,a}|}{|P_{mech,a}|} \end{aligned} \tag{8.11}$$

where the η_{ra} and η_a are the electrical PTO operation efficiencies while providing reactive power and extracting active power respectively, the P_{mech} ($P_{mech} = u\dot{z}$) is

the mechanical power on the buoy side, the $P_{mech,a}$ is the buoy side mechanical power while the WEC is extacting active power and the $P_{mech,ra}$ is the buoy side mechanical power while the WEC is providing reactive power, the P_e (Eq. (8.3)) is the electrical power output, similarly the $P_{e,a}$ and the $P_{e,ra}$ are the active and reactive output power accordingly. The absolute value has been applied in the calculation to eliminate the power flow direction effects.

From Eq. (8.11), the electrical drive operational efficiencies under all operating conditions are shown in Figure 8.8. Due to the different sizes of the simulation time steps in the DRL and SB, the efficiency calculation in the SB (smaller time step) is based upon mean values (mean of the large time step period as in DRL) to have the same amount of the operation points. Comparing these two efficiency maps, the DRL can have higher PTO efficiencies even the required control force is high (the blue trapezoid area in the Figure 8.8 top). On the other hand, the SB control can only achieve higher operation efficiency while the required control force is low (the blue circle area in Figure 8.8 bottom). From Eq. (3.15), a high required control force will end up with high current flow in the electrical drive, resulting in more electrical power losses. This is why the SB can only achieve higher PTO efficiencies while the control force is low. However, the DRL can learn and consider the PTO loss and power extraction trade-off. The large control force will be demanded only when large extraction powers are available. This strategy will end up with higher operating efficiencies due to a large amount of power is extracted by the PTO, although the PTO loss is more.

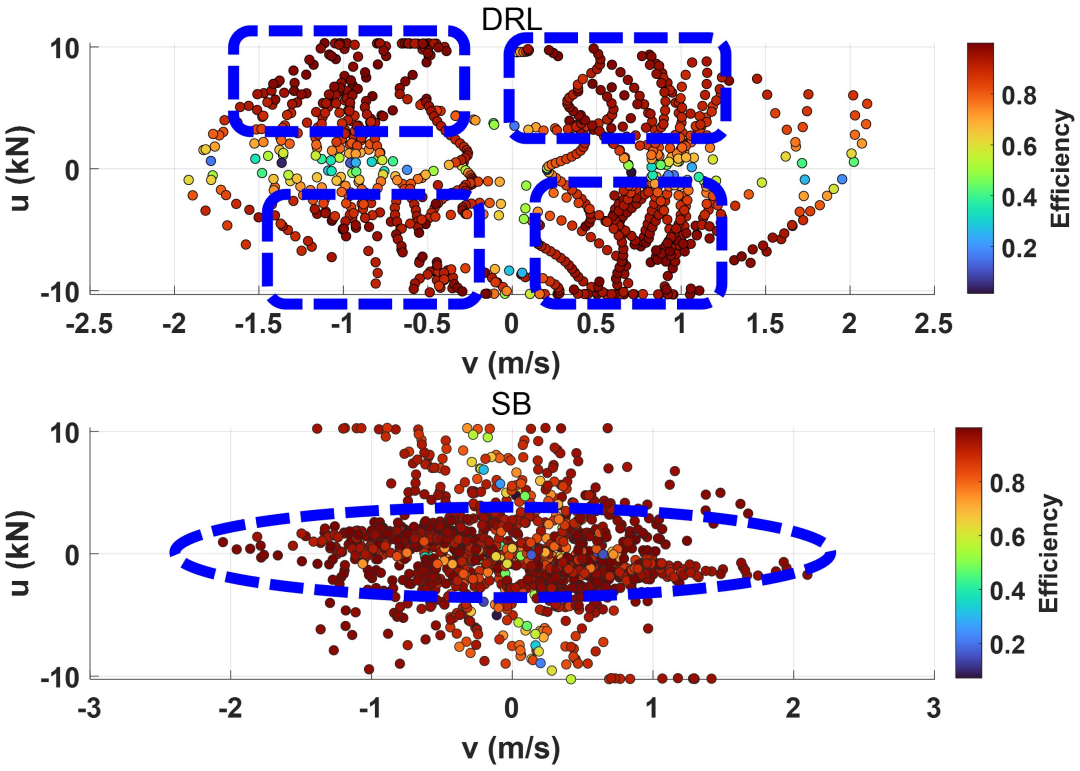

Figure 8.8: Electrical drive operation point efficiency in SB and DRL control

The results of the DRL and the SB control PTO operation efficiencies with respect to the electrical power outputs are shown in Figure 8.9. The efficiency calculation in the SB also relies on the mean power as in Figure 8.8. The positive electrical power in the figure is the extracted (active) power from the PTO, and the negative electrical power in the figure is the provided (reactive) power from the PTO. It further proves that the DRL can extract higher power with high efficiencies. The absolute values of the electrical powers from the SB are much lower (the black dots locate more centrally) than the DRL, which means the DQN agent is capable of extracting more energy with the same PTO control force (current) constraint under nonlinear dynamics.

Figure 8.8 and 8.9 demonstrate the importance of designing a control by considering the overall system dynamics [4]. The model-based controls (e.g., SB) are typically derived only based on linear hydrodynamics without considering the PTO dynamics, which makes the design of the control less cumbersome. In comparison, it is clearly proved in the figures that, when the design of the control is isolated from the PTO dynamics (or more generally, overall dynamics), it causes troubles for an electrical engineer to design a PTO to support this force (as shown in the figures, only has a good efficiency in low power range). It actually has been found in our previous study [4], without limiting the PTO force (basically limits the power flow), a major part of the wave power will be lost in the circuit. In contrast, the DRL control is designed based on wave-to-wire dynamics. As shown in the figures, an optimal path has been found by the DRL control (high power and high efficiency) such that a large amount of wave power can be successfully transmitted to electricity but not all being lost in the circuit (e.g., SB control).

The output electrical power qualities from the selected controls are evaluated and compared as well. The max and mean output power are shown in Figure 8.10. The mean extraction power of the whole time frame is shown as the black bar in the figure, and the DRL has the highest. The max electrical power from the PTO is shown in the red bar, and the DRL has the second lowest. The variation of the output power from the DRL is the smallest. To further prove that the output power from the DRL has the best power quality, the coefficient of variation (COV) and the peak to average

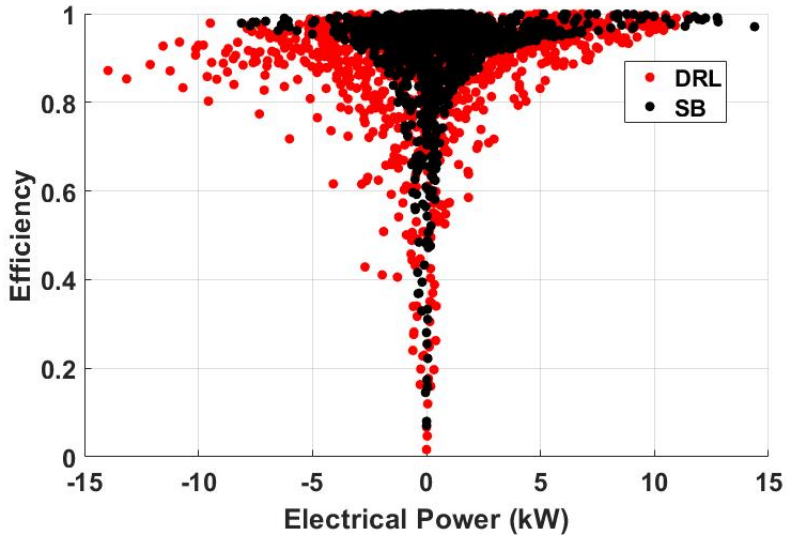

Figure 8.9: Electrical drive operation point efficiency in SB and DRL control with respect to PTO power

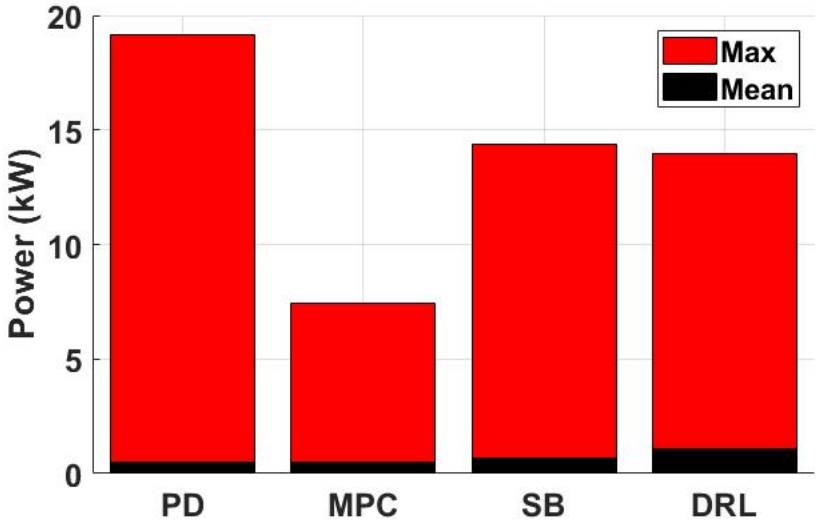

Figure 8.10: Output max and mean power bar plot

(PTA) ratios are applied. The two ratios are calculated by the equations as

$$r_{COV} = \frac{\sigma(P_e(t))}{\bar{P}_e(t)}$$
$$r_{PTA} = \frac{max(|P_e(t)|)}{\bar{P}_e(t)} \tag{8.12}$$

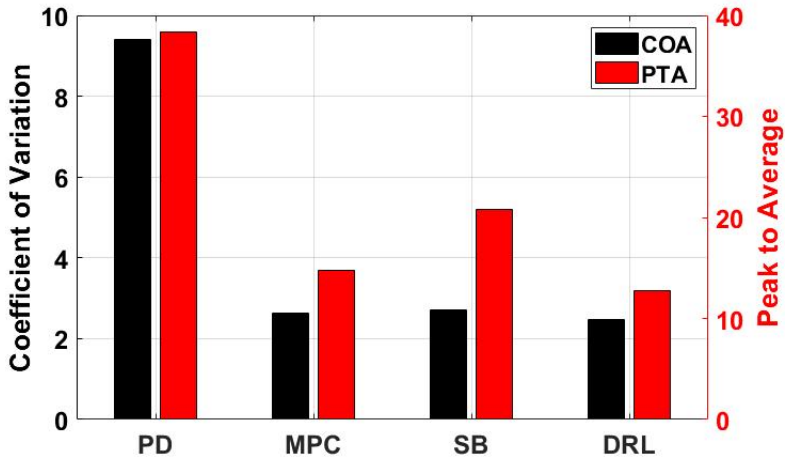

Figure 8.11: Output power coefficient of variation and peak to average bar plot

where the r_{COV} and the r_{PTA} are the ratios, $\sigma(P_e(t))$ is the standard deviation of the electrical power output time-series, the $max(|P_e(t)|)$ is the maximum absolute value of the output power time-series, and the $\bar{P}_e(t)$ is the mean value of the output power time-series. According to Eq. (8.12), the COV and PTO ratios of all the selected controls are shown in Figure 8.11. According to Figure 8.11, both the COV and PTA ratios of the DRL are the lowest. Comparing to other controls, the MPC and SB can have low COVs as well. However, the PTA ratios of the MPC, SB, and the PD are much larger than the DRL, which means there are power fluctuations during the PTO operations, and it reflects as power spikes in the output power profiles. Those power spikes can be caused by the PTO hard constraints (e.g., PTO stoke limit) and the model-predictive horizon setup, the control force will not be smooth every time when the PTO reaches the constraint limit, or the model-predictive horizons are transient (as shown in the Figure 8.7(bottom)). The PD control will not consider any PTO

constraints, resulting in that the buoy oscillation will violate the PTO stroke limits significantly, so it ends up with little power will be extracted and exceeding output power spikes. The MPC and SB will saturate the WEC buoy oscillation based upon the PTO limit, so few of the stroke limit violations will happen in these two controls. However, an infinite prediction horizon cannot be applied in these two controls due to the high compute cost, so that the output power spikes will happen every time when the prediction horizon is transient. Different from these model-based controls, the DRL provides a smooth control force profile while considering the PTO constraints and losses, so the output power quality is better compared to other methods.

8.3.4 Performance in Real Ocean Waves

Ground-truth ocean wave data is very important to evaluate the wave energy potentials, especially for specific off-shore application designs, such as described in [1], the Martha's Vineyard ground-truth wave data is applied to size the ESS. The Pacific Northwest of the U.S. is one of the greatest wave power resources in the world [76]. So the PacWave ocean wave data from the PacWave wave resource assessment report [33] will be applied in this section to evaluate the wave energy extraction performances of the model-based control schemes and the DRL. According to the report, the monthly mean values of the significant wave height (H_s) and energy period (T_{energy}) are shown in the Table 8.2, in which the energy period T_{energy} can be converted to peak period

(T_p) by applying a factor 0.83 as $T_p = \frac{T_{energy}}{0.83}$ [77].

Table 8.2
PacWave Wave Data

Month	H_s (m)	T_{energy} (s)
Jan.	3.2	11.2
Feb.	3.1	11.3
Mar.	2.8	10.8
Apr.	2.4	10.0
May	1.9	9.2
June	1.7	8.8
July	1.5	8.2
Aug.	1.5	8.6
Sep.	1.7	9.2
Oct.	2.3	10.2
Nov.	3.0	10.6
Dec.	3.2	11.2

From the ocean wave data in Table 8.2, a 300 s time series has been simulated for each month, and the extracted mean power is obtained. The mean power results are shown in Table 8.3. The DRL can achieve a higher monthly mean power than the other two control schemes. For the months which have aggressive waves (in Jan., Feb., Mar., Apr., Oct., Nov., and Dec.), the SB control cannot be implemented on the WEC device in this paper due to the small PTO stroke limit (3 m). Poor SB parameter setups (e.g., extremely small prediction horizon) have to be applied to decrease the buoy oscillation displacement to the limit intentionally, which makes the SB be meaningless. The NaN in the Table 8.3 shows the inapplicable months. In May and Sep., the waves are still aggressive for the WEC device under the SB control, resulting in that the monthly mean powers are still lower. The SB can achieve the highest monthly mean in July; the value is about 80% of the one from DRL. As it

has been explained in the former section, the trained agent from the DRL can make decisions based upon the mean power of the whole time frame instead of the limited prediction horizon, and there is no computational cost consideration. A well-trained agent can obtain results that are close to the optimal values, and the results can reflect the actual potentials of the energy extraction in the specific ocean area with the specific WEC design. To better compare the energy extraction performances of the selected controls, the monthly mean power bar plot is shown in Figure 8.12. The DRL consistently has the highest mean power for the whole year, which means it is robust for various wave conditions. On the other hand, the SB relies on the WEC device design and wave conditions more, so that the monthly mean varies significantly and is sometimes not applicable.

Table 8.3
PacWave Monthly Mean Power Results

Month	**DRL** $P_{mean}(kW)$	**SB** $P_{mean}(kW)$	**PD** $P_{mean}(kW)$
Jan.	2.20	NaN	0.72
Feb.	2.11	NaN	0.73
Mar.	2.06	NaN	0.69
Apr.	1.94	NaN	0.69
May	1.70	0.22	0.67
June	1.59	0.92	0.63
July	1.47	1.17	0.64
Aug.	1.45	0.91	0.64
Sep.	1.51	0.24	0.65
Oct.	1.82	NaN	0.68
Nov.	2.10	NaN	0.70
Dec.	2.17	NaN	0.73

To further evaluate and discuss the output power qualities of the selected controls, the COV and PTA ratios of the PacWave monthly power time series are shown in

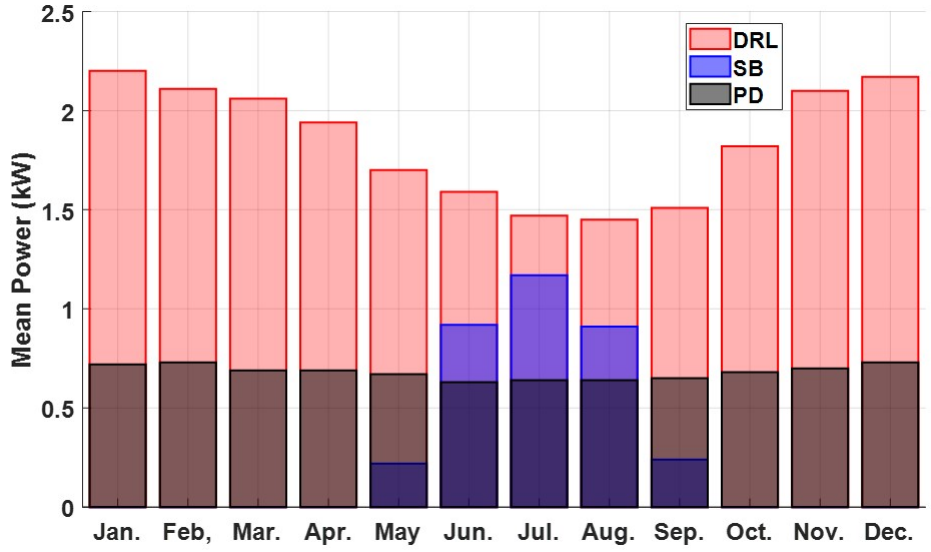

Figure 8.12: PacWave monthly mean power from DRL, SB, and PD

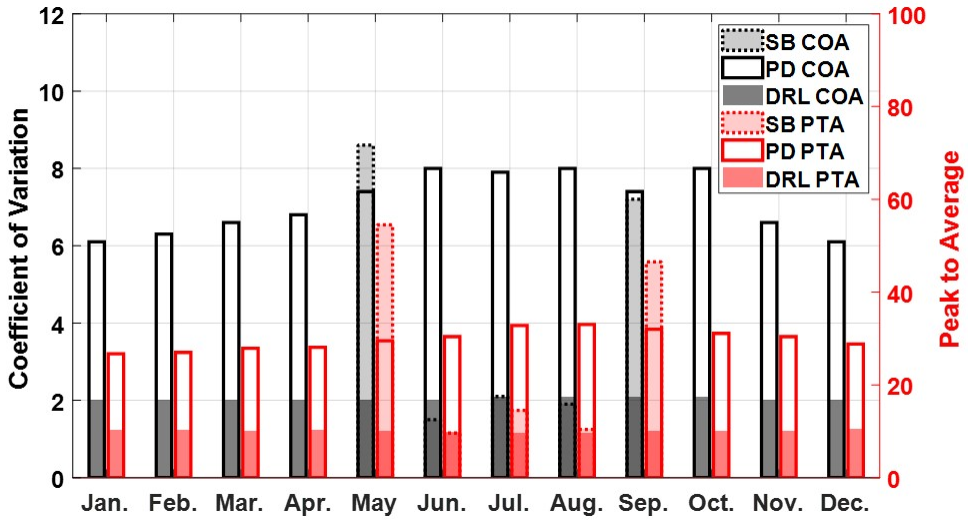

Figure 8.13: PacWave monthly power time-series coefficient of variation and peak to average from DRL, SB, and PD

Figure 8.13. Similar to the results in Figure 8.11, the DRL consistently has the lowest COV and PTA. The SB can obtain small COV and PTO ratios in July. However, as it has been discussed in the former sections, the SB relies on the WEC design and wave conditions, resulting in that the power qualities vary significantly in different wave

conditions, such as May and Sep., the COV and PTA ratios of the SB are significantly high. From the monthly mean power results and the power quality analysis, it further shows that the well-trained agent from the DRL can make so much better decisions for controlling the WEC buoy while considering the PTO constraints and losses that the energy extraction performance of the DRL is the best comparing to other selected model-based controls.

8.4 Conclusion

In this chapter, the DRL control is applied to the small-scaled direct-drive WEC system to study and assess the power extraction performances. A real PTO dynamics is implemented in the wave-to-wire model in addition to the buoy hydrodynamics. Considering the model-based controls are typically only developed based on the hydrodynamics (local point of view), it is expected that the actual electricity produced by the model-based controls is significantly lower than the wave power production predicted in ideal conditions. In contrast, the DRL control does not rely on the explicit description of the environment (model-free), which makes it possible to be designed from a global point of view (based on the wave-to-wire model). The simulation results show the proposed DRL control outperforms the model-based controls in terms of power production, power losses, and operational efficiencies. Furthermore, the power produced by the DRL control has a better quality compared to model-based

controls by assessing the COV and PTA ratios. Finally, the DRL control performance is further validated by using the real ocean data at PacWave. The results show the proposed control is robust and can consistently achieve the highest monthly mean power with the best power qualities. In the future, more complex hydrodynamics (e.g., weakly nonlinear model) and the dynamics of other subsystems (e.g., mooring system) can be included to have a more accurate description of the behavior of a WEC system. Additionally, the PTO model can also be improved (e.g., include an actual efficiency map) to have a more realistic consideration of all the losses.

Chapter 9

Conclusion and Future Work

This research focuses on the WEC wave-to-wire control performance assessment and development. By studying the PTO and electrical drive behaviors in wave-to-wire model, this research indicates that the actual PTO and electrical drive constraints will have significant impacts on the WEC energy extraction performance. Meanwhile, the model-based controls, which are designed from a local point of view (based upon buoy hydrodynamics only), cannot achieve or get close to the optimal results as they proposed in the literature (ideal PTO conditions). This research starts with the WEC electrical PTO static modeling (Chapter 5). By studying the LEM operation limits and efficiency constraints, the result indicates that the WEC wave-to-wire output will be far away from the ideal output signal which based upon buoy hydrodynamic model. To design and size the PTO and ESS for off-shore applications (e.g., sensors),

years of ground-truth ocean wave data need to be assessed and the statistical study is demanded to improve the design reliability. Wave-to-wire static model provides a straightforward method to fast evaluate the large ground-truth data base and obtain a more accurate assessment (Chapter 6). However, to develop and increase the WEC wave-to-wire energy extraction efficiency and meet the goal of decreasing the wave energy levelized cost, studying the WEC wave-to-wire static model only is not enough, the PTO dynamic behaviors and power loss model are demanded. So in the Chapter 7, the buoy hydrodynamic model and the electrical PTO model are coupled. State of the art model-based control schemes are applied and their performance is assessed. The electrical PTO linear (circuit resistance) and non-linear (efficiency map) power loss model are both included. By studying the electrical PTO behaviors, it further proves that the buoy hydrodynamic model-based control will not consider the actual PTO impacts so that the actual outputs are far from optimal. To improve this, there are several possible solutions have been discussed. Improving the LEM design could be a very straightforward way, but it is not robust for all wave conditions, and the hardware cost could increase the wave energy levelized cost instead of decreasing it. Implementing an extra gear system between the buoy and the PTO to manipulate the PTO operation points could be another straightforward engineering solution. However, the gear system will introduce new dynamics and complex the model even more. The actual design and performance evaluation can be included in the future work. Besides these two methods, designing controls from the global point of views

that consider the whole wave-to-wire performance is demanded. Similar to the buoy hydrodynamic model-based controls, designing a wave-to-wire model-based control is another solution. Similar research [27] has shown that considering PTO copper loss in the MPC cost function will improve the WEC wave-to-wire performance significantly. However, it would be very difficult to consider the PTO non-linear loss model due to the complexities of the wave-to-wire model and the computational cost would be significant. A totally different strategy from the model-based controls came into being, which is the machine reinforcement learning. Unlike the model-based control, the RL does not rely on the accurate dynamic models (data-driven and model-free) that much so the complexities and computational cost will be decreased greatly. The details of how to apply the DRL on the WEC wave-to-wire model has been discussed in Chapter 8. The results prove that the DRL control can achieve much higher extraction mean power and much better power quality comparing to the selected buoy hydrodynamic model-based controls. Furthermore, to assess the robustness of the DRL control, one-year PacWave ground-truth ocean wave data are applied in Chapter 8 as well. The results turn out that the DRL control can consistently have the highest mean power and best power quality throughout the whole year.

To summarize, the DRL control would be the best solution (comparing to other discussed ones) for improving the WEC wave-to-wire performance and decreasing the levelized cost. In the future, more new designs should be considered and evaluated

(e.g., extra gear system, etc.). More complex DRL reward function should be considered in the future, such as buoy motion in 6 DoFs, output power quality penalties and non-linear PTO power loss model, etc. Meanwhile, how to apply the DRL on the WEC array wave-to-wire modeling is a new challenge due to that the WEC array performance will rely on the global control even more, and the grid-connected power quality requirements are more strict. The WEC array model-based controls (e.g., collective control) and the DRL control performance assessments are demanded.

References

[1] X. Zhou, O. Abdelkhalik, and W. Weaver, "Power take-off and energy storage system static modeling and sizing for direct drive wave energy converter to support ocean sensing applications," *Journal of Marine Science and Engineering*, vol. 8, no. 7, p. 513, 2020.

[2] X. Zhou, M. Jafari, O. Abdelkhalik, U. A. Korde, and L. Gauchia, "Statistical energy storage sizing for point absorber wave energy converters (wecs): A device for operation off the us east coast," in *International Conference on Offshore Mechanics and Arctic Engineering*, vol. 51319, p. V010T09A023, American Society of Mechanical Engineers, 2018.

[3] X. Zhou, S. Zou, W. W. Weaver, and O. Abdelkhalik, "Control of wave energy converter with losses in electrical power take-off system," in *ASME Power Conference*, vol. 85109, p. V001T09A006, American Society of Mechanical Engineers, 2021.

[4] X. Zhou, S. Zou, W. W. Weaver, and O. Abdelkhalik, "Assessment of electrical power generation of wave energy converters with wave-to-wire modeling," *Journal of Transactions on Sustainable Energy*, Under Review.

[5] S. Zou, X. Zhou, I. Khan, W. W. Weaver, and S. Rahman, "Optimization of the electricity generation of a wave energy converterusing deep reinforcement learning," in *Ocean Engineering*, vol. Under review.

[6] M. K. Hubbert, "Nuclear energy and the fossil fuel," in *Drilling and production practice*, OnePetro, 1956.

[7] M. Hoogwijk and W. Graus, "Global potential of renewable energy sources: a literature assessment," *Background report prepared by order of REN21. Ecofys, PECSNL072975*, 2008.

[8] A. K. Raturi, "Renewables 2019 global status report," 2019.

[9] R. Bedard, M. Previsic, G. Hagerman, B. Polagye, W. Musial, J. Klure, A. von Jouanne, U. Mathur, C. Collar, C. Hopper, *et al.*, "North american ocean energy status-march 2007," *Electric Power Research Institute (EPRI) Tidal Power (TP)*, vol. 8, p. 17, 2007.

[10] S. Zou, O. Abdelkhalik, R. Robinett, G. Bacelli, and D. Wilson, "Optimal control of wave energy converters," *Renewable energy*, vol. 103, pp. 217–225, 2017.

[11] M. A. Mustapa, O. Yaakob, Y. M. Ahmed, C.-K. Rheem, K. Koh, and F. A. Adnan, "Wave energy device and breakwater integration: A review," *Renewable and Sustainable Energy Reviews*, vol. 77, pp. 43–58, 2017.

[12] G. Bacelli, *Optimal control of wave energy converters*. National University of Ireland, Maynooth (Ireland), 2014.

[13] B. Drew, A. R. Plummer, and M. N. Sahinkaya, "A review of wave energy converter technology," 2009.

[14] N. Stauffer, *Catch the wave*. MIT News, MIT Energy Initiative, December 17, 2008.

[15] J. Luoma, *Capturing the Ocean's Energy*. Yale Environment 360, Yale School of the Environment, DECEMBER 1, 2008.

[16] A. A. Faiad and I. Gowaid, "Linear generator technologies for wave energy conversion applications: A review," in *2018 53rd International Universities Power Engineering Conference (UPEC)*, pp. 1–6, IEEE, 2018.

[17] V. S. Neary, P. H. Kobos, D. S. Jenne, and Y.-H. Yu, "Levelized cost of energy for marine energy conversion (mec) technologies.," tech. rep., Sandia National Lab.(SNL-NM), Albuquerque, NM (United States), 2016.

[18] S. Zou and O. Abdelkhalik, "Control of wave energy converters with discrete

displacement hydraulic power take-off units," *Journal of Marine Science and Engineering*, vol. 6, no. 2, p. 31, 2018.

[19] O. Farrok, M. R. Islam, M. R. I. Sheikh, Y. G. Guo, and J. G. Zhu, "Design and analysis of a novel lightweight translator permanent magnet linear generator for oceanic wave energy conversion," *IEEE Transactions on Magnetics*, vol. 53, no. 11, pp. 1–4, 2017.

[20] J. Zhang, H. Yu, Q. Chen, M. Hu, L. Huang, and Q. Liu, "Design and experimental analysis of ac linear generator with halbach pm arrays for direct-drive wave energy conversion," *IEEE Transactions on Applied Superconductivity*, vol. 24, no. 3, pp. 1–4, 2014.

[21] L. Huang, M. Chen, L. Wang, F. Yue, R. Guo, and X. Fu, "Analysis of a hybrid field-modulated linear generator for wave energy conversion," *IEEE Transactions on Applied Superconductivity*, vol. 28, no. 3, pp. 1–5, 2018.

[22] H. Jing, N. Maki, T. Ida, and M. Izumi, "Design study of large-scale hts linear generators for wave energy conversion," *IEEE Transactions on Applied Superconductivity*, vol. 27, no. 4, pp. 1–5, 2017.

[23] G. Bacelli and J. V. Ringwood, "Numerical optimal control of wave energy converters," *IEEE Transactions on Sustainable Energy*, vol. 6, no. 2, pp. 294–302, 2014.

[24] O. Abdelkhalik, R. Robinett, S. Zou, G. Bacelli, R. Coe, D. Bull, D. Wilson, and U. Korde, "On the control design of wave energy converters with wave prediction," *Journal of Ocean Engineering and Marine Energy*, vol. 2, no. 4, pp. 473–483, 2016.

[25] B. A. Ling, B. Bosma, and T. K. Brekken, "Experimental validation of model predictive control applied to the azura wave energy converter," *IEEE Transactions on Sustainable Energy*, vol. 11, no. 4, pp. 2284–2293, 2019.

[26] D. García-Violini, Y. Peña-Sanchez, N. Faedo, C. Windt, F. Ferri, and J. V. Ringwood, "Experimental implementation and validation of a broadband lti energy-maximizing control strategy for the wavestar device," *IEEE Transactions on Control Systems Technology*, 2021.

[27] A. de la Villa Jaén, A. G. Santana, *et al.*, "Considering linear generator copper losses on model predictive control for a point absorber wave energy converter," *Energy Conversion and management*, vol. 78, pp. 173–183, 2014.

[28] M. Penalba and J. V. Ringwood, "A high-fidelity wave-to-wire model for wave energy converters," *Renewable energy*, vol. 134, pp. 367–378, 2019.

[29] V. Mnih, K. Kavukcuoglu, D. Silver, A. Graves, I. Antonoglou, D. Wierstra, and M. Riedmiller, "Playing atari with deep reinforcement learning," *arXiv preprint arXiv:1312.5602*, 2013.

[30] R. Collobert and J. Weston, "A unified architecture for natural language processing: Deep neural networks with multitask learning," in *Proceedings of the 25th international conference on Machine learning*, pp. 160–167, 2008.

[31] A. Krizhevsky, I. Sutskever, and G. E. Hinton, "Imagenet classification with deep convolutional neural networks," *Advances in neural information processing systems*, vol. 25, pp. 1097–1105, 2012.

[32] D. Silver, A. Huang, C. J. Maddison, A. Guez, L. Sifre, G. Van Den Driessche, J. Schrittwieser, I. Antonoglou, V. Panneershelvam, M. Lanctot, *et al.*, "Mastering the game of go with deep neural networks and tree search," *nature*, vol. 529, no. 7587, pp. 484–489, 2016.

[33] G. Dunkle, B. Robertson, G. García-Medina, and Z. Yang, "Pacwave wave resource assessment," 2020.

[34] Z. Zhang, C. Hackl, F. Wang, Z. Chen, and R. Kennel, "Encoderless model predictive control of back-to-back converter direct-drive permanent-magnet synchronous generator wind turbine systems," in *2013 15th European Conference on Power Electronics and Applications (EPE)*, pp. 1–10, 2013.

[35] D. G. Wilson, W. W. Weaver, R. D. Robinett, and S. F. Glover, "Nonlinear power flow control design for networked ac/ dc based microgrid systems," in *2018 Annual American Control Conference (ACC)*, pp. 5698–5705, 2018.

[36] A. Muetze and J. Vining, "Ocean wave energy conversion-a survey," in *Conference record of the 2006 IEEE industry applications conference forty-first IAS annual meeting*, vol. 3, pp. 1410–1417, IEEE, 2006.

[37] W. Cummins, D. T. M. B. W. D. C., and D. W. T. M. Basin, *The Impulse Response Function and Ship Motions*. Report (David W. Taylor Model Basin), Navy Department, David Taylor Model Basin, 1962.

[38] A. Babarit and G. Delhommeau, "Theoretical and numerical aspects of the open source bem solver nemoh," in *11th European Wave and Tidal Energy Conference (EWTEC2015)*, 2015.

[39] C. T. Rim, N. S. Choi, G. C. Cho, and G. H. Cho, "A complete dc and ac analysis of three-phase controlled-current pwm rectifier using circuit dq transformation," *IEEE Transactions on Power Electronics*, vol. 9, no. 4, pp. 390–396, 1994.

[40] S. Eriksson, "Design of permanent-magnet linear generators with constant-torque-angle control for wave power," *Energies*, vol. 12, no. 7, p. 1312, 2019.

[41] T. Hassell, W. W. Weaver, R. D. Robinett, D. G. Wilson, and G. G. Parker, "Modeling of inverter based ac microgrids for control development," in *2015 IEEE Conference on Control Applications (CCA)*, pp. 1347–1353, IEEE, 2015.

[42] L. Wang and J. Isberg, "Nonlinear passive control of a wave energy converter subject to constraints in irregular waves," *Energies*, vol. 8, no. 7, pp. 6528–6542, 2015.

[43] J. Song, O. Abdelkhalik, R. Robinett, G. Bacelli, D. Wilson, and U. Korde, "Multi-resonant feedback control of heave wave energy converters," *Ocean Engineering*, vol. 127, pp. 269–278, 2016.

[44] J. Hals, J. Falnes, and T. Moan, "Constrained optimal control of a heaving buoy wave-energy converter," *Journal of Offshore Mechanics and Arctic Engineering*, vol. 133, no. 1, 2011.

[45] A. Brown, J. Thomson, and C. Rusch, "Hydrodynamic coefficients of heave plates, with application to wave energy conversion," *IEEE Journal of Oceanic Engineering*, vol. 43, no. 4, pp. 983–996, 2017.

[46] D. G. Wilson, R. D. Robinett, G. Bacelli, O. Abdelkhalik, W. W. Weaver, and R. Coe, "Nonlinear wec optimized geometric buoy design for efficient reactive power requirements," in *OCEANS 2019 MTS/IEEE SEATTLE*, pp. 1–6, IEEE, 2019.

[47] "Available online: https://mvco.whoi.edu/data-history," accessed on 4 May 2020.

[48] M. N. Allahdadi, B. Gunawan, J. Lai, R. He, and V. S. Neary, "Development and validation of a regional-scale high-resolution unstructured model for wave energy resource characterization along the us east coast," *Renewable Energy*, vol. 136, pp. 500–511, 2019.

[49] V. S. Neary, S. Ahn, B. E. Seng, M. N. Allahdadi, T. Wang, Z. Yang, and R. He, "Characterization of extreme wave conditions for wave energy converter design and project risk assessment," *Journal of Marine Science and Engineering*, vol. 8, no. 4, p. 289, 2020.

[50] U. A. Korde, J. Song, R. D. Robinett, and O. O. Abdelkhalik, "Hydrodynamic considerations in near-optimal control of a small wave energy converter for ocean measurement applications," *Marine Technology Society Journal*, vol. 51, no. 6, pp. 44–57, 2017.

[51] C. Lee, "Theory manual," 1995.

[52] S. Prakash, K. Mamun, F. Islam, R. Mudliar, C. Pau'u, M. Kolivuso, and S. Cadralala, "Wave energy converter: a review of wave energy conversion technology," in *2016 3rd Asia-Pacific World Congress on Computer Science and Engineering (APWC on CSE)*, pp. 71–77, IEEE, 2016.

[53] S. Foteinis and T. Tsoutsos, "Strategies to improve sustainability and offset the initial high capital expenditure of wave energy converters (wecs)," *Renewable and Sustainable Energy Reviews*, vol. 70, pp. 775–785, 2017.

[54] E. Moschos, G. Manou, P. Dimitriadis, V. Afentoulis, D. Koutsoyiannis, and V. K. Tsoukala, "Harnessing wind and wave resources for a hybrid renewable energy system in remote islands: a combined stochastic and deterministic approach," *Energy Procedia*, vol. 125, pp. 415–424, 2017.

[55] Z. Zhou, M. Benbouzid, J. F. Charpentier, F. Scuiller, and T. Tang, "A review of energy storage technologies for marine current energy systems," *Renewable and Sustainable Energy Reviews*, vol. 18, pp. 390–400, 2013.

[56] L. Wang, D.-J. Lee, W.-J. Lee, and Z. Chen, "Analysis of a novel autonomous marine hybrid power generation/energy storage system with a high-voltage direct current link," *Journal of Power Sources*, vol. 185, no. 2, pp. 1284–1292, 2008.

[57] Y. Zhang, M. Beer, and S. T. Quek, "Long-term performance assessment and design of offshore structures," *Computers & Structures*, vol. 154, pp. 101–115, 2015.

[58] M. Scotto and C. G. Soares, "Bayesian inference for long-term prediction of significant wave height," *Coastal Engineering*, vol. 54, no. 5, pp. 393–400, 2007.

[59] F. Schneider, Y. G. Garcia, and J. Denzler, "Modelling ocean parameters through graphical models," in *OCEANS 2017-Aberdeen*, pp. 1–6, IEEE, 2017.

[60] S. Illesinghe, R. Manasseh, R. Dargaville, and A. Ooi, "Idealized design parameters of wave energy converters in a range of ocean wave climates," *International journal of marine energy*, vol. 19, pp. 55–69, 2017.

[61] "Drum hv thermal management application note," *Elmo Motion Control Ltd.*, February 2016 Ver. 1.402.

[62] L. Li, Z. Yuan, and Y. Gao, "Maximization of energy absorption for a wave energy converter using the deep machine learning," *Energy*, vol. 165, pp. 340–349, 2018.

[63] M. A. Desouky and O. Abdelkhalik, "Wave prediction using wave rider position measurements and narx network in wave energy conversion," *Applied Ocean Research*, vol. 82, pp. 10–21, 2019.

[64] D. Sarkar, E. Contal, N. Vayatis, and F. Dias, "Prediction and optimization of wave energy converter arrays using a machine learning approach," *Renewable Energy*, vol. 97, pp. 504–517, 2016.

[65] S. M. Mousavi, M. Ghasemi, M. Dehghan Manshadi, and A. Mosavi, "Deep learning for wave energy converter modeling using long short-term memory," *Mathematics*, vol. 9, no. 8, p. 871, 2021.

[66] C. Ni, X. Ma, and J. Wang, "Integrated deep learning model for predicting electrical power generation from wave energy converter," in *2019 25th International Conference on Automation and Computing (ICAC)*, pp. 1–6, IEEE, 2019.

[67] Y. Ma *et al.*, *Machine learning in ocean applications: wave prediction for advanced controls of renewable energy and modeling nonlinear viscous hydrodynamics*. PhD thesis, Massachusetts Institute of Technology, 2020.

[68] S. C. James, Y. Zhang, and F. O'Donncha, "A machine learning framework to forecast wave conditions," *Coastal Engineering*, vol. 137, pp. 1–10, 2018.

[69] C. E. Stringari, P. V. Guimarães, J.-F. Filipot, F. Leckler, and R. Duarte, "Deep neural networks for active wave breaking classification," *Scientific Reports*, vol. 11, no. 1, pp. 1–12, 2021.

[70] S. Shamshirband, A. Mosavi, T. Rabczuk, N. Nabipour, and K.-w. Chau, "Prediction of significant wave height; comparison between nested grid numerical model, and machine learning models of artificial neural networks, extreme learning and support vector machines," *Engineering Applications of Computational Fluid Mechanics*, vol. 14, no. 1, pp. 805–817, 2020.

[71] E. Anderlini, D. I. Forehand, P. Stansell, Q. Xiao, and M. Abusara, "Control of a point absorber using reinforcement learning," *IEEE Transactions on Sustainable Energy*, vol. 7, no. 4, pp. 1681–1690, 2016.

[72] E. Anderlini, S. Husain, G. G. Parker, M. Abusara, and G. Thomas, "Towards real-time reinforcement learning control of a wave energy converter," *Journal of Marine Science and Engineering*, vol. 8, no. 11, p. 845, 2020.

[73] L. Bruzzone, P. Fanghella, and G. Berselli, "Reinforcement learning control of an onshore oscillating arm wave energy converter," *Ocean Engineering*, vol. 206, p. 107346, 2020.

[74] E. Anderlini, D. Forehand, E. Bannon, Q. Xiao, and M. Abusara, "Reactive control of a two-body point absorber using reinforcement learning," *Ocean Engineering*, vol. 148, pp. 650–658, 2018.

[75] S. Zou, O. Abdelkhalik, R. Robinett, U. Korde, G. Bacelli, D. Wilson, and R. Coe, "Model predictive control of parametric excited pitch-surge modes in wave energy converters," *International journal of marine energy*, vol. 19, pp. 32–46, 2017.

[76] A. M. Cornett, "A global wave energy resource assessment," in *The Eighteenth international offshore and polar engineering conference*, OnePetro, 2008.

[77] S. Ahn, "Modeling mean relation between peak period and energy period of ocean surface wave systems," *Ocean Engineering*, vol. 228, p. 108937, 2021.

[78] G. Li and M. R. Belmont, "Model predictive control of sea wave energy converters–part i: A convex approach for the case of a single device," *Renewable Energy*, vol. 69, pp. 453–463, 2014.

[79] J. H. Prudell, A. Schacher, and K. Rhinefrank, "Direct drive ocean wave energy electric plant design methodology," in *2012 Oceans*, pp. 1–7, IEEE, 2012.

[80] I. Temiz, J. Leijon, B. Ekergård, and C. Boström, "Economic aspects of latching control for a wave energy converter with a direct drive linear generator power take-off," *Renewable energy*, vol. 128, pp. 57–67, 2018.

[81] J. Prendergast, M. Li, and W. Sheng, "A study on the effects of wave spectra on wave energy conversions," *IEEE Journal of Oceanic Engineering*, vol. 45, no. 1, pp. 271–283, 2018.

[82] J. Falnes and A. Kurniawan, *Ocean waves and oscillating systems: linear interactions including wave-energy extraction*, vol. 8. Cambridge university press, 2020.

[83] P. D. Sclavounos and Y. Ma, "Wave energy conversion using machine learning forecasts and model predictive control," in *33th international workshop on water waves and floating bodies, France*, 2018.

Appendix A

Letters of Permission

In this chapter, the permission letters from the journals for approving the reuse of the materials in the papers are listed.

The permission letter is shown in Figure A.1 for using the paper from MDPI, Journal of Marine Science and Engineering.

The permission letter is shown in Figure A.2 for using the paper from ASME, International Conference on Offshore Mechanics and Arctic Engineering, and Power Conference.

Copyrights

Copyright and Licensing

For all articles published in MDPI journals, copyright is retained by the authors. Articles are licensed under an open access Creative Commons CC BY 4.0 license, meaning that anyone may download and read the paper for free. In addition, the article may be reused and quoted provided that the original published version is cited. These conditions allow for maximum use and exposure of the work, while ensuring that the authors receive proper credit.

In exceptional circumstances articles may be licensed differently. If you have specific condition (such as one linked to funding) that does not allow this license, please mention this to the editorial office of the journal at submission. Exceptions will be granted at the discretion of the publisher.

Figure A.1: The permission of reusing the paper [1]

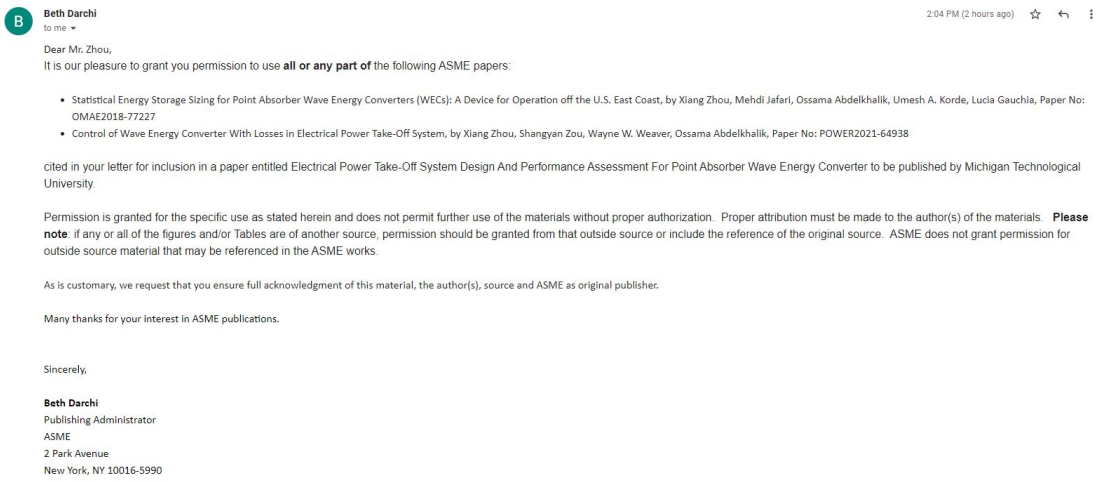

Beth Darchi
to me

2:04 PM (2 hours ago)

Dear Mr. Zhou,
It is our pleasure to grant you permission to use **all or any part of** the following ASME papers:

- Statistical Energy Storage Sizing for Point Absorber Wave Energy Converters (WECs): A Device for Operation off the U.S. East Coast, by Xiang Zhou, Mehdi Jafari, Ossama Abdelkhalik, Umesh A. Korde, Lucia Gauchia, Paper No: OMAE2018-77227
- Control of Wave Energy Converter With Losses in Electrical Power Take-Off System, by Xiang Zhou, Shangyan Zou, Wayne W. Weaver, Ossama Abdelkhalik, Paper No: POWER2021-64938

cited in your letter for inclusion in a paper entitled Electrical Power Take-Off System Design And Performance Assessment For Point Absorber Wave Energy Converter to be published by Michigan Technological University.

Permission is granted for the specific use as stated herein and does not permit further use of the materials without proper authorization. Proper attribution must be made to the author(s) of the materials. **Please note**: if any or all of the figures and/or Tables are of another source, permission should be granted from that outside source or include the reference of the original source. ASME does not grant permission for outside source material that may be referenced in the ASME works.

As is customary, we request that you ensure full acknowledgment of this material, the author(s), source and ASME as original publisher.

Many thanks for your interest in ASME publications.

Sincerely,

Beth Darchi
Publishing Administrator
ASME
2 Park Avenue
New York, NY 10016-5990

Figure A.2: The permission of reusing the paper [2, 3]